HOT CHEMISTRY AND PHYSICS IN THE PLANET-FORMING ZONES OF DISKS

Hot Chemistry And Physics In The Planet-Forming Zones Of Disks

Thesis Universiteit Leiden - Illustrated - With summary in Dutch and English - With references
ISBN: 978-94-6182-206-2
Printed by Offpage.nl
Cover: Photo and design by Eva Polakovičová (eeeeefa@gmail.com)

HOT CHEMISTRY AND PHYSICS IN THE PLANET-FORMING ZONES OF DISKS

PROEFSCHRIFT

ter verkrijging van de graad van Doctor aan de Universiteit Leiden,
op gezag van de Rector Magnificus prof.mr. P.F. van der Heijden,
volgens besluit van het College voor Promoties
te verdedigen op donderdag 10 januari 2013
klokke 15.00 uur door

Jeanette Bast

geboren te Stockholm, Zweden in 1979

Promotiecommissie

Promotores:	Prof. dr. E. F. van Dishoeck	
	Prof. dr. A. G. G. M. Tielens	
Overige Leden:	Prof. dr. K. Kuijken	
	Prof. dr. C. W. M. Fridlund	
	Prof. dr. G. A. Blake	California Institute of Technology
	Dr. M. R. Hogerheijde	
	Dr. A. M. Mandell	NASA Goddard Space Flight Center

To my parents,

for teaching me to stand up, learn and move on,
whenever failure comes into your life.

Contents

I

Introduction

Questions about our origin have always fascinated humankind. Where do we come from? How did life arise from the beginning? Is the origin of life something specific to our own planet? Indeed, can life exist elsewhere? Many of these questions will remain unanswered for many more generations to come and require progress in many small steps. In this thesis one of these smalls steps towards answering the question about the origin of life is taken by studying the regions around stars where terrestrial, hence Earth like, planets are thought to be forming. These are the planets that today we think would be the best candidates for having life supporting conditions.

1.1 The formation of planetary systems

The formation of a planetary system starts with the formation of substructures in molecular clouds that can contract under their own gravity. These parts of the molecular cloud get more and more dense until their cores reach such high densities that stars are born there (see reviews by Bergin & Tafalla 2007, di Francesco et al. 2007). Because of angular momentum, the collapsing core will rapidly form a circumstellar disk around the star. The most deeply embedded phase is called a class 0 object or protostar. The material from the collapsing envelope will start to accrete onto the star through the disk. The star in turn will heat up the surrounding disk and envelope. Some of the material will be ejected in the form of a stellar jet or disk wind along the rotational axis. This will disrupt and clear away the envelope. This phase of the still young protostar is called the class I stage, see Adams et al. (1987) and André et al. (1993) for further details on classification. Once most of the envelope has accreted onto the disk or been blown away by the wind, only the disk is left around the star. The disk is the location where planets are thought to be formed and is therefore called a protoplanetary disk. The object is a T Tauri star if the stellar mass is < 2 M_{Sun} and a Herbig AeBe star if the mass is within the range $2 - 8$ $M_{\odot}$. The formation and evolution of the pre-main sequence star and a protoplanetary disk is summarised in Fig. 1.1. That these protoplanetary disks indeed exist in reality and not just in theory has been confirmed by the detection of an infrared access in their spectral energy distribution (SED) that could only be explained by a disk around the star (Kenyon & Hartmann 1987, Calvet et al. 1992, Chiang & Goldreich 1997, Men'shchikov & Henning 1997, D'Alessio et al. 1998). Later on direct observations done by for example the Hubble Space Telescope of circumstellar disks or proplyds, as they also can be called when an external light source illuminates them on the sky, could further prove their existence (see Fig 1.2) (O'Dell et al. 1993). In addition these disks can be detected by observing scattered stellar light on the dust grains located in the disk (Grady et al. 2005, Fukagawa et al. 2004, Clampin et al. 2003, Heap et al. 2000, Augereau et al. 2001, Grady et al. 1999).

In the early stages of the protoplanetary disk the temperature in the inner disk is hot enough so that all primordial grains are sublimated. Once the gas cools down, various compounds can start to condense. Which species condense out, and hence the chemical composition of the inner disk, will vary with the temperature and the cooling time which are both very dependent on the radial and vertical location of the gas. At this point, planets can start to form. The type of planets, their atmospheres and their radial location and their mass distribution will then strongly depend on the chemical and physical structure of the disk (see reviews by Prinn 1993, Ehrenfreund & Charnley 2000, Markwick & Charnley 2004, Bergin 2009). How this planet formation process proceeds and what will be its products can be better understood by studying the physical and chemical evolution models of the gas and dust in these disks. Fig. 1.3 shows an overview of typical chemical

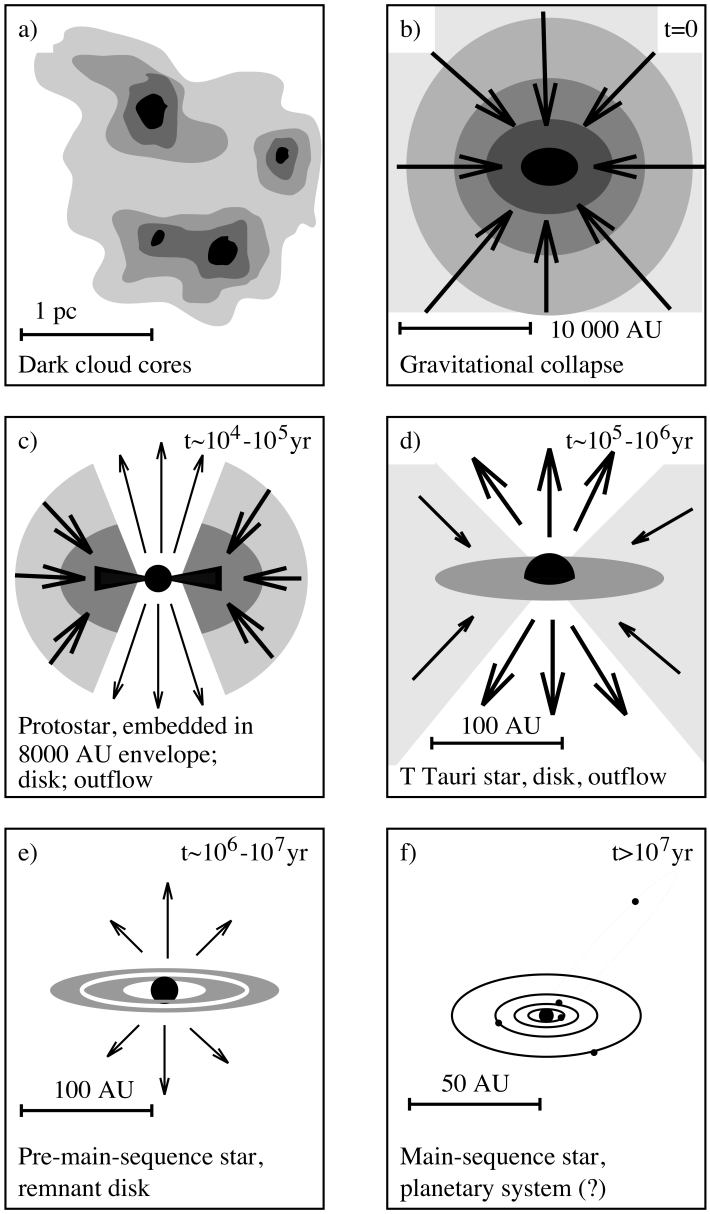

Figure 1.1 The formation and evolution of a protoplanetary disk. The different stages are shown, going from the dark cloud core, through the embedded proto star phase, with its circumstellar disk and outflow that carves out the envelope, until the protoplanetary disk becomes visible and a planetary system can form (Hogerheijde 1998).

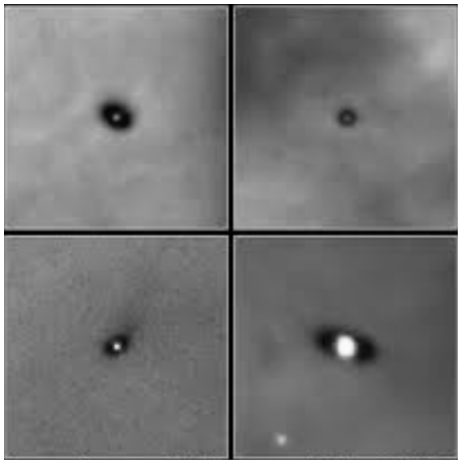

Figure 1.2 Direct observations of protoplanetary disks in the Orion nebula using the Hubble space telescope. Note how the disk is shown as a darker shadow surrounding the stars in front of the bright nebula. These protoplanetary disks have radii ranging from 100 – 300 AU (McCaughrean & O'Dell 1995, Bally et al. 2000).

conditions and physical processes in a protoplanetary disk.

The habitable zone of protoplanetary disks is especially interesting to study. This region is the zone in which a planet can have the proper conditions to be able to form or at least maintain life. One of the requirements is that the planet can have a temperature than permits liquid water on its surface. All life - as we know it - needs liquid water, so this is often considered a necessary condition for life. This habitable zone is in our own solar system estimated to be between 0.95 – 1.37 AU (Kasting et al. 1993). However, this radial range varies with different planetary and stellar properties. One factor is the luminosity of the star. For higher stellar luminosities, the habitable zone will move further away from the star and broaden. For example, the habitable zone is larger around F stars than around our Sun (a G star) and it is smaller around K and M stars.

Circumstellar chemical and physical evolution disk models start with initial conditions such as the temperature and density distribution and kinematics of the gas, chemical composition and gas/dust ratio of the disk. The chemical and physical structures that the models produce can then be compared with the observations of the gas and dust in protoplanetary disks (Natta et al. 2007, Bergin et al. 2007b). the next step is to compare with existing and future even more detailed observations of exoplanets and their atmosphere (e.g., Mayor & Queloz 1995, Borucki et al. 2011, Madhusudhan et al. 2011, Désert et al. 2011, Brogi et al. 2012).

1.2 A chemical and physical inventory of planet-forming zones

As discussed in Section 1.1 it is very important to understand the different physical and chemical properties of the protoplanetary disk to be able to understand how and which type of planets that form there. It is especially interesting to be able to define these properties in the inner regions of these disks since this is where the habitable zone is located. These parameters will not just help constraining the chemical evolution disk models but also the planet-formation models. These chemical disk models can then simulate and address the evolution of the organic inventory with characteristics such as temperature structure, different radiation fields and different molecular abundances.

It is for example interesting to study which types of more complex organic molecules can be constructed. It is observationally difficult to determine the inventory of large complex molecules as their abundance is expected to be low. Hence chemical models are required to predict abundances of complex molecules and these models have to be based upon observations of simple molecules. These more complex molecules are very interesting to study since they are considered to be the most important ones in being able to form planets with preferable conditions for life.

There are several different types of chemical evolution disk models. What mainly separate them are their different ways of breaking carbon out of CO and nitrogen out of N_2. The Najita et al. (2011) model for example include a X-ray field and the Agúndez et al. (2008), Woitke et al. (2009), Willacy & Woods (2009), Vasyunin et al. (2011), Walsh et al. (2012) models include an UV-field and photo-ionisation and photo-dissociation processes. The Walsh et al. (2012) model takes both the X-ray and UV-fields into account. There are also other important parameters such as cosmic ray ionisation, gas versus dust temperatures and the settling of the disk. Models also differ in the size of the chemical networks considered and the types of chemical reactions included. Molecular observations of protoplanetary disks can provide key tests of such models.

As circumstellar disks are small and not very luminous, good telescope and spectrometers with both very high spatial and spectral resolution are required in order to study chemistry and physical conditions in the inner regions of disks. The first observations of these sources were done at submillimeter and radio wavelengths since at these wavelengths high spectral and spatial resolution can be achieved by the use of single dish and interferometry. Molecules such as CO, H_2O, HCO^+, H_2CO, HCN, N_2H^+, CN, C_2H, SO, DCO^+ and DCN have been detected in this way (Dutrey et al. 1997, Kastner et al. 1997, Thi et al. 2004, Fuente et al. 2010, Henning et al. 2010, Öberg et al. 2011, Hogerheijde et al. 2011). However these observations cover the colder gas which is mainly located > 100 AU in the disk which is not where most planets are thought to be forming. Only in the last 15 years have telescopes become sensitive enough to study the chemistry in the

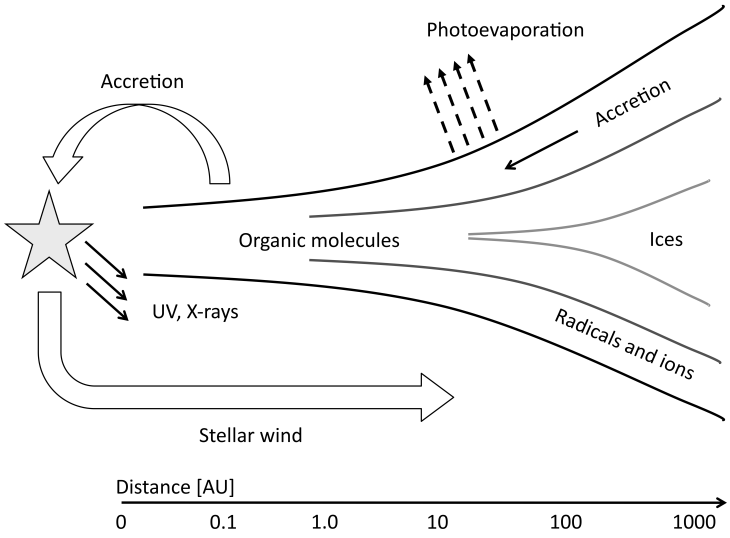

Figure 1.3 An overview of the different physical processes in a protoplanetary disk and its chemical structure; Material is accreted from the envelope and transported through the disk to the inner regions where accretion onto the star can occur. The gas gets photo-evaporated further out in the disk since the thermal speed of the gas can more easily exceed the escape velocity in these regions than in the inner disk (Störzer & Hollenbach 1999). Young stellar objects often have stellar winds which may impact the disk. Stellar UV and X-ray photons produce a photodissociation region on the surface of the disk. In the midplane there is ongoing ice accretion. Photo-desorption causes sublimation from ices in the surface layers of the disk. Warm chemistry in the inner regions (< a few AU) or in the surface layers produces more complex molecules at a few hundred up to a few thousand Kelvin.

inner regions (< 10 AU) of the circumstellar disks.

CO was the first molecule observed to originate from the hot inner disk (e.g., Najita et al. 2003, Brittain et al. 2003, 2007, 2009, Blake & Boogert 2004, Pontoppidan et al. 2008, Salyk et al. 2009, 2011b, Brown et al. subm.) and this was quickly followed by observations of H_2O, OH, CO_2, C_2H_2 and HCN (Carr et al. 2004, Lahuis et al. 2006, Gibb et al. 2007, Carr & Najita 2008, Salyk et al. 2008, Pascucci et al. 2009, Najita et al. 2010, Pontoppidan et al. 2010, Carr & Najita 2011, Kruger et al. 2011, Salyk et al. 2011). A very important milestone was the first detection of water (Carr & Najita 2008, Salyk et al. 2008) in these regions. This is because the presence of water is generally considered to be a necessary condition for life. Today we know that water and also other pre-biotic molecules such as HCN seem to be abundant in these regions and hence the warm gas in the planet forming zones of these disks seems to nourish a rich organic inventory. There are therefore many reasons to continue to gather even more information about these regions to be able to improve our knowledge about the physical and chemical conditions of these planet-forming zones.

1.2.1 Probing planet-forming regions with infrared observations

Near infrared and mid infrared observations around 1 – 30 μm are the best way to study the gas in the inner planet-forming zones of circumstellar disks. This is because the gas in these regions is warm, ranging from a few hundred to several thousand Kelvin, and therefore emits copiously in this wavelength region. In the near-infrared, around 1 – 5 μm, observations can be done from the ground and this allows the use of large spectrometers with high spectral and spatial resolution. Such instruments cannot be included in space-based observatories because of space and weight limitations. The best spectrometers today that can be used for observations within this wavelength range are NIRSPEC with a spectral resolving power of $R = \delta\lambda/\lambda = 25{,}000$ at the Keck telescope and the CRIRES spectrometer ($R = 10^5$) at the Very Large Telescope (VLT). This high spectral resolution means that the spectral lines can be individually resolved and even details of the line profiles can be detected. Most of the mid infrared lines from 5 – 30 μm cannot be observed on Earth because the atmosphere that is opaque at these wavelengths. The spectrometer IRS at the *Spitzer* Space Telescope is the instrument that has been primarily used within this wavelength range. Observations from all of these three telescopes are presented in this thesis. In particular, this thesis makes use of data from a large VLT-CRIRES program surveying ~70 disks around T Tauri and Herbig Ae stars (Pontoppidan et al. 2011b, Brown et al. subm.) For an overview of the various kinds of observations used for studying the emission from the relevant regions see Fig. 1.4.

The main focus of this thesis is to study emission and absorption lines from the

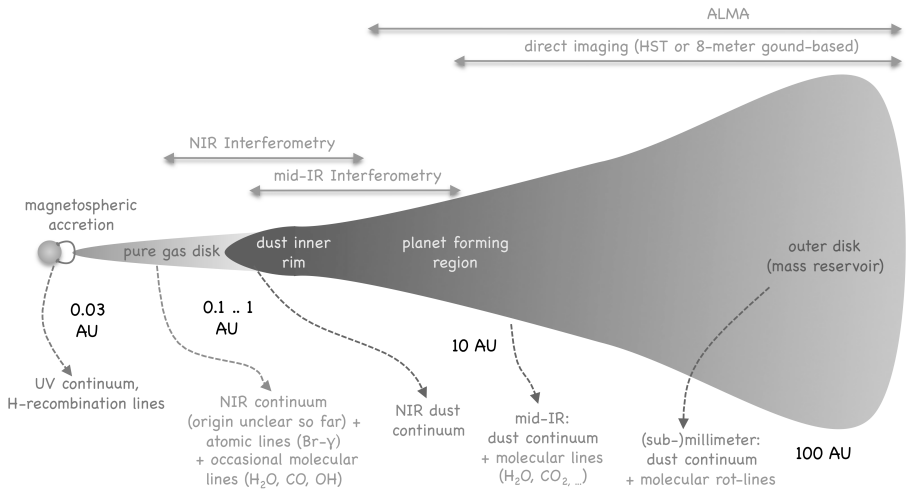

Figure 1.4 An overview of which areas of a protoplanetary disk different types of observations cover. In addition the type of continuum plus molecular emission that can be expected from different parts of the disk are presented here (Dullemond & Monnier 2010).

molecules H_2O, OH, CO_2, C_2H_2 and HCN. These molecules are all important prebiotic molecules and are also building blocks of more complex species. In addition, these molecules are sensitive tracers for the temperature and the different radiation fields in the disk. Their sensitivity as tracers means that by studying for example their relative and absolute amounts one can decide which the main reaction routes within a chemical network must have been to form them. These reaction routes are often controlled by an activation barrier that requires high temperatures to proceed. Reaction routes can also be affected by the local radiation field as that sets the level of ionisation and ions may react much more quickly than neutral species. These observations can also address evolutionary questions related to the origin of the relevant species. Specifically, are these molecules formed in the very early class 0 stage on the colder dust grains or later during the class II stage in the hot chemistry in the upper layers of the disk. It will also contribute to the more general astrochemical understanding of which type of chemical processes that play an important role in the formation/destruction reactions for different molecules in these environments.

In this thesis the focus is on ro-vibrational transitions of molecules. Unlike pure rotational transitions, which are predominantly emitted by cold gas far out in the disk, mid-IR ro-vibrational lines originate in the warm gas in the inner disks. These type of molecules can go through both vibrational and rotational transitions which do impact each other. This interaction is however so small that it can be omitted at a first order approximation when estimating the total ro-vibrational energy for one transition level. The total energy $E_{vib,rot}$ of a ro-vibrational transition can therefore be calculated using equation:

$$E_{vib,rot} = E_{vib} + E_{rot} = \left(v + \frac{1}{2}\right) h\nu_0 + hc\bar{B}J(J+1) \tag{1.1}$$

where v is the vibrational quantum number, J is the rotational quantum number, h is Planck's constant, ν_0 is the frequency of the vibration, c is the speed of light, and $\bar{B}$ is the rotational constant. Due to quantum mechanical selection rules, only transitions where ΔJ is 0, ±1 are allowed. The transitions will split out into R, Q and P-branches characterised by $\Delta J = 1$, 0 and -1 (see Fig 1.5). Note that some molecules (e.g.., CO) do not have a Q-branch e.g., $\Delta J = 0$ is not allowed. As an example the spectrum of the ν_3 mode of the C-H stretch at 3.019 μm of HCN has been plotted in the middle panel of Fig. 1.6 where the R, P and Q branches can be clearly seen. The overall extent of the P and R branches will depend on the level populations, in v=1 for emission and v=0 for absorption. These level populations are set by collisions - and hence are sensitive to the density and temperature of the emitting gas - as well as by the radiation field that can excite levels as well. Thus, the envelope of the P and the R branches will be broader for warmer gas, for denser gas and for gas that is pumped by a radiation field (see Fig. 1.6). The individual lines in the Q branch will generally blend into one broad feature. The profile of this feature will however still be set by the level populations and this can be used to derive the physical conditions in the emitting or absorbing gas.

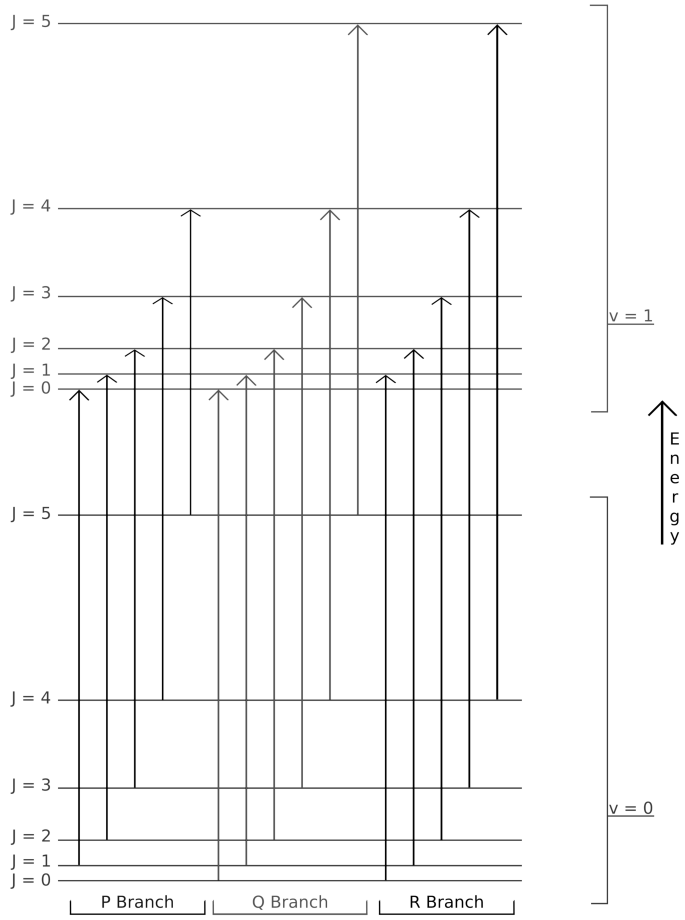

Figure 1.5 A schematic diagram of ro-vibrational transitions to illustrate how the R, Q and P branches arise.

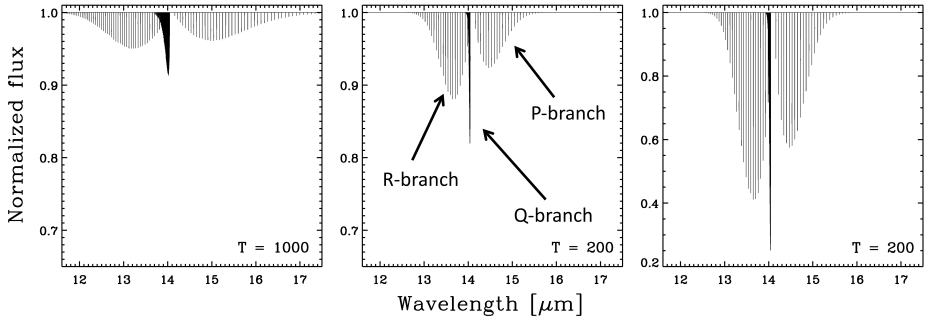

Figure 1.6 Absorption spectra of the ν_3 mode of HCN at the temperatures 200 and 1000 K and column densities $3.0 \cdot 10^{16}$ (left and middle panel) and $7.0 \cdot 10^{16}$ cm^{-2} (right panel).

1.3 This thesis

We now know that by studying the physical and chemical conditions in protoplanetary disks we can better understand how planetary systems are formed. These studies provide input for studies of planet-formation. They are what we can call the recipe for planets. However we also know that in order to use these models we need the parameters, hence the ingredients, for these recipes. The goal of this thesis is to provides these physical and chemical ingredients by using observations. The main questions together with short explanations for how we can use observations to answer these question are summarized here:

- **Which molecules can be found in these regions?** - Trying to detect different molecules by using observations.
- **What is the temperature of the gas where we detect the molecules?** - The comparison between the relative strengths of lines of a molecule provides a probe of the temperature of the gas where these molecules are excited.
- **Which type of excitation processes dominate?** By relating the observed excitation of these molecules to the local physical conditions (density, temperature, and radiation field), the dominant excitation process - collisions versus radiation - can be studied.
- **What is the spatial location of these molecules?** - The use of radiative transfer disk models can analyze line profiles of spectrally resolved lines to determine their spatial location. Different spatial distributions of a certain molecule will have different types of line profiles.

- **What are the chemical processes that form these molecules?** - By modeling the different intensities of the different molecular line profiles relative abundances can be estimated. These abundances can in turn be compared to the expected relative abundances that different chemical disk models predict depending on their different dominating chemical processes.

The four following chapters summarise the work that has been done addressing these questions. The main content of each chapter is described here:

Chapter 2: The origin of unexpected CO line profiles

During the investigation of CO emission line profiles, 8 out of ~50 T Tauri stars showed a broad based single peaked line profile. This type of line profile does not agree well with the expected line profile from Keplerian rotating gas in the inner region of a protoplanetary disk. An investigation was therefore done using the high spectral resolution CO 4.7 μm lines to see if the origin of these types of line profiles could be explained. The investigation showed that all of the 8 sources have in common that they have high mass accretion rates and have higher line to continuum ratios than their parent sample. In addition their CO lines are excited to higher vibrational states up to $v = 2$, and 4 out of 8 sources up to $v = 4$, and their rotational excitation temperature (~300 – 800 K) is lower than their vibrational temperature (~ 1700 K). This tells us that their CO lines are UV - pumped and hence exposed to a strong UV-field. The observations also show that the emission comes from within a few AU and has a velocity shift of < 5 km s^{-1} relative to the radial velocity of their parent star. One of the main results from this investigation is that these line profiles could not solely originate from a Keplerian rotating disk as was earlier expected. In addition an origin in a funnel flow and in magnetically, FUV or X - driven winds could also be ruled out. The results show that a combination of a disk plus a slow EUV launched disk wind is the most probable explanation of the birth place for these broad based single peaked line profiles.

Chapter 3: First detections of near infrared emission from organics

Only three molecules H_2O, OH and CO have previously been detected in near-infrared emission from the innermost regions of protoplanetary disks. The difficulty in detecting more molecules has to do with the large amount of the same molecules in the atmosphere of the Earth. The atmospheric molecules create very broad saturated absorption lines in the spectra that totally dominate the much weaker emission lines from the circumstellar disks. By observing the disks while they are having an as high as possible relative radial velocity shift to the Earth, combined with a very precise modeling of the atmospheric absorption lines, we are able to present the first detections of HCN near-infrared emission lines in 3/3 observed sources and C_2H_2 emission lines in one source as well as very stringent

upper limits on both NH_3 and CH_4. Relative abundances of these molecules as well as of H_2O and OH are presented and their excitation temperatures are extracted by using both a radiative transfer slab model and a more precise disk model to compare the results with each other. Both models give comparable results. These 3 protoplanetary disks, which all belong to the same sample of the 8 disks discussed in Chapter 2 with single peaked broad based CO line profiles, also show the same type of line profiles for these organic molecules. Hence the origin of these organics may as well be linked to a disk + disk wind.

Chapter 4: Investigation of HCN excitation in protoplanetary disks

Earlier radiative transfer slab and disk models used local thermodynamic equilibrium (LTE) as an approximation in their models when trying to fit observed near- and mid-infrared line fluxes from the planet-forming zones of the disks. This approximation is done since implementing non-LTE in those models is a cumbersome and time consuming task. The main problem is however that the line emission from these regions is thought to come from gas that does not achieve high enough densities to be well described by LTE. A study is therefore presented in this chapter to investigate how the 3 and 14 μm emission from these regions will change using non-LTE in a slab model relative to LTE conditions and also to include radiative pumping in the excitation process of the HCN molecule. We conclude that the 3 μm line fluxes will be overestimated and hence the column density of HCN underestimated when using a LTE model. In addition it is shown that a slab model including both non-LTE and in addition radiative pumping will much better describe the excitation at 3 μm and hence derive better estimates of the HCN abundance. The 14 μm line emission is however not as much affected by non-LTE excitation since it reaches LTE at much lower densities than the 3 μm emission due to its lower critical density.

Chapter 5: Exploring organic chemistry in planet-forming zones

An investigation using high S/N *Spitzer* data was performed here for the first time to look for the most abundant more complex organic molecules in the inner regions of disks predicted by chemical models. This was done by studying two edge-on disks which show absorption lines instead of emission lines. Absorption lines have the main advantage that they have a much stronger line to continuum ratio compared to emission lines and hence much less abundant molecules can be studied. We have detected absorption lines of CO_2, HCN and C_2H_2. Analysis of the observations reveals similar abundances as observed for deeply embedded protostars as well as for comets in our own Solar system. This intriguing result suggests that (part of the) cometary material originates from the inner warm regions of the Solar Nebula. We also establish 3σ upper limits for the abundance ratios of C_2H_4, C_2H_6, C_6H_6, C_3H_4, C_4H_2, CH_3, HNC, HC_3N, CH_3CN, NH_3 and SO_2 relative to C_2H_2 and HCN. A comparison shows that the upper molecular limits

relative to C_2H_2 and HCN agree much better with high temperature chemistry disk models including both UV and X-ray irradiation rather than just a X-ray irradiation. Also, the NH_3/HCN abundance tells us that the NH_3 molecules must have been formed in the warm chemistry of the disk atmospheres instead of being evaporated from the icy mantles of dust grains coming from the earlier stages of the disk evolution. In addition, simulations for future instruments like JWST, SOFIA, SPICA and ELTs show that molecules with at least one order of magnitude lower abundances relative to *Spitzer* observations can be detected with these future instruments. This would mean that much more strict constraints can be put on future chemical disk models.

1.4 Main conclusions

The main aim of this thesis is to contribute to the understanding of the physical and chemical conditions in regions of planet formation. This has been done by extracting physical and chemical parameters of the gas in the inner regions of protoplanetary disks by using infrared observations to better constrain planet formation and chemical disk evolution models. The extracted parameters and their resulting conclusions that could be drawn from this work are as follows:

- **Detections and molecular abundances:** HCN and C_2H_2 have been detected in the innermost disk (< 1 AU) and their relative column densities extracted using the high spectral resolution CRIRES data in combination with our newly developed observational tools. In addition strict upper limits on NH_3 and CH_4 were found using CRIRES and for the first time upper limits on the organics and sulfur bearing molecules C_2H_4, C_2H_6, C_6H_6, C_3H_4, C_4H_2, CH_3, HNC, HC_3N, CH_3CN, NH_3 and SO_2 have been made using the *Spitzer* telescope.
- **Temperatures:** Excitation temperatures and temperature structures have been estimated for CO, H_2O, OH, C_2H_2, HCN and CO_2 using both slab and disk radiative transfer models, modeling both emission and absorption line profiles.
- **Origin of emission:** Evidence has been found for a non-Keplerian origin from detected CO, H_2O and HCN emission lines. The origin of the emission is concluded to come from a disk + disk wind. We have shown that modeling of line profiles is important to be able to constrain the spatial distribution of the gas.
- **Excitation and chemistry:** We have shown that emission from the inner region of a protoplanetary disk is not well described using a LTE slab model. It is therefore very important to include non-LTE, radiative pumping and both UV irradiation and X-rays in future radiative transfer and chemical evolution disk models.

1.5 Future prospects and outlook

This thesis shows that, today, we can start to get detailed information about the chemical and physical structure of the planet-forming zones which was earlier only possible in the outer regions by using millimeter observations.

Instruments like CRIRES could for the first time provide us with details of the line profiles in these regions and reveal the importance of being able to describe these line profiles. This is and will be a very exciting challenge for future modelers. It is not enough any longer to just model the intensities and excitation temperatures of the lines and assume simple approximations such as a spatial distribution consisting of gas in Keplerian rotation around a star. Future radiative transfer models need to include a combination of origins of the gas, such as different types of disk winds, funnel flows and the disk itself. In addition different types of radiation fields, non-LTE excitation and the gas/dust ratio are very important to include to get more detailed information about the excitation processes of these molecules. Chemical disk evolution models also need to include different types of radiation fields and expand their chemical networks with even more molecules and their different types of formation and destruction routes both on dust grains and in the warm gas.

New and even more detailed observations is the only way to provide the modelers with the necessary information they need to be able to improve their models. Telescopes such as JWST, SOFIA, SPICA and ELTs will be able to both push the detection limits for the less abundant and more complex organic molecules and in addition give even more detailed line profile or spatial information. It is especially interesting to compare these results with the upcoming observations done by ALMA of the outer cooler regions in the disk. These comparisons will provide us with a much more complete picture of protoplanetary disks and their evolution. This information will in the end help us to understand how such a wide variety of planets can form and, at least in one case, provide such favourable conditions that even life itself could evolve there.

II

Single peaked CO emission line profiles from the inner regions of protoplanetary disks[1]

Context Protoplanetary disks generally exhibit strong line emission from the CO fundamental v=1–0 ro-vibrational band around 4.7 μm. The lines are usually interpreted as being formed in the Keplerian disk, as opposed to other kinematic components of the young stellar system.
Aim This paper investigates a set of disks that show CO emission line profiles characterized by a single, narrow peak and a broad base extending to $> 50\,\mathrm{km\,s^{-1}}$, not readily explained by just Keplerian motions of gas in the inner disk.
Methods High resolution ($R = 10^5$) *M*-band spectroscopy has been obtained using CRIRES at the Very Large Telescope in order to fully resolve fundamental ro-vibrational CO emission line profiles around 4.7 μm.
Results Line profiles with a narrow peak and broad wings are found for 8 disks among a sample of ~50 disks around T Tauri stars with CO emission. The lines are very symmetric, have high line/continuum ratios and have central velocity shifts of < 5 km s^{-1} relative to the stellar radial velocity. The disks in this subsample are accreting onto their central stars at high rates relative to the parent sample. All 8 disks show CO emission lines from the $v = 2$ vibrational state and 4/8 disks show emission up to $v = 4$. Excitation analyses of the integrated line fluxes reveal a significant difference between typical rotational (~300-800 K) and vibrational (~1700 K) temperatures, suggesting that the lines are excited, at least in part, by UV-fluorescence. For at least one source, the narrow and broad components show different excitation temperatures, but generally the two component fits have

[1] Based on: J.E. Bast, J.M. Brown, G.J. Herczeg, E.F. van Dishoeck and K.M. Pontoppidan, 2011, A&A, 527, A119

similar central velocities and temperature. Analysis of their spatial distribution shows that the lines are formed within a few AU of the central star.
Conclusions It is concluded that these broad centrally peaked line profiles are inconsistent with the double peaked profiles expected from just an inclined disk in Keplerian rotation. Models in which the low velocity emission arises from large disk radii are excluded based on the small spatial distribution. Alternative non-Keplerian line formation mechanisms are discussed, including thermally and magnetically launched winds and funnel flows. The most likely interpretation is that the broad-based centrally peaked line profiles originate from a combination of emission from the inner part (< a few AU) of a circumstellar disk, perhaps with enhanced turbulence, and a slow moving disk wind, launched by either EUV emission or soft X-rays.

2.1 Introduction

It is generally thought that planets form in the inner regions of protoplanetary disks ($\lesssim$10 AU Lissauer 1993). Information on the physical structure, gas dynamics and chemical composition of the planet-forming region is essential to constrain models of planet formation. Processes like planet migration, which can change the orbits of newly formed planets, depend sensitively on the presence of gas in the disk (e.g., Ward 1997, Kley et al. 2009). The planetary mass distributions (Ida & Lin 2004) and planetary orbits (Kominami & Ida 2002, Trilling et al. 2002) resulting from planet formation models can eventually be tested against recent observations of exo-planetary systems (e.g., Mordasini et al. 2009a,b). Observations of line emission from disks at high spectral and spatial resolution are needed to provide the initial conditions for these models. Gas-phase tracers of the disk surface can also be used to probe photo-evaporation processes (Gorti et al. 2009, Gorti & Hollenbach 2009). More generally, these observations provide constraints on the lifetime of the gas in the inner part of the disk and thus its ability to form giant gaseous planets.

The bulk of the gas mass in protoplanetary disks is in H_2 but this molecule is difficult to observe since its rotational quadrupole transitions from low-energy levels are intrinsically weak and lie in wavelength ranges with no or poor atmospheric transmission (e.g., Carmona et al. 2007). In contrast, the next most abundant molecule, CO, has ro-vibrational lines which can be readily detected from the ground. This makes CO an optimal tracer of the characteristics of the warm gas in the inner regions of disks (see Najita et al. 2007,for overview). CO overtone emission ($\Delta v = 2$) was detected for the first time in low and high mass young stellar objects by Thompson (1985) and was attributed to circumstellar disks by Carr (1989).

Overtone emission lines at 2.3 μm from disks around T Tauri stars, when present, have been fitted with double peaked line profiles with a FWHM of around 100 km s^{-1}, which suggests an origin in the innermost part (0.05-0.3 AU) of the disk under the assumption of Keplerian rotation (Carr et al. 1993, Chandler et al. 1993, Najita et al. 1996). The relative intensities of the ro-vibrational lines can be used to determine characteristic CO excitation temperatures (rotational and vibrational), which, in turn, provide constraints on the kinetic temperatures and densities in the line-forming region. The overtone data resulted in temperature estimates in the 1500-4000 K range and with densities of $>10^{10}$ cm^{-3} (Chandler et al. 1993, Najita et al. 2000, 2007).

Fundamental CO $v = 1 - 0$ emission at 4.7 μm has been observed both from disks around T Tauri stars (e.g., Najita et al. 2003, Rettig et al. 2004, Salyk et al. 2007, Pontoppidan et al. 2008, Salyk et al. 2009) and around Herbig Ae/Be stars (e.g., Brittain et al. 2003, Blake & Boogert 2004, Brittain et al. 2007, 2009, van der Plas et al. 2009). The fundamental ro-vibrational lines are excited at lower temperatures (1000-1500 K) than the overtone lines (Najita et al. 2007). Fundamental

CO emission lines are usually fitted with double peaked or narrow single-peaked line profiles that can be described by a Keplerian model. Single-peaked line profiles with broad wings (up to 100 km s^{-1}) in T Tauri disks have been seen by Najita et al. (2003), who also discussed their origin. Three possible formation scenarios were mentioned: disk winds, funnel flows or gas in the rotating disk. The latter option was favored, and the lack of a double peak was ascribed to the relatively low (R=$\lambda/\Delta\lambda$=25000) spectral resolving power of the data. Alternative explanations such as an origin in disk winds and funnel flows were ruled out mainly because of the lack of asymmetry in the line profiles.

The high resolution ($R = 10^5$) spectrometer CRIRES (CRyogenic InfraRed Echelle Spectrograph) fed by the MACAO (Multi - Application Curvature Adaptive Optics) adaptive optics system on the Very Large Telescope offers the opportunity to observe molecular gas emission from T-Tauri disks with unsurpassed spectral and spatial resolution. A sample of ∼70 disks was observed in the fundamental CO band around 4.7μm as part of an extensive survey of molecular emission from young stellar objects. In total, 12 of the 70 T Tauri stars show CO emission lines with a broad base and a narrow central peak, from now on called broad-based single peaked line profiles. Eight of the 12 T Tauri stars are selected for detailed analysis in this paper, based on criteria discussed in §2.3.5. Because the lines remain single peaked even when observed at 4 times higher spectral resolution than previous observations, the lack of a double peak can no longer be explained by the limited resolution in Najita et al. (2003). Hence the modeled double peaked lines in Najita et al. (2003) are not a plausible explanation for the centrally peaked line profiles in T Tauri disks. The aim of this paper is to classify these broad centrally peaked lines and to constrain their origin. Since many of these sources have high line to continuum ratios and are prime targets to search for molecules other than CO (e.g. Salyk et al. 2008), a better understanding of these sources is also warranted from the perspective of disk chemistry studies.

The observations and sample are presented in §3.2. In section §2.3 the line profiles are modeled using a Keplerian disk model where it is concluded that a model with a standard power-law temperature structure does not provide a good fit to the broad-based single peaked line profiles. The profiles are subsequently inverted to determine what temperature distribution would be consistent with the spectra. The origin of the emission is then further constrained in §2.4 by extracting radial velocity shifts between the gas and the star, determining rotational and vibrational temperatures and investigating the extent of the emission. In §5.4 the results are discussed and they are summarized in §5.5.

Table 2.1 List of sources with single-peaked line profiles analyzed in this paper.

Source[a]	α(J2000)	δ(J2000)	Spectral Type	Distance (pc)	Flux [Jy]	$T_{\rm eff}$ [K]	$L_\star$ [$L_\odot$]	Ref.[b]
AS 205 A (N)[c]	16 11 31.4	-18 38 24.5	K5	125	4.0	4250	4.0	1, 4, 8, 10
DR Tau	04 47 06.2	+16 58 42.9	K7	140	1.3	4060	1.1	4, 5, 11
RU Lup	15 56 42.3	-37 49 15.5	K7	140	1.1	4000	1.3	1, 6, 12, 15
S CrA A (N)	19 01 08.6	-36 57 20.0	K3	130	2.2	4800	2.3,	2, 3, 17
S CrA B (S)	19 01 08.6	-36 57 20.0	M0	130	0.8	3800	0.8	2, 3, 17
VV CrA A (S)	19 03 06.7	-37 12 49.7	K7	130	-	4000	0.3	3, 13, 16
VW Cha	11 08 01.8	-77 42 28.8	K5	178	0.7	4350	2.9	7, 9, 14
VZ Cha	11 09 23.8	-76 23 20.8	K6	178	0.4	4200	0.5	7, 9, 14

[a]Three of these sources are binaries and the separations between their A and B components are: AS 205: 1.″3, S CrA: 1.″3 and VV CrA: 1.″9 (Reipurth & Zinnecker 1993).

[b]References. - (1) Kessler-Silacci et al. (2006); (2) Prato et al. (2003); (3) Takami et al. (2003); (4) Salyk et al. (2008); (5) Muzerolle et al. (2003); (6) Günther & Schmitt (2008), (7) Luhman et al. (2008), (8) Evans et al. (2009), (9) Whittet et al. (1997); (10) Andrews et al. (2009); (11) Ricci et al. (2010); (12) Gras-Velázquez & Ray (2005); (13) Koresko et al. (1997); (14) Natta et al. (2000); (15) Stempels & Piskunov (2003) (16) Appenzeller et al. (1986) and (17) Peterson et al. (subm.).

[c]N or S indicate if the source is the northern (N) or southern (S) of a binary system.

Table 2.2 Journal of observations.

Source	Obs. time	Settings (μm)[a]	Standard star	Spectral type standard star
AS 205 A	Apr 07	4.760, 4.662, 4.676, 4.773	BS 4757	A0
	Aug 07	4.730	BS 5812	B2.5
	Apr 08	4.730	BS 6084	B1
	Aug 09	5100, 5115	BS 5984	B0.5
DR Tau	Oct 07	4.716, 4.730, 4.833, 4.868	BS 3117, BS 838	B3, B8
	Dec 08	4.716, 4.946	BS 1791	B7
RU Lup	Apr 07	4.716, 4.730, 4.833, 4.929	BS 5883	B9
	Apr 08	4.730	BS 6084	B1
S CrA	Apr 07	4.730, 4.716	BS 6084	B1
	Aug 07	4.730	BS 7235, BS 7920	A0, A9
	Aug 08	4.868, 4.946	BS 6084, BS 7236	B1, B9
VV CrA A	Apr 07	4.716, 4.730, 4.840	BS 7362	A4
	Aug 07	4.770, 4.779	BS 7236	B9
	Aug 08	4.946	BS 7236	B9
VW Cha	Dec 08	4.716, 4.800, 4.820, 4.946	BS 5571, HR 4467	B2, B9
VZ Cha	Dec 08	4.716, 4.800, 4.820, 4.946	BS 5571, HR 4467	B2, B9

[a]The reference wavelength of a given setting is centered on the third detector.

2.2 Observations and sample

A sample of 70 disks around low-mass pre-main sequence stars was observed at high spectral resolving power ($\lambda/\Delta\lambda = 10^5$ or 3 km s^{-1}) with CRIRES mounted on UT1 at the Very Large Telescope (VLT) of the European Southern Observatory, Paranal, Chile. The CRIRES instrument (Käufl et al. 2004) is fed by an adaptive optics system (MACAO, Paufique et al. 2004), resulting in a typical spatial resolution of ~160-200 milli-arcsec along the slit. CRIRES has 4 detectors that each cover about 0.02 – 0.03 μm with gaps of about 0.006 μm at 4.7 μm. Staggered pairs of settings shifted in wavelength are observed to cover the detector gaps and produce continuous spectra.

The observations were taken during a period from April 21 2007 to January 3 2009. The parent sample is a broad selection of low-mass young stellar objects, consisting mostly of T Tauri stars and a few Herbig Ae stars. The full data set will be published in a future study (Brown et al. in prep.). Of the 70 sources, about 50 disks around T Tauri stars show clear CO emission lines. This paper focuses on a subsample of 8 of the 12 objects that show broad-based single peaked CO ro-vibrational line profiles. Their names and characteristic parameters are presented in Table 3.4, and their selection is justified in §3.2 and §4. Inclinations are unknown for the majority of the sources. Several of the sources in the sample are binaries, with the primary and secondary defined as A and B, respectively. The specific definition for each source's primary and secondary is taken from the literature, see Table 3.4. For S CrA, both A and B components show broad-based centrally peaked line profiles. For AS 205 and VV CrA, only the A component

has such single-peaked emission profiles. The B components show CO absorption (see Smith et al. 2009 for the case of VV CrA B). Thus, there is no obvious trend of the presence of these profiles with binarity of the system.

Ground-based M-band spectroscopy is usually dominated by strong sky emission lines (including CO itself) superimposed on a thermal continuum. Nodding with a throw of 10" was performed to correct for both the sky emission and the thermal continuum. In addition jittering with a random offset within a radius of 0.″5 was used to decrease systematics and to remove bad pixels. The weather conditions during the observations were usually good with optical seeing varying typically between 0.″5 – 1.″5. Even at times when the seeing was higher most of the light still passed through the 0.″2 slit because of the adaptive optics system. Observations of standard stars were done close in time to each science target with airmass differences of typically 0.05–0.1 in order to correct for telluric features.

The observations typically covered CO v = 1 − 0: R(8)–P(32) lines, where the notation indicates that most lines between R(8) and P(32) are observed, including, for example, the R(0) and P(1) lines. Lines from vibrationally excited levels as well as isotopologues are also included, specifically: CO v = 2 − 1: R(17)–P(26); CO v = 3 − 2: R(26)–P (21); CO v = 4 − 3: R(37)–P(15); ^{13}CO: R(24)–P(23); C^{18}O: R (17)–P(27); and C^{17}O: R(26)–P(22).

The wavelengths and dates of the observations can be found in Table 2.2. Each wavelength setting is centered on the third, in order of increasing wavelength, of the four detectors. As an example, the setting at 4.730 μm corresponds to a spectral range of 4.660 – 4.769 μm. Observations were sometimes taken during different seasons to shift the telluric lines relative to the source spectrum due to the reflex motion of the Earth. Combination of the two data sets then allows the reconstruction of the complete line profile, whereas a single epoch would have a gap due to the presence of a saturated telluric CO line. For 6 of the sources presented here, no evidence has been found that the line fluxes and profiles changed within this 1–1.5 yr period. For VW Cha and VZ Cha this information is not available since they were only observed once.

2.2.1 Data reduction

The spectra were reduced using standard methods for infrared spectroscopy (see Pontoppidan et al. 2008,for details). Dome flats were used for each setting to correct the images for pixel-to-pixel sensitivity differences in the detectors. A linearity correction was applied to the frames using the parametrization given in the CRIRES documentation. The nod pairs were then differenced to subtract the background. The data stack was co-added after correction for field distortion. Extraction of the 2-dimensional images to 1 dimensional spectra was done after the subtraction and combination of the 2-D frames tracing the source in the 2-D spectra. Additional spectra of well separated binaries were extracted as well during this procedure.

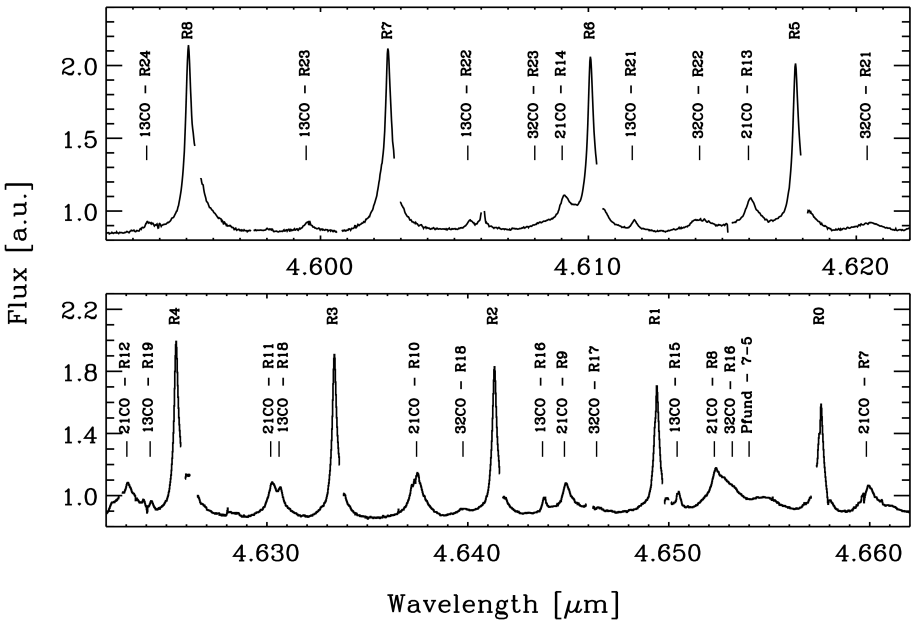

Figure 2.1 Part of the VLT-CRIRES spectrum of AS 205 A. The strong ^{12}CO lines are labelled with their *R*-band lower *J*-transition number and the other marked lines show detections of ^{12}CO v = 2–1, v = 3-2, ^{13}CO, and the Pfund-β line. The gaps in the spectrum are excised telluric features. For other parts of the AS 205 A spectrum, these gaps have been filled in by observations at different times of the year (see Fig. 2.2).

The spectra were subsequently wavelength calibrated by fitting the standard star atmospheric lines to an atmospheric model generated using the Reference Forward Model (RFM) code. This model is a line-by-line radiative transfer model developed at Oxford University based on Clough et al. (1982)[1]. The typical velocity accuracy is about 0.1–1 km s^{-1}, but can vary between settings, depending on the density of telluric lines. The last step in the reduction process was to correct for the strong telluric absorption lines in the spectra, by dividing the science spectra with the spectra taken of early-type photospheric standard stars. These hot stars have a strong hydrogen Pfund β (7-5) absorption line at 4.654 μm. Division by the standard star therefore introduces an artificial contribution to the emission line in the science spectra. However, Pfund β is detected in emission towards most of the sources prior to telluric correction. Early-type photospheric standard stars are otherwise rather featureless throughout the spectral band. Flux calibration was carried out by scaling to photometry from the Spitzer IRAC band 2 (see Table 3.4).

In Fig. 2.1 part of the reduced spectrum for the northern of the binary components of AS 205 is presented. This spectrum shows highly resolved ^{12}CO line profiles for the v = 1−0 transitions R(8)–R(0) and clear detections of ^{13}CO v= 1−0, CO v = 2 − 1 and v = 3 − 2 lines and the Pfund β line. An overview of parts of the spectra of the 8 single peaked sources is presented in Fig. 2.2.

2.3 Line profiles

2.3.1 ^{12}CO line profiles

The spectrally resolved fundamental CO emission lines from the sample of T Tauri stars observed with CRIRES show a broad variety of profiles. Often, the line profiles can be explained by Keplerian rotation, absorption by the disk or absorption by a foreground cloud (Brown et al., in prep). Fig. 2.3 shows a selection of emission line profiles of three basic shapes: A) narrow single-peaked, matched by a single Gaussian, B) double-peaked line profiles and C) single-peaked with broad wings. Lines that show absorption are not included due to the difficulty in determining the profile close to line center.

The CO line profiles of TW Hya fall in category A and likely arise from gas in a face-on disk in Keplerian rotation (e.g. Pontoppidan et al. 2008). Prototypical for category C are the line profiles of the source AS 205 A, which are by inspection qualitatively different from the double peaked profiles of sources like AA Tau and VV Ser (category B) because of their single narrow peak relative to a broad base. While categories A and B appear to be well understood (see below), the question is what the origin of the broad centrally peaked line profiles of category C is.

[1] http://www.atm.ox.ac.uk/RFM/

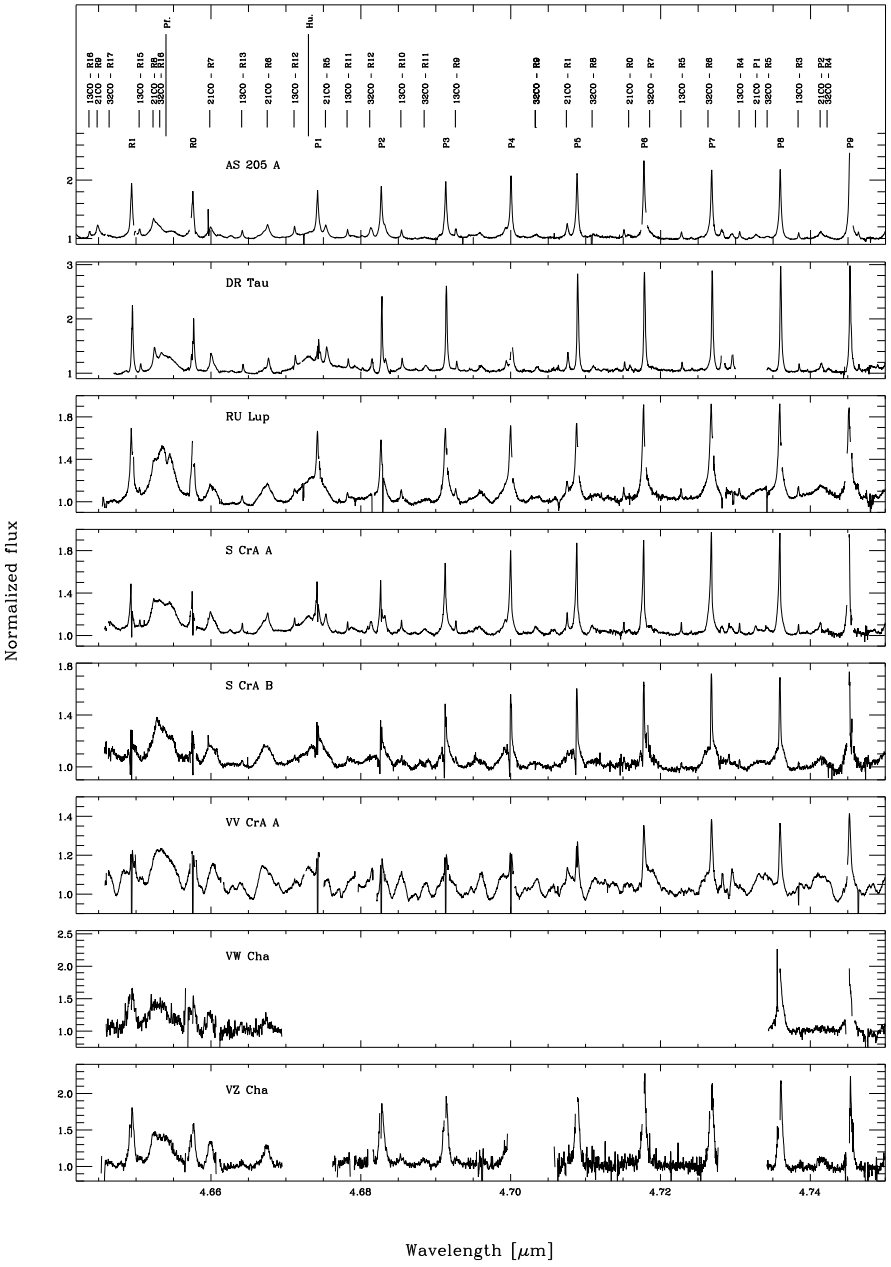

Figure 2.2 Partial spectra for the entire sample of sources with single peaked ^{12}CO lines. The HI Pfund β line at 4.655 μm and the Humphrey's line at 4.675 μm are included. The spikes seen in spectra of S CrA A, B and VV CrA A are narrow (self) absorption lines visible in the low J lines.

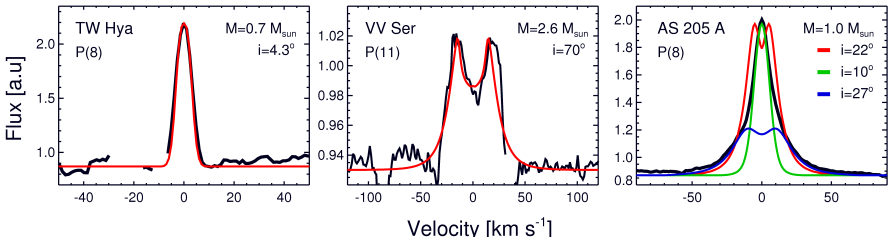

Figure 2.3 Modeled lines, plotted in red, are fitted to observed spectral lines in black of TW Hya, VV Ser and AS 205 A. Good fits could be found for VV Ser and TW Hya using a Keplerian model with a power-law temperature profile. No good fits could be found for AS 205 A. The optimal fit to the total line profile (red) using extended emission out to 10 AU, to the narrow inner part (green) and to the outer broader wings (blue) are presented in the right figure. See text for model parameters.

2.3.2 Keplerian disk model

To investigate to what extent the broad centrally peaked (category C) line profiles can be described by emission originating from gas circulating in the inner parts of the disk, a simple disk model of gas in Keplerian rotation adopted from Pontoppidan et al. (2008) is used.

Description of the model

The model includes a flat disk with constant radial surface density. The motions of the gas in the disk are described by Kepler's law. The disk is divided into emitting rings with radial sizes that are increasing logarithmically with radius. Each ring has a specific temperature. Local thermal equilibrium (LTE) is used as an approximation for describing the excitation of the emitting molecules, which means that the relative populations in a ro-vibrational level can be derived using the Boltzmann distribution at the given temperature in each emitting ring.

In the standard formulation, a power law is used to describe the temperature gradient throughout the disk, $T = T_0(R/R_0)^{-\alpha}$, where T is the gas temperature, R is the radius and T_0 is the temperature at the inner radius R_0. The other parameters are: the mass of the star $M_\star$; the inclination of the disk i; the outer radius of the disk $R_{\rm max}$; and a line broadening parameter $\Delta V_{\rm mod}$ which combines the instrumental broadening and any turbulent broadening. Several parameters are degenerate, including the stellar mass and disk inclination. Thus, this model is not used to derive the best estimates of the characteristic parameters of the sources. The aim is instead to explore the parameter space to see whether good fits can be found for the category C line profiles using basic Keplerian physics. The local line

profile is convolved with a Gaussian turbulent line FWHM broadening ($\Delta V_{\rm turb}$) which describes the local turbulence of the gas in the disk. The instrumental broadening ($\Delta V_{\rm instr}$) can also be represented by a Gaussian, which has a FWHM value of 3 km s^{-1} for CRIRES. The lowest value for $\Delta V_{\rm mod} = (\Delta V^2_{\rm turb} + \Delta V^2_{\rm instr})^{1/2}$ is therefore set to 3 km s^{-1} and any additional broadening represents an increase in the value of $\Delta V_{\rm turb}$. For temperatures up to 1000 K, typical of the molecular gas in the inner disk, the thermal broadening of the CO lines of up to 1.3 km s^{-1} is negligible.

Fits with a Keplerian model with a power-law temperature profile

The sources TW Hya, VV Ser and AS 205 A were chosen as illustration since their fundamental CO emission lines represent the three main different types of line profiles in our large sample. Each of these sources and their fits are presented here and shown in Fig. 2.3.

Single peaked narrow line profile -- TW Hya: A good fit was found to the narrow single peaked line profile of the TW Hya disk. This fit was achieved by using a low inclination angle of $i = 4.3°$, $\alpha = 0.4$, a stellar mass of 0.7 M$_\odot$, $R_0 = 0.1$ AU, $T_0 = 1100$ K, $R_{\rm max} = 1.5$ AU and $\Delta V_{\rm mod}$ =3 km s^{-1}, see the left plot in Fig. 2.3. The adopted stellar mass and disk inclination are taken from Pontoppidan et al. (2008). For this source, CO emission from the Keplerian disk model described above, convolved to the 3 km s^{-1} instrumental resolution of CRIRES, provides a good fit to all lines. Additional line broadening from turbulence is not needed to explain the line profiles. This low turbulence is consistent with the low turbulent velocity of ∼0.1 km s^{-1} inferred for the outer disk of TW Hya by Qi et al. (2006), although that value refers to much cooler gas at large radii in the disk.

Double peaked line profile -- VV Ser: VV Ser is an example of a disk with double peaked line profiles extending out to velocities of ± 40 km s^{-1}. VV Ser is a Herbig Ae/Be star of spectral type A2-B6 with a mass of 2.6 ± 0.2 M$_\odot$ and an inclination of 65-75^o (Pontoppidan et al. 2007). A good fit between the model and the data is shown in the center panel in Fig 2.3. The estimated parameters are $M_\star = 2.6$ M$_\odot$, $i = 70°$, $T_0 = 3500$ K, $\alpha = 0.45$, $R_0 = 0.08$ AU, $R_{\rm max} = 11$ AU and $\Delta V_{\rm mod}$ =3 km s^{-1}. However in this case the parameter space is rather large since smaller inclination angles will give equally good fits if a higher stellar mass is used. The main point here is that a good fit can readily be obtained with reasonable parameters for a Keplerian model.

Single peaked broad-based line profile -- AS 205 A: No equally good fit could be found for the emission lines from AS 205 A. An approximate fit is shown in red in the right plot of Fig. 2.3 with a model using an inclination angle of $i = 22°$, $R_0 = 0.04$ AU, $R_{\rm max} = 5$ AU, $\Delta V_{\rm mod}$ =3 km s^{-1}, $T_0 = 1100$ K, $\alpha = 0.3$, and a mass of 1.0 M$_\odot$. The mass is the same and the inclination angle is close to that

given by Andrews et al. (2009,1.0 $M_\odot$ and 25°, respectively). As for TW Hya, the millimeter data of Andrews et al. (2009) refer to much larger radii (typically >50 AU) than the CRIRES observations that the model is fitted to. A lower inclination angle of 10° gives a better fit to the narrow central part of the line but results in poor fitting of the outer wings of the profile, as presented by the green profile in Fig. 2.3. The blue line represents the best fit to the line wings, which is achieved by increasing the inclination angle to 27° and taking α to be 0.36.

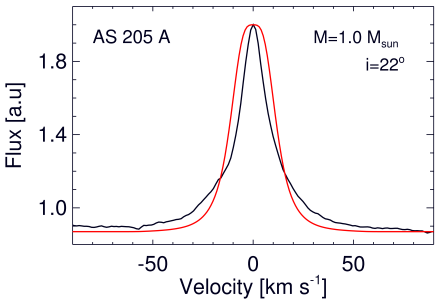

Figure 2.4 Fit to the broad-based single peaked line of AS 205 A (black) using a standard Keplerian model with a power-law temperature profile (red) including an enhanced line broadening parameter ($\Delta V_{\rm mod}$) of 8 km s^{-1}. The other parameters are $i = 22°$, $R_0 = 0.04$ AU, $R_{\rm max} = 5$ AU, $T_0 = 1100$ K, $\alpha = 0.3$ and a mass of 1.0 $M_\odot$ (as in §2.3.2).

One option to improve the fit to the AS 205 A data could be to increase the turbulent broadening so that the central dip is filled in. Indeed, increasing $\Delta V_{\rm mod}$ to 8 km s^{-1}, removes the central double peak (see Fig. 2.4). This fit is unable to simultaneously match both the narrow peak and the broad base of the profile, however.

In summary, the fits to TW Hya and VV Ser show that both narrow single peaked and double peaked line profiles can be reproduced with a simple Keplerian model with reasonable parameters. However a single peaked line with broad wings cannot be well explained with this type of standard Keplerian model as long as the temperature gradient is described by a continuous power-law.

Keplerian disk models with a non-standard temperature profile

Since disk models with a standard temperature and density power-law do not fit the data, one complementary approach is to investigate what physical distribution would be needed to reproduce the line profiles within a Keplerian model. For this, an iterative approach is used in which the observed line profile is 'inverted' to determine the temperature distribution that would be consistent with the data. Specifically, the disk is divided into rings and the temperature of each ring is

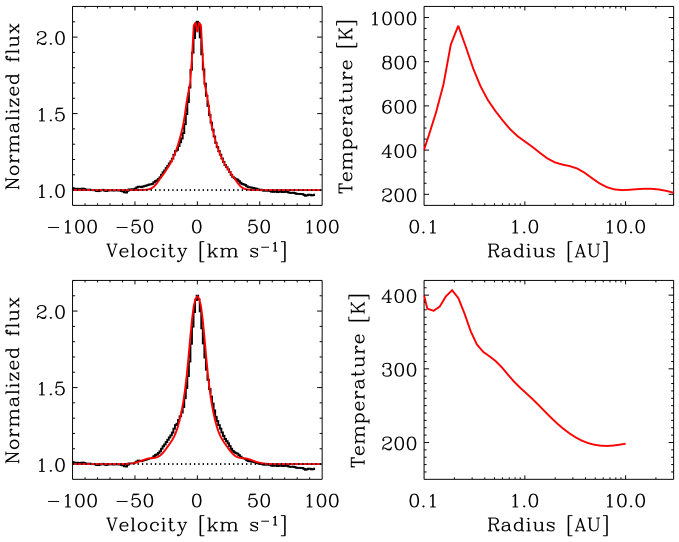

Figure 2.5 Left panel: Keplerian model (red) using an iterative inversion method to fit the velocity profile of the AS 205 A CO v = 1 – 0 P(8) line (black). Right panel: The excitation temperature as a function of radius needed to create the modeled lines. The models in the upper panels include extended emission out to 30 AU, a stellar mass of 1.4 $M_\odot$, an inclination of 25° and $\Delta V_{\rm mod}$=3 km s^{-1}. The models in the lower panels include emission out to 10 AU, a stellar mass of 1.0 $M_\odot$, an inclination of 22° and an increased $\Delta V_{\rm mod}$=7 km s^{-1}.

adjusted to match the line profile. The left panels of Fig. 2.5 present the model compared with the velocity profile of the AS 205 CO v = 1 – 0 P(8) line whereas the right plots show the corresponding excitation temperature profiles with radius. For LTE excitation and optically thin emission, the latter can also be viewed as an intensity profile with radius. The upper plots use the same parameters as in §2.3.2 for AS 205 A but with a higher stellar mass of 1.4 $M_\odot$, a higher inclination angle of i=25°and including extended emission out to 30 AU. The lower plots show a model using the same parameters as in §2.3.2 but with an extended emission out to 10 AU and increasing the $\Delta V_{\rm mod}$ to 7 km s^{-1}. Both of these models fit the line profiles well, illustrating that a Keplerian disk model with an unusual temperature distribution can explain the data. The emission is much more extended, however, than in the case of the standard disk models with a power-law temperature profile: out to 30 AU in the case of no turbulence or out to 10 AU with increasing $\Delta V_{\rm mod}$. These models will be further tested in §2.5.1 using the constraints on the spatial extent of the observed emission found in §2.4.3.

Table 2.3 The peakiness parameter P_{10}, the accretion luminosity and the line/continuum (L/C) ratio for a selected sample of protoplanetary disks.

Index number	Source	P_{10}[a]	L/C	Acc. lum. [log($L_\odot$)]	Ref.[b]
1	AA Tau	1.8 (0.2)	1.5	-1.6	1
2	AS 205 A	11.5 (1.0)	2.1	0.2[c]	2
3	CV Cha	4.1 (0.8)	1.3	-	-
4	CW Tau	3.0 (0.2)	1.4	-1.3	2
5	DF Tau	4.2 (0.5)	1.5	- 0.7	3
6	DR Tau	7.7 (0.8)	2.9	- 0.1	2
7	DoAr24E A	7.3 (2.0)	1.5	- 1.6	4
8	DoAr 44	7.7 (0.3)	1.4	-	-
9	EX Lup	10.8 (1.0)	1.3	-	-
10	FN Tau	3.3 (0.5)	1.5	-	-
11	GQ Lup	3.5 (0.5)	1.4	-	-
12	Haro 1-4	3.3 (0.5)	1.4	-	-
13	Haro 1-16	3.4 (0.4)	1.3	-	-
14	HD135344B	6.9 (0.3)	1.2	-0.9	5
15	HD142527	6.0 (0.5)	1.2	0.0	5
16	IRS 48	1.7 (0.2)	1.2	-	-
17	IRS 51	4.1 (0.4)	1.2	-	-
18	LkHa 330	5.2 (0.5)	1.3	-	-
19	RNO 90	4.5 (0.6)	1.5	-	-
20	RU Lup	15.1 (3.5)	1.8	- 0.4	3
21	RY Lup	3.3 (0.5)	1.2	-	-
22	S CrA A	13.4 (2.5)	2.0	-	-
23	S CrA B	18.8 (2.3)	1.8	-	-
24	SR 9	2.4 (0.6)	1.1	-1.4	4
25	SR 21	2.4 (0.3)	1.2	<-1.9	4
26	TW Hya	5.0 (0.5)	2.3	-1.4	3
27	VSSG1	4.7 (1.0)	1.5	- 0.4	4
28	VV CrA A	14.0 (3.0)	1.4	-	-
29	VV Ser	1.5 (0.2)	1.1	1.2	5
30	VW Cha	8.1 (0.5)	2.0	- 0.2	6
31	VZ Cha	7.7 (0.6)	2.2	- 1.1	6

[a]Values refer to an average of the lower J- transitions. Uncertainties are indicated in parentheses

[b]References - (1) Gullbring et al. (1998); (2) Valenti et al. (1993); (3) Herczeg & Hillenbrand (2008); (4) Natta et al. (2006); (5) Garcia Lopez et al. (2006); and (6) Hartmann et al. (1998).

[c]For both A and B component

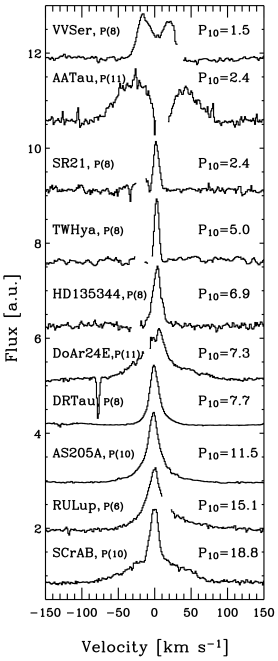

Figure 2.6 The line profile parameter P_{10}=$\Delta V_{10}/\Delta V_{90}$ is presented here for a sample of selected sources. Note that this parameter is clearly larger for the broad-based single peaked line profiles. The P_{10}-value is an average of the lower J-transition lines (up to P(14)). The J-transition corresponding to each plotted profile is given in the figure. The narrow absorption line seen toward DoAr24E A is due to ^{13}CO absorption in the foreground cloud.

2.3.3 Line profile parameter

A parameter is defined to quantify the difference in line profiles between the broad single peaked sources (category C) and the other sources in the sample. This so-called line profile parameter P_{10} describes the degree to which line profiles have a broad base relative to their peak. The line profile parameter P_{10} is therefore defined as the full width (ΔV_{10}) of the line at 10% of its height divided by the full width at 90% (ΔV_{90}) of its height, $P_{10} = \Delta V_{10}/\Delta V_{90}$. The broad-based single peaked lines (category C) have a higher value of the line profile parameter relative to the double and narrow single peaked lines, see Fig. 2.6.

A summary of the line profile parameter values for 31 selected T Tauri stars from the total sample of ∼50 T Tauri stars with CO emission is presented in Fig. 2.7 and Table 2.3. These 31 T Tauri stars were selected because their CO

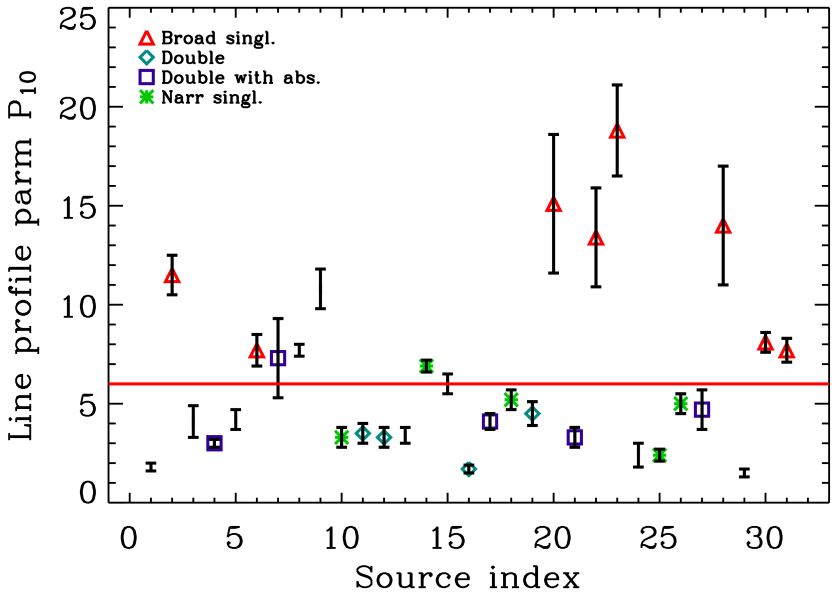

Figure 2.7 The line profile parameter P_{10} for different sources. The index numbers represent the different sources, see Table 1. Each type of line profile is given by a specific symbol. Data points without a symbol are for sources without clearly defined line profiles. The red line gives the maximum line profile parameter achieved using a standard Keplerian disk model with a power-law temperature profile.

emission line profiles have high S/N and are not contaminated by strong telluric or absorption lines. Figure 2.7 shows that the double peaked (turquoise diamonds) and narrow single peaked (green stars) sources all have a line profile parameter of <6. For reference, a Gaussian line profile has a P_{10}-value of 4.7. The selected sample of 8 broad centrally peaked sources (red triangles) all have a P_{10}-value of >6. An overview of the normalized and continuum-subtracted ^{12}CO P(8) line profiles of this subset is presented in Fig. 2.8. These lines are typically symmetric around line center and have a narrow top and a very broad base that extends out to ±100 km s^{-1} in several cases. Four other sources, DoAr24E A, DoAr44, EX Lup and HD135344B, also have higher (>6) P_{10}- values but are not selected for our sample (see §2.3.5 for source selection criteria).

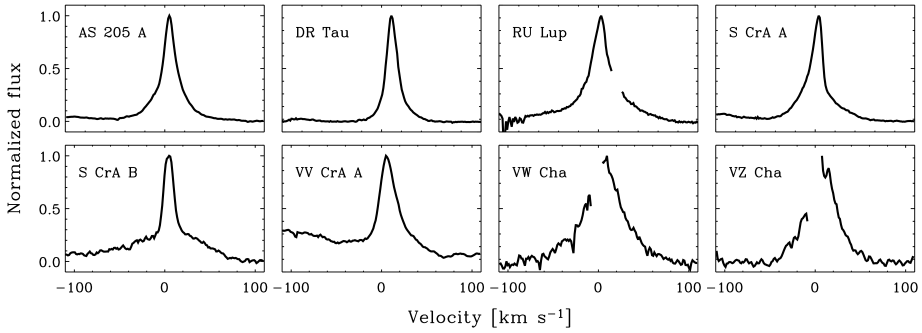

Figure 2.8 The P(8) ^{12}CO line is plotted for the entire sample broad-based single peaked sources, apart from VW Cha for which the P(10) line is presented because the P(8) line is affected by a strong telluric feature at the time of observation. The lines have been continuum subtracted and normalized. The asymmetry of the VV CrA A line is caused by line blending by the CO v = 3 – 2 R(5) line. This line overlap adds intensity on the blue side of the ^{12}CO P(8) line.

2.3.4 Model line profile parameters

To derive the maximum line profile parameter consistent with a standard Keplerian model with a power-law temperature profile, a grid of Keplerian line profiles was constructed. Three parameters in the model were set to fixed values that give strongly peaked line profiles; $T_0 = 1100$ K, $\alpha = 0.30$ and $\Delta V_{\rm mod} = 3$ km s^{-1}. The following parameters were varied between $M_\star = 0.5$ – 1.0 M$_\odot$, $i = 10$ – 80°, $R_0 =$ 0.04 – 1.0 AU and $R_{\rm max} = 5$ – 100 AU and the P_{10}- value was calculated for each produced line profile. An overview of the P_{10}-values versus inclination is shown in Fig. 2.9. It is found that a typical standard Keplerian model with a power-law temperature profile can achieve a maximum P_{10}-value of about 6, with the highest values found at low inclination. This conclusion is unchanged if $\Delta V_{\rm mod}$ is increased to values as large as ∼10 km s^{-1}. The upper limit of $P_{10} \approx 6$ that the Keplerian model can reproduce is presented as a red line in Fig. 2.7. Figure 2.9 also indicates that the inclination of the source, invoked to explain the different widths of Herbig Ae disk profiles (Blake & Boogert 2004), should not affect the value of P_{10} significantly except at very low inclinations, since it enters both ΔV_{10} and ΔV_{90}.

Note that the Keplerian models always require a low inclination angle of 20° – 30° to obtain high values of the line profile parameter P_{10}, regardless of whether or not a large turbulent broadening is included. If inclination angles within 5° of the range $i = 20$ – 30° are considered necessary for the broad single peaked line profiles, then 6 ± 3 sources of the total sample of 50 T Tauri stars would have broad, single-peaked line profiles, which is consistent with our subsample

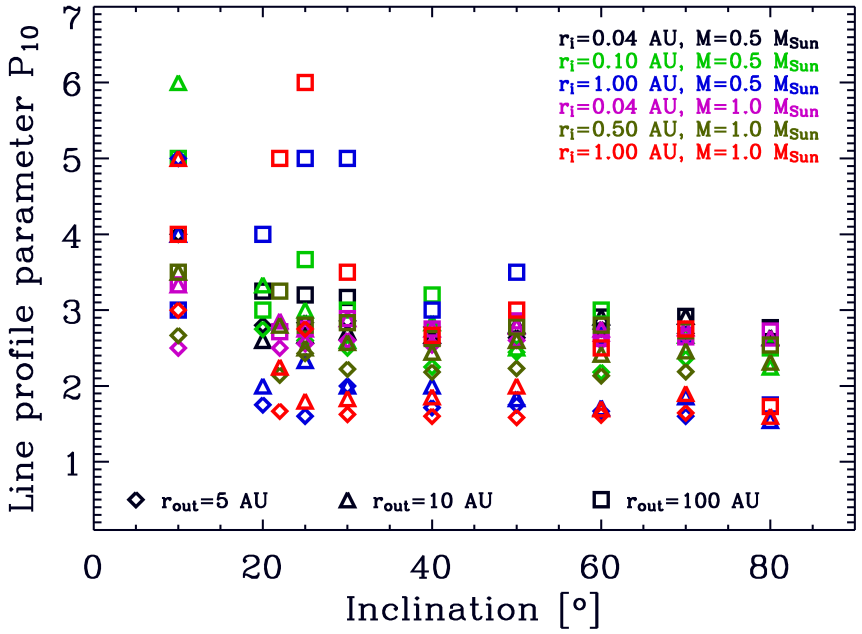

Figure 2.9 Line profile parameter P_{10} versus inclination for a large model grid of standard Keplerian models with a power-law temperature profile. Note that P_{10} does not become larger than 6 and shows no trend with inclination for $i > 20^o$.

of 8 sources. Millimeter interferometry data for AS 205 A and DR Tau yield inclinations of 25° and 37± 3°, respectively (Andrews 2008, Andrews et al. 2009, Isella et al. 2009), which are roughly consistent with the model requirements.

2.3.5 P_{10}-value versus the line-to-continuum ratio and source selection

The broad-based single peaked sources are also noteworthy for having high line-to-continuum (L/C) ratios in many lines, including the resolved CO ro-vibrational lines discussed here and H_2O lines in Salyk et al. (2008). Here, the L/C-ratio is defined as the ratio between the peak line flux relative to the continuum flux. The L/C ratios of the ^{12}CO lines have been plotted against the P_{10}-values in Fig. 2.10. Typical uncertainties of the line-to-continuum ratio are ±0.1. Seven of the sources stand out clearly with high line profile parameters and high line-to-continuum ratios. Figure 2.10 is used to set the criteria ($P_{10} > 6$ and $L/C > 1.6$) for the selection of the broad-based single peaked line profiles (category C). The lower

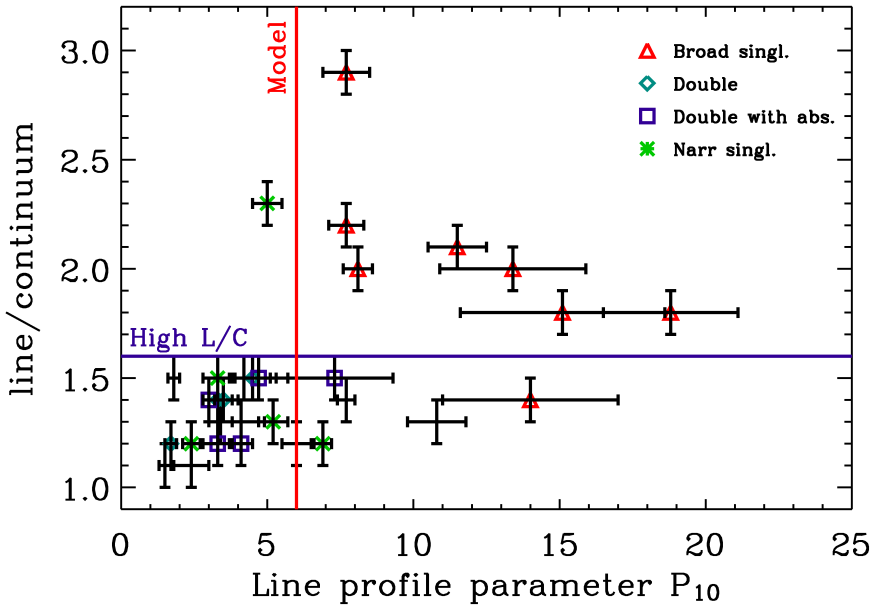

Figure 2.10 The line to continuum ratio relative to the line profile parameter P_{10}. Each type of line profile is given by a specific symbol. Data points without a symbol do not have a clearly defined line profile. The broad single peaked sample includes sources with either a line/continuum ratio > 1.6 (blue line) and $P_{10} > 6$ (red line) or solely $P_{10} > 10$.

limit for the P_{10}-value ($P_{10} > 6$) for the sample is set to match the maximum line profile parameter for a line that the standard Keplerian model with a power-law temperature profile can produce (§3.4). The line-to-continuum constraint of L/C > 1.6 is rather arbitrary, based on the observation that the majority of the sources have a lower value. Two other sources, EX Lup and VV CrA A, have L/C ratios less than 1.6 but have such a high line profile parameter (>10) that they are considered to belong to the category C profile sample. However, EX Lup is a variable source that underwent an outburst in 2008. The variation of the CO line profiles from EX Lup during and after the outburst are discussed in Goto et al. (subm.). DoAr 44 and DoAr24E A are borderline cases and are not included here because their profiles are contaminated by absorption, limiting the analysis. HD135344B is also excluded from the sample due to the combination of having both a low L/C ratio and a P_{10}-value close to 6. In addition HD135344B is a well-known face-on disk whose profile has been well fitted with a Keplerian model (Pontoppidan et al. 2008, Brown et al. 2009, Grady et al. 2009). Line profiles emitted by disks with

Table 2.4 List of CO isotopologues and the ^{12}CO v = 2 – 1, v = 3 – 2 and v = 4 – 3 lines.

Source[a]	^{12}CO	^{13}CO	CO v = 2 – 1	CO v = 3 – 2	CO v = 4 – 3	C^{18}O
AS 205 A	x	x	x	x	x	x
DR Tau	x	x	x	x	x	x
RU Lup	x	x	x	x	-	-
S CrA A	x, a	x	x	x	x	x
S CrA B	x, a	x	x	x	-	-
VV CrA A	x, a	x, a	x	x	x	a
VW Cha	x	a	x	-	-	-
VZ Cha	x	-	x	x	-	-

[a]x = detection in emission, a = detection in absorption and - = no detection.

a low inclination angle can have a line profile parameter close to 6, as shown in Fig. 2.9. These selection criteria yield in total 8 sources that are included in the broad-based single peaked sample; these sources are marked with red triangles in Fig. 2.10.

2.4 Characteristics for the sources with broad single peaked lines

In §3, we showed that our selected sources with broad single peaked line profiles (category C) cannot be reproduced well with a standard Keplerian model with a power-law temperature profile. In the following sections, we analyze the observational characteristics of the emission to obtain further constraints on the origin.

2.4.1 Line profiles of CO isotopologues and the v = 2 – 1 CO lines

Table 2.4 summarizes the lines seen in the spectra of the broad single peaked sources, including if they are detected in absorption, emission or both. In the richest spectrum, that of AS 205 A, lines of ^{13}CO, C^{18}O, CO v = 1 – 0, v = 2 – 1, v = 3 – 2 and v = 4 – 3 are all detected. All of the sources, besides VZ Cha, have detections of ^{13}CO. Four sources have a C^{18}O detection in emission. In addition every source in the sample has detections of CO v = 2 – 1, 7 of 8 sources of CO v = 3 – 2 and 4 of 8 sources of CO v = 4 – 3.

Fig. 2.11 compares the stacked, normalized and continuum-subtracted line profiles for ^{13}CO v = 1 – 0, ^{12}CO v = 1 – 0, ^{12}CO v = 2 – 1 and ^{12}CO v = 3 – 2. All of the isotopologues and the higher ro-vibrational transitions also show a broad-based single peaked line profile. However, the profiles of the ^{12}CO and ^{13}CO v = 1 – 0 lines match exactly for only one source, AS 205 A. For the other sources, DR Tau,

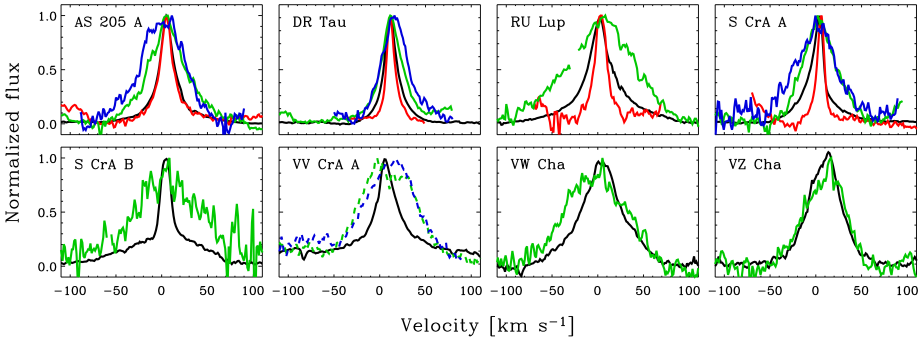

Figure 2.11 ^{13}CO (red), CO v = 2 – 1 (green) and v = 3 – 2 (blue) line are plotted on top of the CO v = 1 – 0 lines (black) for the broad-based single peaked CO emitting sample of T Tauri stars. Dashed lines indicate that the line profile is constructed by stacked lines that all are to some degree affected by line overlap. All profles have been normalized to a peak flux of unity.

RU Lup, and S CrA A, the ^{13}CO lines are narrower than the ^{12}CO v = 1 – 0 lines.

The width of the CO v = 1 – 0 lines at 10% of their height (see Table 2.6) are in general narrower than the CO v = 2 – 1 and v = 3 – 2 lines by about 60-80% which can be seen in Fig. 2.11. Najita et al. (2003) also found a similar trend of broader higher vibrational lines in their data. The difference in width between the lower and higher vibrational lines in our sample may reflect a physical difference in the location of the emitting gas. The high fraction of CO v = 2 – 1 and 3 – 2 detections in our sample of broad-based single peaked line sources is consistent with the Najita et al. (2003) sample, where 9 of their 12 CO sources have detections of v = 2 – 1 emission and 3 out of 12 sources have v = 3 – 2 detections. However it is difficult to categorize their line profiles due to the lower spectral resolution.

Two component fits

The line profiles shown in Fig. 2.8 are generally not well fit by a single Gaussian profile. A good example of this is the CO emission line profiles of S CrA B, which clearly consist of two components. An interesting aspect is that the narrow component stands out very prominently in the low J-transitions but progressively decreases in intensity with higher J-transitions relative to the broad component (Fig. 2.12). The simplest explanation is that the components arise from different locations where the narrow component has a lower rotational temperature than the broad component. This is not as clearly seen for the other 7 sources in the sample. However, Najita et al. (2003) see a similar phenomenon in the broad-based single peaked source GW Ori.

The line profiles from S CrA A and GW Ori support a hypothesis in which

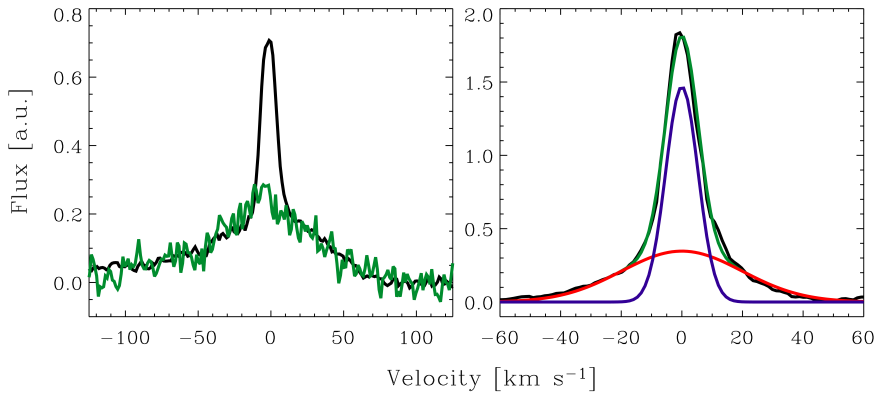

Figure 2.12 Left: The higher J-transition ^{12}CO P(32) (green) is plotted on top of the lower J-transition ^{12}CO P(8) (black) for S CrA B. The narrow component of the ^{12}CO P(8) line decreases with increasing excitation. Right: Two Gaussian fitted lines (in red and blue) to the CO v = 1 − 0 P(7) line of DR Tau (black). The green line represents the sum of the two Gaussian fits.

two physical components combine to form broad centrally peaked line profiles. We therefore fit the line profiles of all sources with two Gaussians to investigate the possibility that the broad-based centrally peaked line profiles consist of two physical components. In the fits, all 6 Gaussian parameters (the two widths, amplitudes and central wavelengths) are left free. For example, Fig. 2.12 shows that the CO v = 1 − 0 P(7) line from DR Tau is well-fit with two Gaussian profiles, one narrow and one broad.

Two Gaussian profiles are needed for 7 of the 8 broad-based single peaked sources to find an optimal fit to their line profiles. The resulting FWHM$_B$, FWHM$_N$, V_B(CO) and V_N(CO) are presented in Table 2.5. These results show that the broad-based single peaked line profiles (category C) can be fitted using a narrow component with a FWHM varying between ∼ 10 - 26 km s^{-1} and a broad component with FWHM of ∼ 40 - 100 km s^{-1}. The central velocities of the two components are generally the same within the errors. Only the line profile of VZ Cha was adequately fit with a single Gaussian.

The results presented in Table 2.5 are based on fits to the CO v = 1 − 0 lines that are chosen to be as uncontaminated from line overlap as possible. The uncertainties in Table 2.5 are the standard deviations of the fit parameters of individually fitted lines. The spread within a parameter for a given source is caused by uncertainties in the Gaussian fits, by overlapping weaker lines that may affect the width and position of the broad component, by errors of around ∼1.0 km s^{-1} in the wavelength calibration (which can vary between different detectors, see §

Table 2.5 The FWHM of the broad and narrow components and their average heliocentric velocities V_B(CO) and V_N(CO) relative to literature values of the heliocentric velocities for the stars V_h(star).

Source	FWHM$_B$ km s^{-1}	FWHM$_N$ km s^{-1}	V_B(CO) km s^{-1}	V_N(CO) km s^{-1}	V_h(star) km s^{-1}	Ref.[a]
AS 205 A	61.3 (16.3)	14.8 (1.7)	-4.4 (4.8)	-6.2 (0.3)	-9.4 (1.5)	1
DR Tau	39.8 (6.3)	13.1 (0.9)	26.9 (1.3)	24.4 (0.7)	27.6 (2.0)	3
RU Lup	96.8 (11.0)	24.0 (3.9)	0.4 (7.0)	-3.9 (1.1)	-0.9 (1.2)	1
S CrA A	50.2 (6.7)	10.7 (1.2)	-9.2 (1.4)	-5.0 (0.7)	0.9 (0.9)	2
S CrA B	97.6 (17.7)	12.3 (0.5)	-4.7 (3.5)	-3.5 (0.3)	0.9 (0.9)[b]	2
VV CrA A[c]	-	19.3 (2.0)	-	-0.9 (0.2)	-	-
VW Cha	70.6 (3.1)	26.6 (2.2)	15.4 (1.4)	15.1 (1.9)	17. 2 (2.0)	2
VZ Cha[d]	45.1 (2.6)	-	19.1 (1.7)	-	16.3 (0.6)	2

[a]References. - (1) Melo (2003); (2) Guenther et al. (2007) and (3) Ardila et al. (2002).
[b]Taken to be the same as S CrA A since in the literature only a value for S CrA is given
[c]Broad component could not be determined due to large amount of line overlap.
[d]Optimal fits with one Gaussian curve, results presented in the broad component columns.

Table 2.6 The averaged line profile parameter P_{10} for high and low J-transitions for the sample of sources with single peaked CO v = 1 − 0 emission lines. ΔV_{10} is the averaged width of the line at 10% of its height.

	P_{10}		
Source	(low J)	(high J)	ΔV_{10} [km s^{-1}]
AS 205 A	11.5 (0.5)[a]	-	62.8 (3.9)
DR Tau	7.7 (0.8)	6.6 (0.6)	40.2 (1.0)
RU Lup	15.1 (3.5)	10.5 (2.3)	109 (11.1)
S CrA A	13.4 (2.5)	7.9 (0.2)	56.9 (3.4)
S CrA B	18.8 (2.3)	12.5 (1.0)	102.6 (6.9)
VW Cha	8.1 (0.5)	8.4 (0.3)	115.0 (7.0)
VZ Cha	7.7 (0.6)	7.7 (0.9)	79.2 (2.4)

[a]Value in parentheses indicates the spread in P_{10} for different J. Low-J includes selected lines up to P(14). High-J includes lines from P(22) to P(32).

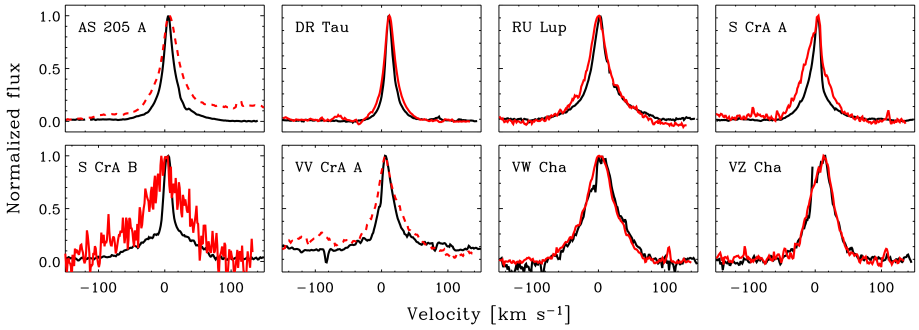

Figure 2.13 Comparison of the lower J and higher J profiles. The red line represents the stacked higher J-transitions (J = P(22)-P(32)) and the black line the lower J-transitions (up to J = P(14)) of v = 1−0 CO. The baseline for the higher stacked J-transitions for AS 205 A and VV CrA A (dashed red) is not straight because of line overlap and blend. All profiles have been normalized to a peak flux of unity.

2.2.1), and degeneracies of the fits between the broad and the narrow component. The large amount of line overlap in VV CrA A makes measurements of the broad component highly unreliable so the fits are not presented here.

Table 2.6 and Fig. 2.13 show that the relative width of the peak and base as represented in P_{10} is approximately constant with increasing J for most of the selected category C sources, with the exceptions of S CrA A and B. For these two sources the P_{10}-value decreases with increasing J (Table 2.6) and the line profiles become dominated by the broad wings at the higher J-transitions, see Fig. 2.12. AS 205 A and VV CrA A are excluded in the calculations of the line profile parameter because of their large amount of overlapping lines that cause difficulties in reliably measuring the 10% and 90% line widths (for AS 205 A, just in the higher J-transitions, see Fig. 2.13). The lack of variation in P_{10} towards higher J-transitions for all sources besides S CrA A and B, combined with the absence of a velocity shift, suggest that the broad and narrow components may be formed in related physical regions.

Central velocities

The central velocities of the CO gas and stellar photosphere are compared to look for differences indicative of a wind or outflow, which could explain the narrow low velocity peak. The stellar radial velocities in Table 2.5 are taken from literature measurements of photospheric optical absorption lines. The photospheric absorption lines for our sample of sources are generally heavily veiled by continuum emission related to accretion, leading to uncertainties in the stellar velocity measurements of the order of 1-2 km s^{-1}.

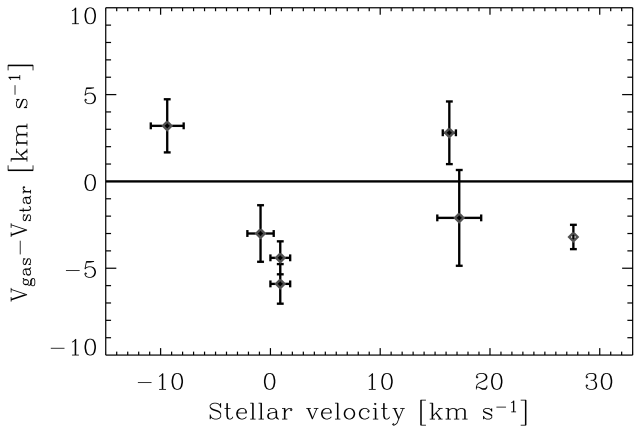

Figure 2.14 Velocity shifts V_{gas} - V_{star} as functions of V_{star}. The gas velocity refers to the central velocity of the narrow component of the CO v = 1 – 0 lines.

The differences between the molecular gas radial velocity of the narrow component and the stellar radial velocity are small with shifts of $|V_{CO}$ - $V_{star}| \lesssim 5$ km s^{-1}, see Fig. 2.14. The shifts are more commonly seen towards the blue rather than the red, indicating that the CO gas is moving towards us relative to the star. However, the velocity shifts are only 1– 2σ and may not be significant.

The small velocity differences rule out an origin of the lines in a fast moving disk wind or outflow. However it is still possible that the lines are emitted by gas in a slow disk wind. Najita et al. (2003) also do not see any significant velocity shifts between the radial velocity of the star and the gas within their few km s^{-1} uncertainties.

2.4.2 Excitation temperatures

Rotational temperatures

The extracted fluxes of the ^{12}CO v = 1 – 0 and ^{13}CO lines are used to produce excitation diagrams and thus calculate the gas rotational temperatures. This calculation is done by using the Boltzmann distribution, which assumes that the excitation in the gas can be characterized by a single excitation temperature and that the emission is optically thin;

$$\frac{N_i}{g_i} = \frac{N_\nu}{Q_r(T_{\rm rot})} e^{-\frac{E_i}{kT_{\rm rot}}} \tag{2.1}$$

Table 2.7 Rotational temperatures $T_{\rm rot}$ derived from the ^{13}CO lines, together with the vibrational temperatures $T_{\rm vib}$.

Source	$T_{\rm rot}$ [K]	$T_{\rm vib}[K]$
AS 205 A	550 ± 40	1740 ± 150
DR Tau	510 ± 40	1680 ± 140
RU Lup	360 ± 20	-
S CrA A	420 ± 30	1730 ± 140

and where the column density N_i of the upper level i is described by,

$$N_i = \frac{4\pi F_i}{\Omega A_{ij} h\nu} \tag{2.2}$$

where the solid angle $\Omega = D_{\rm em}/d^2$ includes the emitting area $D_{\rm em}$ and the distance d to the object. The other quantities are the Einstein coefficient A_{ij} [s^{-1}], the frequency ν [cm^{-1}] and the measured line flux F_i [W m^{-2}], the statistical weight g_i of the upper level, the total column density N_v for vibrational level v, the excitation temperature $T_{\rm ex}$ and the rotational partition function $Q_r(T_{\rm ex})$. Plotting the upper energy levels E_i against $\ell{\rm n}(F_i/A_{ij}\nu g_i)$ will give the rotational temperature $T_{\rm rot}$ by measuring the slope of the fitted line given by -1/$T_{\rm rot}$.

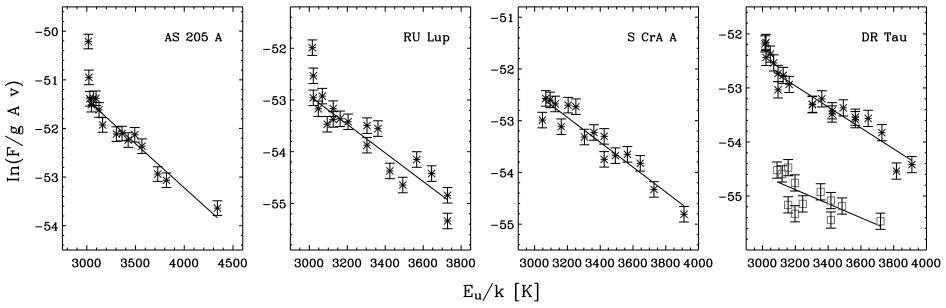

Figure 2.15 Rotational diagrams for T-Tauri stars AS 205 A, DR Tau, RU Lup and S CrA A. Blue stars represent ^{13}CO lines and green squares C^{18}O lines.

The rotation diagrams for the ^{12}CO lines are not linear, which suggests that the lines are optically thick. In addition, UV-pumping can cause non-linearity between the different transitions (Krotkov et al. 1980). To overcome this problem, rotational temperatures have been estimated using only the ^{13}CO emission lines for the 4 sources, AS 205 A, DR Tau, RU Lup and S CrA A, for which sufficiently high S/N emission lines are detected, see Fig. 2.15 and Table 2.7. The relative error of the line fluxes is taken to be 15% based on the noise in the spectra and

uncertainties in the baseline fits. Only lines with $J_u > 1$ are taken into account in the fit.

While ^{13}CO is significantly less abundant than ^{12}CO, ^{13}CO lines may also be optically thick. ^{13}CO lines with $\tau \approx 1$ have, for example, been seen in the disk around Herbig star AB Aur by Blake & Boogert (2004). The inferred rotation temperatures of the 4 sources span 300–600 K, which is lower than 1100–1300 K found for the T Tauri sample of Najita et al. (2003) but within the temperature interval of 250–800 K given in Salyk et al. (2009). The discrepancy with Najita et al. (2003) may arise from differences in methodology. Najita et al. (2003) fit ^{12}CO data covering lines with upper energies levels of up to 10^4 K, which they assume to be optically thin. They performed a linear fitting based on this assumption, but curvature in their rotation diagrams indicates that their ^{12}CO lines are likely also optically thick, leading to uncertainties in their extracted temperatures. Another explanation for the temperature difference may be the lack of higher J-transitions in our data set. However, AS 205 A includes ^{13}CO transitions up to E_i = 4400 K, and still has a lower temperature of 550 ± 40 K. The temperature estimates by Salyk et al. (2009) based on ^{12}CO should be more reliable since they took optical depth effects into account. In addition, a rotational temperature of 770 ± 140 K has been estimated for DR Tau using the C^{18}O lines, which is close to the temperature of 510 ± 40 K given by the ^{13}CO lines (Fig. 2.15). If the two highest-J ^{13}CO lines are excluded from the fit, the ^{13}CO rotational temperature increases to 610 ± 70 K, which is consistent with the C^{18}O temperature within the error bars. These two high-J ^{13}CO lines are very weak and their fluxes may have been underestimated.

We determine the ^{13}CO/C^{18}O ratio for DR Tau to examine whether the ^{13}CO emission is indeed optically thin. The ratio is calculated by comparing the fluxes in the R(5) and P(16) lines for ^{13}CO with the R(5) and P(17) lines for C^{18}O, chosen because they are not blended and have similar J. This gives ^{13}CO/C^{18}O = 6.3 ± 1.0 which is close to the overall abundance ratio of ^{13}CO/C^{18}O = 8.5 observed in the solar neighborhood (Wilson & Rood 1994). The optical depth of ^{13}CO is estimated to be $\tau = 0.3 \pm 0.2$. Inferred column densities and emitting areas will be presented in Brown et al. (in prep.), based on combined fits to the ^{12}CO and ^{13}CO lines.

Vibrational temperatures

Vibrational temperatures are determined for the three sources, AS 205 A, DR Tau and S CrA A, for which high S/N ^{12}CO data exist for several vibrational transitions (see Fig. 2.16). The vibrational temperatures are calculated using the same relation between the flux of the lines and the upper energy levels as presented in equations 2.1 and 2.2. The assumption made here is that every vibrational level has the same rotational temperature. The only difference is that $\ell n(F_i/A_{ij}\nu)$ instead of $\ell n(F_i/A_{ij}\nu g_i)$, is plotted vs the upper energy levels E_i to extract the vibrational temperature $T_{\rm vib}$ since the statistical weights of the vibrational levels

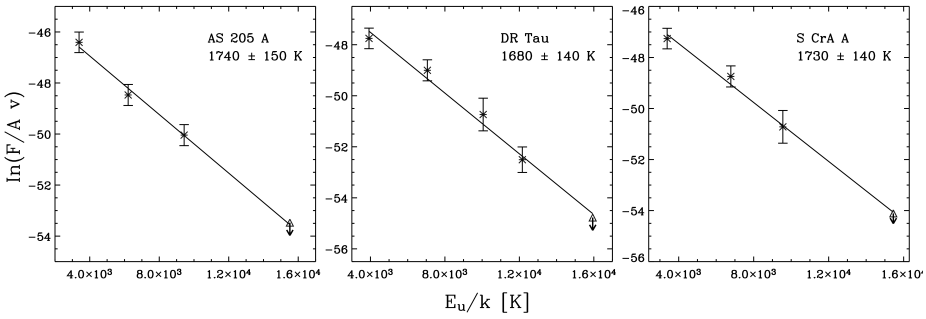

Figure 2.16 Vibrational diagrams for AS 205 A, DR Tau and S CrA A. Triangles represents upper limits.

are the same. One clear line, close in J-level and without strong line overlap, is chosen per ro-vibrational level (CO v = 1 – 0, v = 2 – 1 etc.) to extract the line fluxes.

The inferred vibrational temperatures are 1740 ± 150 K for AS 205 A, 1680 ± 140 K for DR Tau and 1730 ± 140 K for S CrA A. The same fits have been done without including the ^{12}CO v = 1 – 0 lines since the lines within this band can be more optically thick than those for the higher vibrational transitions. However, excluding the ^{12}CO v = 1 – 0 lines does not significantly change the results within the uncertainties. The upper limits of the v = 5 – 4 flux have been estimated using $F = 1.065\ I_{peak}\ \Delta V$, where the ΔV is taken to be the same as that of a CO v = 3 – 2 line and the amplitude $I_{peak} = 3\sigma/bin^{-1/2}$, where the parameter bin is the number of pixels within ΔV and σ is the rms of a clean part of the spectrum where the line of interest is expected. The detection level is set to 3σ.

The vibrational temperatures of ~1700 K are in general higher than the rotational temperatures derived from the ^{13}CO lines of 300-600 K. The inferred temperatures can be compared to Brittain et al. (2007) who find a lower rotational excitation temperature of ~200 K compared with a vibrational temperature of 5600 ± 800 K for the disk around the Herbig Ae star HD 141569. Similarly, van der Plas et al. (subm.) detect lower rotational temperatures of ~1000 K relative to vibrational values of ~6000 – 9000 K for three other Herbig Ae/Be stars. Both papers interpret the higher vibrational temperatures as caused by UV-pumping into the higher vibrational levels.

The results presented here indicate that UV-pumping may also be an important process for populating the higher vibrational levels in disks around T Tauri stars, especially for the broad-based single peaked sources. The rotation/vibration temperature differences in Brittain et al. (2007) and van der Plas et al. (subm.) are, however, much larger than those derived here. This may be due to the stronger UV fields from Herbig Ae/Be stars than T Tauri stars in the wavelength range

Table 2.8 The upper limit on the projected radial extent ΔR_{line} of the line emission, together with ΔR_{instr}.

Source	ΔR_{instr} [a] [AU]	ΔR_{line} [AU]
AS 205 A	15.1 ± 0.1	<2.1
DR Tau	14.5 ± 0.1	<1.7
RU Lup	17.9 ± 0.2	<2.5
S CrA A	15.9 ± 0.2	<2.0
S CrA B[b]	-	-
VV CrA A[b]	16.6 ± 0.5	-
VW Cha	23.4 ± 2.3	<10.4
VZ Cha	20.7 ± 1.0	<6.3

[a]See text for definition
[b]Contamination by companion star.

where CO is UV-pumped.

Additional UV flux above the stellar photosphere can be produced by accretion (Valenti et al. 2000). Table 2.3 includes accretion luminosities taken from the literature for our T Tauri stars. These accretion luminosities are based on measurements of the hydrogen continua or Hα line emission from the sources. The average accretion luminosity for those broad-based single peaked lines for which accretion luminosities have been measured, is 0.5 $L_\odot$. This value is higher than the average accretion luminosity of 0.1 $L_\odot$ which is calculated for the rest of the sample of disks that are shown in Table 2.3. The strong Pfund-β lines observed in our data provide an additional confirmation of ongoing strong accretion (see Fig. 2.2). Higher accretion rates lead to higher UV fluxes, which, in turn, increase the UV pumping rate of CO into higher vibrational states. Quantitative estimates of the effect have been made by Brown et al. (in prep.) using the actual observed UV spectra for stars with spectral types A–K in an UV excitation model. Even if the enhanced UV from accretion for the T Tauri stars is included, however, the resulting vibrational excitation temperatures for a K-type star with additional UV due to accretion are still lower than those using an A-star spectrum. For the v = 1 − 0 emission, the question remains how much UV-fluorescence contributes relative to thermal excitation.

2.4.3 Lack of extended emission

Information about the spatial extent of the CO emission from broad-based single peaked sources is an important ingredient for constraining models of their origin. The variance or formal second moment μ_2 of the spectral trace is calculated at each wavelength from the 2-dimensional spectrum, according to the following equation.

$$\mu_2 = \Sigma(x_i - C)^2 \times F_i / \Sigma F_i \tag{2.3}$$

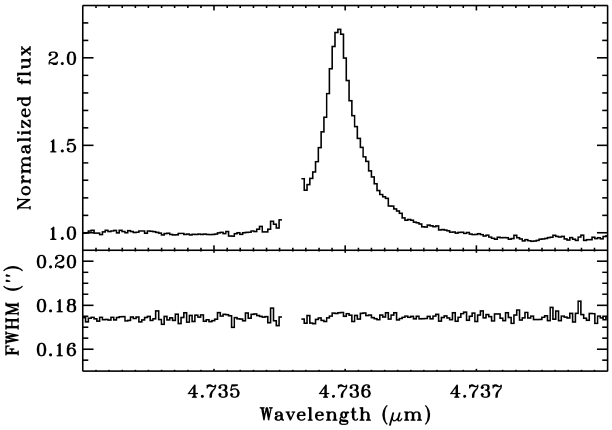

Figure 2.17 Top: The spectral line CO v = 1 − 0 P(8) for AS 205. Bottom: The FWHM of the spatial profile of the above spectrum at each individual wavelength point. No increase in FWHM is seen at the position of the line.

where x_i is the spatial position, F_i is the flux at that point and C is the centroid position computed from $C = \Sigma x_i \times F_i / \Sigma F_i$.

For continuum emission, the average value of the second moment reflects the spatial resolution provided by the AO system, assuming that the continuum is not spatially extended. If the line emission is spatially extented, the values of μ_2 will be larger than the noise in the continuum μ_2 signal at wavelengths where the line emits. There is no significant detection of extended line emission for any of our sources, see Fig. 2.17 and Fig. 2.18. An upper limit on the radial extent of the line emission, ΔR_{line}, is therefore calculated using the formula $\Delta R_{line}{}^2 \leq (\Delta R_{instr} + \sigma_{\Delta R})^2 - \Delta R_{instr}{}^2$, where ΔR^2_{instr} is equal to the mean of $\mu_2/2$ of the continuum and $\sigma_{\Delta R}$ is the standard deviation of $(\mu_2/2)^{1/2}$. The values listed in Table 2.8 include an additional correction factor $(1 + C/L)$, where C/L is the continuum/line flux ratio, because the total centroid is diluted by the continuum flux. These results show that most of the projected CO emission must originate from within a few AU for AS 205 A, DR Tau, RU Lup and S CrA A. S CrA B and VV CrA A (not shown) have a feature close to the central velocity of the line, however this can be explained by contamination from the companion star. The small feature seen for S CrA A may be a detection of extended line emission. VW Cha and VZ Cha have higher upper limits of the projected radial line extent of 10.4 and 6.3 AU respectively which is caused by a higher noise in the second moment of the continuum emission.

Since the position angle of the slit is arbitrary with respect to that of the disks in our observations, an additional check on the lack of radial extended emission is provided by the different spatial line profiles of the stacked CO v = 1 − 0 lines of AS 205 A, DR Tau and S CrA A taken at 3 different rotational angles. All three

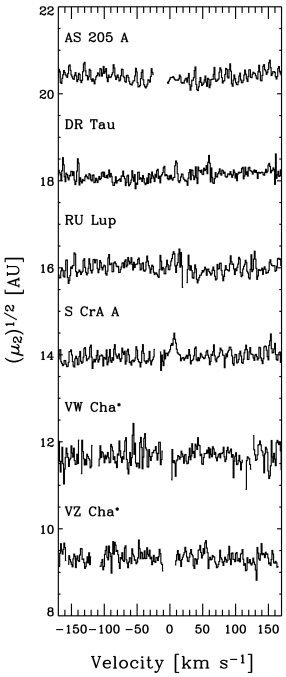

Figure 2.18 The stacked square root of the formal second moment $(\mu_2)^{1/2}$ of the spectral trace for the ^{12}CO emission lines. About 5–10 clean lines for each source were used for stacking. The square root of the second moment $(\mu_2)^{1/2}$ is multiplied with * = 0.2 for sources with a larger uncertainty in the second moment. The vertical shift for respective source is: AS 205 A = 0 AU, DR Tau = -3.4 AU, RU Lup = -7.0 AU, S CrA A = -7.2 AU. For VW Cha and VZ Cha the shifts are 5.5 and 3.7 AU after multiplication with 0.2.

show exactly the same profile. This means that the CO emission originates from within a few AU at many different angles around the sources.

2.5 Discussion

Three possibilities for the origin of broad-based single peaked profiles are discussed below: a Keplerian rotating disk, a disk wind or a funnel flow.

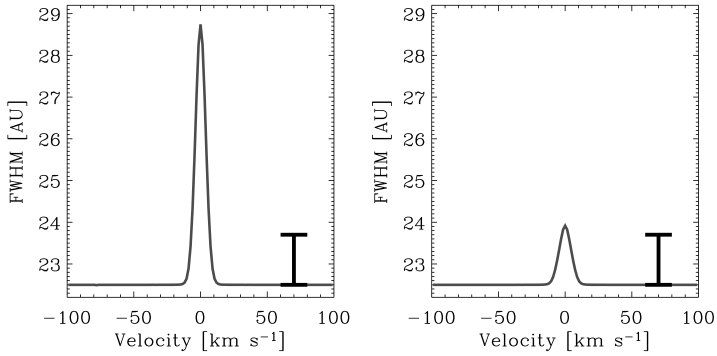

Figure 2.19 The second moment of the modeled spatial line profile for AS 205 (10 AU = 0.″08 at a distance of 125 pc). The model in the left plot includes extended emission out to 30 AU and $\Delta V_{\rm mod}$=3 km s^{-1}. The model in the right plot includes emission out to 10 AU and an increased $\Delta V_{\rm mod}$=7 km s^{-1} (see Fig. 2.5). Error bars represent the 3σ noise limit for AS 205 A in Fig. 2.18. Both models use the observed position angle of 115° which is 50° off from the position angle of 165° of the AS 205 A disk (Andrews et al. 2009).

2.5.1 Rotating disk

The results presented in §2.3.2 show that broad-based single peaked lines (category C) cannot be reproduced using a Keplerian model with a power-law temperature profile. Increasing the local line broadening parameter $\Delta V_{\rm mod}$ to ~8 km s^{-1} removes the double peak, but a larger local line broadening is not sufficient to give a good fit between the disk model and the data. As seen in § 2.3.2 a Keplerian disk model can fit the data by solving for a temperature structure. The best fits have a plausible temperature structure but require extended emission, possibly in combination with an increase in the local broadening parameter.

The results of § 2.4.3 show that the bulk of the emission comes from within a few AU which means that a Keplerian model with a non-standard temperature profile including extended emission out to 30 AU cannot explain the broad-based single peaked line profiles. Even the model with enhanced turbulence and emission out to 10 AU becomes marginal, as illustrated by the expected second moments in these non-standard cases (Fig. 2.19). The vertical error bars in Fig. 2.19 represent the 3σ noise limit in AU for AS 205 A. Similar results hold for most of the other sources, although the Keplerian models with a non-standard temperature profile including an enhanced turbulence cannot be fully ruled out for sources like VW Cha and VZ Cha, for which the limits on the spatial extent are larger.

Carr et al. (2004) invoked a larger local line broadening of 7–15 km s^{-1} in their disk models to obtain a better fit to CO v = 2 – 0 band head profiles observed

toward various young stellar objects. As discussed in their paper, such values are much larger than the sound speed of a few km s^{-1} in the inner disk, whereas models of turbulence in disks typically give velocities that are less than the sound speed (e.g., Klahr & Bodenheimer 2006). In addition, these turbulent values are much higher than those inferred from observations of gas in the outer disk (Qi et al. 2006, Hughes et al. 2009), although the turbulence in a warm surface layer near the star may differ from that in the outer regions. A more extended discussion of turbulence in inner disks is given in Carr et al. (2004). Even though we cannot fully exclude an increased level of turbulence for some of our sources, this is unlikely to be the sole explanation for the broad-based single peaked line profiles observed here.

In summary, the above discussion shows that a pure Keplerian disk model does not fit the data. However, the estimated rotational temperatures of 300 to 800 K for the broad centrally peaked sources are consistent with the temperature expected for the inner parts of a disk. The symmetry of the lines and the small radial velocity shift between the gas and the star (a maximum of ∼5 km s^{-1}) are additional indications that the emission may originate in a disk. Therefore, it is likely that at least part of the emission originates from the disk but some additional process must contribute to these line profiles as well.

2.5.2 Disk wind

Thermally launched winds

Strong outflows are excluded due to the small velocity shifts of the molecular gas relative to the central star. Thermally launched winds are driven by irradiation of either FUV (far-ultraviolet), EUV (extreme ultraviolet), or X-ray photons (Alexander 2008, Gorti & Hollenbach 2009, Ercolano & Owen subm.). Irradiation of the upper layers of the disk heats the gas to such high temperatures that the thermal energy exceeds the gravitational potential, leading to a flow off the disk surface. The launching radius is roughly given by $R_g = GM_\star/V_{\rm orb}^2$, where $V_{\rm orb}$ is the orbital speed of the gas. The wind retains the Keplerian rotational velocity of the launch radius.

If the disk is illuminated by EUV radiation, an HII region forms in the upper layer of the disk atmosphere. The ionized gas reaches a temperature of 10^4 K, which corresponds to V ∼10 km s^{-1}. For a 1 $M_\odot$ star, the launching radius is then $R_g \sim 5-10$ AU, and the wind is launched with a velocity of $\sim 5-10$ km s^{-1} (Alexander 2008). This small velocity shift is consistent with the small velocity shifts we see in the CO gas emission relative to the stellar radial velocity. However, an EUV-driven wind consists mostly of ionized gas, so that CO may be photodissociated. Detailed models of the CO chemistry are needed to test whether enough CO can survive in such a wind to produce the observed CO line profiles.

In the X-ray and FUV photoevaporation models of Gorti & Hollenbach (2009),

the evaporating gas is cooler than the EUV-irradiated gas. The expected launching radii of 10–50 AU for X-ray photoevaporation and >50 AU for FUV photoevaporation are inconsistent with the lack of spatially-extended emission in our CO spectra. However, in models of photoevaporation by soft X-ray emission by Ercolano & Owen (subm.), the launching radius is closer to the star. Ercolano & Owen (subm.) calculate profiles for atomic and ionized species within this model and predict symmetric, broad-based, single-peaked line profiles with small blueshifts of 0–5 km s^{-1}.

As for the EUV models, a detailed CO chemistry needs to be coupled with the wind model to test this scenario, but the fact that the wind is mostly neutral will help in maintaining some CO in the flow.

In summary, EUV and soft-X-ray photoevaporation of the disk might produce some CO emission at low velocities. More detailed studies of the CO chemistry and velocity fields in the thermally-launched wind are needed to determine where CO can survive in the wind and the resulting emission line profile.

Magnetically launched winds

Magnetic fields of Classical T Tauri stars exert torques that are thought to be strong enough to launch powerful winds. Edwards et al. (2006) describe two types of winds that are seen in absorption in the He 1 λ10830 line, one with velocities of around 250 km s^{-1} and another with lower speeds up to 50 km s^{-1}. These velocity shifts are also commonly observed in optical forbidden lines, such as [O I] 6300 Å. The high velocities are not consistent with the velocities seen in the broad-based single peaked CO emission, making this scenario highly unlikely.

2.5.3 Funnel flow

Accretion from the disk onto the star is thought to occur in a funnel flow along strong dipolar field lines (e.g., Hartmann et al. 1994, Bouvier et al. 2007, Yang et al. 2007, Gregory et al. 2008). Najita et al. (2003) rule out the possibility that the funnel flow could produce some CO emission because the temperatures in the funnel flow are expected to be $\sim 3000 - 6000$ K (Martin 1997), higher than the measured temperatures of the CO-emitting gas. Models of observed hydrogen emission line profiles are consistent with these temperatures (Muzerolle et al. 2001, Kurosawa et al. 2006). However, Bary et al. (2008) suggest that the relative hydrogen emission line fluxes may also be consistent with cooler temperatures of $\sim 1000 - 1500$ K, and cooler temperatures may be present where the funnel flow connects with the disk. Najita et al. (2003) show that a modeled CO emission line profile from a funnel flow would have a double peaked line profile with no velocity shift (see Fig. 10b in their paper), which disagrees with the presence of the narrow emission peak seen in the line profiles discussed here. Thus, funnel flows are also not likely to be the origin of the observed emission.

2.6 Conclusions

Using CRIRES spectroscopy of CO (Δv = 1) ro-vibrational emission lines around 4.7 μm from a sample of 50 T Tauri stars, we find that the line profiles can be divided into three basic categories: A) narrow single peaked profiles, B) double peaked profiles and C) single peaked profiles with a narrow peak ($\sim 10-20\,\mathrm{km\,s^{-1}}$), but broad wings, sometimes extending out to $100\,\mathrm{km\,s^{-1}}$. The broad-based single peaked line profiles are rather common, since they were detected in 8 sources in a sample of about 50 T Tauri stars. These 8 sources have preferentially high accretion rates, show detections of higher vibrational emission lines (up to $v = 4$) and have CO lines with unusually-high line-to-continuum ratios relative to all other sources within our sample. For at least one of the disks (S CrA B), the narrow component decreases faster for higher J lines than the broad component, implying that the narrow component is colder. Generally, however, the two component fits give similar temperatures and central velocities.

The broad-based single peaked emission originates within a few AU of the star with gas temperatures of ~300 – 800 K. The line profiles are symmetric and the gas radial velocity is close to the stellar radial velocity. These characteristics point toward an origin in a disk. However, unlike the CO profiles from other objects that are double-peaked or have only one narrow peak, the broad-based single peaked line profiles could not be well fit using a Keplerian model with a power-law temperature profile. The fits are improved if a large turbulent width of $\sim$ 8 km s^{-1} is invoked, but the overall profile fit is still poor. Models with an unusual temperature distribution, perhaps with enhanced turbulence, provide a much better fit to the line profiles but require emission out to larger distances than observed. Thus, the hypothesis that this emission originates in a pure Keplerian disk needs to be questioned and an additional physical component needs to be considered.

Several other scenarios are also ruled out. FUV radiation-driven winds have a launching radius of > 50 AU that is inconsistent with the lack of spatially-extended emission in our data. Magneto-centrifrugal winds are observed to have blueshifts of 50 – 250 km s^{-1}, which are inconsistent with the lack of a significant velocity shift in the symmetric CO emission lines. A funnel flow is also unlikely because emission near the inner rim of the disk should have a double-peaked line profile, and because the temperatures in the funnel flow are expected to be higher than the calculated CO rotational temperatures.

The most plausible explanation for the broad-based single-peaked line profiles is therefore some combination of emission from the warm surface layers of the inner disk, contributing to the broad component through Keplerian rotation, and a disk wind, responsible for the narrow component. A thermally launched disk wind, perhaps driven by EUV radiation or soft X-rays will have a small velocity shift of ΔV of 0-10 km s^{-1}, which is marginally consistent with the maximum detected velocity shift of ΔV ~5 km s^{-1}.

More information, including independent estimates of inclination angles, detailed models of CO chemistry and line profiles that originates in disk winds and the inner regions of disks, and spectro-astrometry of emission from these sources, is needed to distinguish the contributions from a disk (perhaps with enhanced turbulence) and a disk wind. These line profiles will be further discussed by Pontoppidan, Blake & Smette (subm.) using a combined disk and slow molecular disk wind model to analyze the spectro-astrometric data of these sources.

Acknowledgements

JEB is supported by grant 614.000.605 from Netherlands Organization of Scientific Research (NWO). EvD acknowledges support from a NWO Spinoza Grant and from Netherlands Research School for Astronomy (NOVA). JEB is grateful for the hospitality during long term visits at the Max Planck Institute for Extraterrestrial Physics in Garching and Division of Geology and Planetary Science at California Institute of Technology in Pasadena. The authors would like to acknowledge valuable discussions with R. Alexander, B. Ercolano, C. Salyk, J. Muzerolle, A. Johansen, A. Smette, U. Käufl and W. Dent.

III

First detection of near-infrared line emission from organics in young circumstellar disks[1]

We present an analysis of high-resolution spectroscopy of several bright T Tauri stars using the VLT/CRIRES and Keck/NIRSPEC spectrographs, revealing the first detections of emission from HCN and C_2H_2 in circumstellar disks at near-infrared wavelengths. Using advanced data reduction techniques we achieve a dynamic range with respect to the disk continuum of $\sim$ 500 at 3 μm, revealing multiple emission features of H_2O, OH, HCN, and C_2H_2. We also present stringent upper limits for two other molecules thought to be abundant in the inner disk, CH_4 and NH_3. Line profiles for the different detected molecules are broad but centrally peaked in most cases, even for disks with previously determined inclinations of greater than 20°, suggesting that the emission has both a Keplerian and non-Keplerian component as observed previously for CO emission. We apply two different modeling strategies to constrain the molecular abundances and temperatures: we use a simplified single-temperature LTE slab model with a Gaussian line profile to make line identifications and determine a best-fit temperature and initial abundance ratios, and we compare these values with constraints derived from a detailed disk radiative transfer model assuming LTE excitation but utilizing a realistic temperature and density structure. Abundance ratios from both sets of models are consistent with each other and consistent with expected values from theoretical chemical models, and analysis of the line shapes suggests the molecular

[1]Based on: A.M. Mandell, J.E. Bast, E.F. van Dishoeck, G.A. Blake, C. Salyk, M.J. Mumma and G. Villanueva, 2012, Ap.J., 747, 92

emission originates from within a narrow region in the inner disk (R < 1 AU). [1]

[1] Based partially on observations collected at the European Southern Observatory Very Large Telescope under program ID 179.C-0151, program ID 283.C-5016, and program ID 082.C-0432 (PI: Pontoppidan).

3.1 Introduction

The chemical and thermal distribution of the warm gas in the inner regions of protoplanetary disks provides important diagnostics related to the composition of the material that formed into planets around nearby stars. With the recent discovery of surprisingly large numbers of super-Earths (planets with masses of $1-10$ M_{Earth}) within a few AU of their parent stars, significant questions have been raised concerning their origin and composition (Borucki et al. 2011). Spectroscopy of the atmospheres of a few such super-Earth and mini-Neptune planets show large variations in composition from object to object (Madhusudhan & Seager 2011, Désert et al. 2011), and it is clearly important to constrain the chemistry of the gas in the inner regions of protoplanetary disks in order to better understand the origin of the atmospheres and interiors of these planets.

With improved infrared instrumentation on ground- and space-based telescopes, various molecules can now be observed in the warm irradiated surface layers of disks, allowing us to determine their chemistry and dynamics. CO rovibrational emission at $4.7\,\mu$m has been extensively surveyed in both Herbig Ae (HAe) and T Tauri stars (Brittain et al. 2003, Najita et al. 2003, Blake & Boogert 2004, Pontoppidan et al. 2008, Salyk et al. 2009, Pontoppidan et al. 2011, Bast et al. 2011), H_2O emission has been detected in both the overtone (Carr et al. 2004) and fundamental bands (Salyk et al. 2008), and there have been early detections of additional tracers such as warm H_2 (Bitner et al. 2007) and OH (Mandell et al. 2008, Fedele et al. 2011). Just in the last few years, there have been surprising detections of absorption by C_2H_2, HCN and CO_2 in systems with unique viewing geometries (Lahuis et al. 2006, Gibb et al. 2007), and high S/N data from Spitzer are now revealing an extraordinarily rich mid-IR spectrum in emission containing lines of water, OH and organics (Carr & Najita 2008, 2011, Pascucci et al. 2009, Pontoppidan et al. 2010, Salyk et al. 2011). Overall, we are moving toward a comprehensive picture of the disk chemistry and temperature structure in the region of the disk in which planets form; these results will aid in understanding processes such as planetary migration, disk turbulence and the accretion of volatiles. However, to accurately constrain the physical structure and chemical balance among different molecular species in different regions of the disk we must analyze a full suite of molecular tracers, with transitions excited at both high and low temperatures, using instruments with sufficient resolving power to constrain different line shapes indicative of different Keplerian velocities (i.e., different source regions).

In this paper we present high-resolution ($R = 25,000-95,000$) L-band ($3-4\,\mu$m) observations of three bright T Tauri stars using the CRIRES instrument on the Very Large Telescope and the NIRSPEC instrument on the Keck II telescope, with the goal of further characterizing molecular emission from gas tracers that have been detected with the IRS instrument on Spitzer (primarily HCN) and to search for new species not covered by the Spitzer bandpass, specifically CH_4. The latter two molecules are observed to be significant components of interstellar ices (Öberg

et al. 2008, Bottinelli et al. 2010) and of comets (Mumma & Charnley 2011), with typical abundances of a few percent with respect to H_2O. If incorporated unaltered into icy planetesimals in the cold outer regions and subsequently transported inward across the snow line, they become part of the gas in the planet-forming zones. Observations of CH_4 are of particular interest because of the recent controversies on the CH_4/CO abundance ratios in exoplanetary atmospheres (Madhusudhan et al. 2011, Madhusudhan & Seager 2011).

The search for new molecules is best done toward sources which show high fluxes of common molecules and high line-to-continuum ratios. The three stars observed for this study have all been identified through their unusually bright CO emission (Bast et al. 2011), and two of them (AS 205 A and DR Tau) have been shown to have bright water emission at 3.0 μm (Salyk et al. 2008). AS 205 A is a K5 star within a triple system in the constellation of Ophiuchus. With an age of 0.5 Myr and a disk inner radius of 0.07 to 0.14 AU, the system is the archetype of a young gas-rich accreting primordial disk (Andrews et al. 2009, Eisner et al. 2005). DR Tau is a K7 star, while RU Lup is a G5 star; these disks are less bright at NIR wavelengths than AS 205 A but similar in their rich molecular emission characteristics. We present a preliminary analysis of the detected molecular disk tracers using several different molecular emission models, discuss our results in the context of recent observations of mid-IR emission from the same objects as well as theoretical models of disk chemistry, and describe future work required to improve our constraints on the abundance and distribution of these molecular gas tracers of the warm inner disk.

3.2 Observations and data reduction

Spectra were acquired over several observing epochs using the CRIRES instrument on the VLT ($\lambda/\Delta\lambda \approx 96{,}000$) as part of our large program to study primordial circumstellar disks (Pontoppidan et al. 2011b), and additional data were acquired with the NIRSPEC instrument on Keck ($\lambda/\Delta\lambda \approx 25{,}000$). Comparison stars were also observed as close in time and airmass to the science targets as possible; a full list of targets is listed in Table 3.1. Both telescopes were nodded in an ABBA sequence with a throw of 10 – 12 arcseconds between nods, with a 60-second integration time per image (or combination of co-adds). The CRIRES observations for DR Tau and RU Lup were taken using two different wavelength settings in order to cover the gaps between the instrument detectors, while only a single setting was used for AS 205 A; a single echelle and cross-disperser setting was used for the NIRSPEC observations of DR Tau. In total, we analysed 48 CRIRES spectra and 28 NIRSPEC spectra of DR Tau, 32 CRIRES spectra of RU Lup, and 36 CRIRES spectra of AS 205 A.

Table 3.1 Summary of Observations

Star	Dates	Instrument	Wavelength Range (μm)	t_{int} (min)	Standard	Molecules
AS 205 A	UT July 23 2009	VLT/CRIRES	2.995 – 3.058	36	BS6378	HCN, C_2H_2, NH_3, H_2O, OH
DR Tau	UT October 30 2007	Keck/NIRSPEC	2.947 – 2.987	28	HR1620	HCN, H_2O, OH
	UT December 31 2008	VLT/CRIRES	3.333 – 3.414	48	HR2421	CH_4, OH
RU Lup	UT August 5 2009	VLT/CRIRES	2.995 – 3.071	32	BS5812	HCN, C_2H_2, NH_3, H_2O, OH

We utilized custom data reduction algorithms, previously used to detect new molecular emission features from warm gas in circumstellar disks (Mandell et al. 2008, Mandell et al. 2011) to extract and process spectra for each echelle order in each ABBA set. We reduced the initial 2D spectral-spatial images to 1D spectra after first correcting for the slope of the beam due to cross-dispersion and subtracting A- and B-beam images to remove the contribution from telluric radiance. We identified bad pixels and cosmic ray hits in each raw pixel column by comparing the beam profile to an average beam profile for nearby columns, allowing us to identify and replace single-pixel events without removing any enhancements due to emission or absorption features.

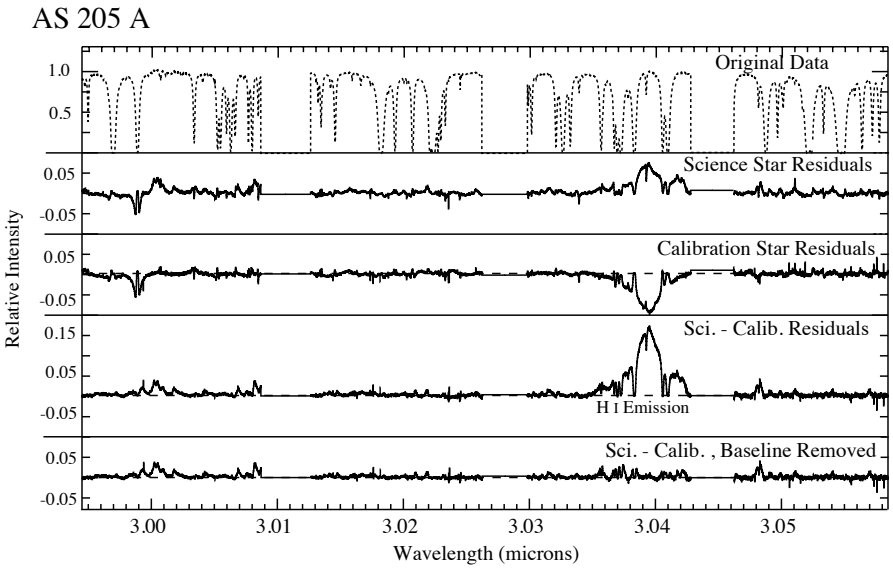

Figure 3.1 Data for AS 205 A, with the original data plotted in the first panel and subsequent residuals plotted below. The Science and Calibration Star Residuals are produced by removing a best-fit atmospheric model for each star separately; the two residuals are then differenced to produce the Science - Calibration Residuals. A segmented baseline composed of several polynomial fits is then used to remove broad features such as the H I emission line.

We corrected for changing airmass and telluric atmospheric conditions by fitting the data with a terrestrial spectral transmittance model synthesized with the LBLRTM atmospheric code (Clough et al. 2005) based on line parameters from the HITRAN 2008 molecular database with updates from 2009 (Rothman et al. 2009). The telluric models were optimized to fit the observational data by varying the abundances of the primary atmospheric constituents (H_2O, CO_2, CH_4, O_3, and

N_2O), with the resolving power of the model set by the width of the narrowest telluric features. Atmospheric models were fitted for wavelength sub-sections of each AB set, and the telluric model was subtracted from the stellar data to produce a first set of residuals. We performed the same telluric removal routine on the comparison star, and the post-telluric residuals of the science and comparison stars were then differenced to remove remnant fringes and other instrumental artifacts, as well as minor errors in the telluric model such as improper pressure broadening and isotopic ratios. The residuals for all sections were then combined, and the complete spectrum was then fit with a new segmented continuum model to remove obvious broad emission features, most notably the H I emission line at 3.04 μm. The new continuum baseline matched a polynomial fit to individual segments of the spectrum whose length was defined interactively (but not less than 100 pixels), allowing us to fit sections of the spectrum with a complex morphology. The different steps of the reduction process are illustrated in Figure 3.1.

The reduction process yields spectra with S/N on the stellar continuum corresponding to an rms noise only slightly larger (by 20%) than that expected from the photon statistics, reaching ~ 500 for AS 205 A. These are the deepest disk spectra obtained in this wavelength range with CRIRES to date. Data with remaining bad pixels and other artifacts (such as several unidentified stellar features in the comparison star for AS 205 A) were removed; the regions were 5 pixels or less, and did not affect the processing or analysis of nearby pixels. Flux calibration was performed by normalizing the observed continuum flux to the predicted flux based on the K-band stellar magnitude (Cutri et al. 2003), which was then converted to L-band magnitudes using colors from the literature (Glass & Penston 1974, Hartigan et al. 1990, Appenzeller et al. 1983). The flux was further adjusted for a wavelength-specific flux assuming a continuum blackbody temperature of 1500 K, which is the standard temperature for the veiling continuum of T Tauri stars; however, since the stellar magnitudes were converted to L-band magnitudes using observed colors, this correction was relatively minor.

3.3 Line identification and LTE slab modeling

The final spectral residuals for each star revealing disk emission are shown in Figures 3.2 - 3.5. The data for AS 205 A and RU Lup cover the spectral region between 2.995 μm and 3.071 μm, allowing us to search for multiple transitions of HCN, H_2O, OH, and C_2H_2, and emission from the ν_1 band of NH_3. The NIRSPEC data for DR Tau cover the spectral region between 2.947 μm and 2.987 μm (spanning transitions of HCN, H_2O and OH), while the CRIRES data for DR Tau cover the region between 3.333 μm and 3.414 μm, allowing us to search for emission from OH and the P branch of the $2\nu_2$ band of CH_4 (Table 3.1).

Initial identifications of emission features in the residual spectra were assigned using data from the HITRAN 2008 molecular database with updates from 2009 (Rothman et al. 2009). We conclusively detect emission from H_2O, OH, and HCN

Table 3.2 Line Intensities for Selected Molecular Features

Source	Molecule	$\lambda_{rest}(\mu m)$	Transition[a]	Intensity (W/cm^2)
AS 205 A	HCN	3.00155	$(\nu_1+\nu_2+\nu_3)$-$(\nu_2+\nu_3)$, R13 e	2.1×10^{-22}
		3.00158	ν_1, R6	4.7×10^{-22}
	H_2O	3.02066	$(100)6_{51}$ - $(000)7_{62}$	1.4×10^{-22}
		3.02067	$(100)6_{51}$ - $(000)7_{61}$	4.3×10^{-22}
	OH	2.99995	$X^2\Pi_{1/2}$ (1-0), P5.5 f	1.2×10^{-21}
		3.00022	$X^2\Pi_{1/2}$ (1-0), P5.5 e	1.2×10^{-21}
	C_2H_2	2.99800	$\nu_2+\nu_4+\nu_5$, R23e	1.4×10^{-22}
		2.99801	ν_3, R17 e	1.4×10^{-22}
RU Lup	HCN	3.00155	$(\nu_1+\nu_2+\nu_3)$-$(\nu_2+\nu_3)$, R13 e	1.5×10^{-22}
		3.00158	ν_1, R6	3.4×10^{-22}
	H_2O	3.02066	$(100)6_{51}$ - $(000)7_{62}$	6.7×10^{-23}
		3.02067	$(100)6_{51}$ - $(000)7_{61}$	2.1×10^{-22}
	OH	2.99995	$X^2\Pi_{1/2}$ (1-0), P5.5 f	2.5×10^{-21}
		3.00022	$X^2\Pi_{1/2}$ (1-0), P5.5 e	2.5×10^{-21}
	C_2H_2	2.99800	$\nu_2+\nu_4+\nu_5$, R23 e	1.5×10^{-22}
		2.99801	ν_3, R17 e	1.3×10^{-22}
DR Tau	HCN	2.97525	ν_1, R17	1.4×10^{-22}
		2.97528	$(\nu_1+2\nu_2)$-$(2\nu_2)$, R 33	4.1×10^{-24}
	H_2O	2.95642	$(001)12_{66}$ - $(000)13_{67}$	1.4×10^{-22}
	OH	2.96043	$X^2\Pi_{1/2}$ (1-0), P4.5 e	3.1×10^{-22}
		2.96026	$X^2\Pi_{1/2}$ (1-0), P4.5 f	3.1×10^{-22}
	CH_4	3.38053	ν_3, P6 (F2-F1)	$< 6.0\times10^{-23}$
		3.38040	ν_3, P6 (F1-F2)	$< 6.0\times10^{-23}$

[a]Multiple transitions are listed if a single molecular feature is an unresolved blend or a doublet

in the spectra of all three stars, with multiple strong features of each molecule detected. We also detect several low-amplitude features due to C_2H_2 in AS 205 A; there is one clean feature at $3.0137\,\mu$m and several blended features ($2.9981\,\mu$m, $3.0021\,\mu$m, $3.0177\,\mu$m) that require C_2H_2 for a decent fit. Part of the blend at $2.9981\,\mu$m in the RU Lup spectrum may also be due to C_2H_2, but no other features are detectable. We can place an upper limit on CH_4 emission from DR Tau based on the CRIRES data; even though a weak feature is visible at $3.381\,\mu$m, no corresponding lines are present at $3.393\,\mu$m and $3.405\,\mu$m that could be ascribed convincingly to CH_4. We also place upper limits on the presence of NH_3 emission from AS 205 A and RU Lup. The contribution of NH_3 at $2.9995\,\mu$m and $3.0015\,\mu$m improves the model fit, but there are several other locations where the fit is degraded (see Figure 3.6). A list of selected lines for each molecule and the derived intensities for each star are listed in Table 3.2.

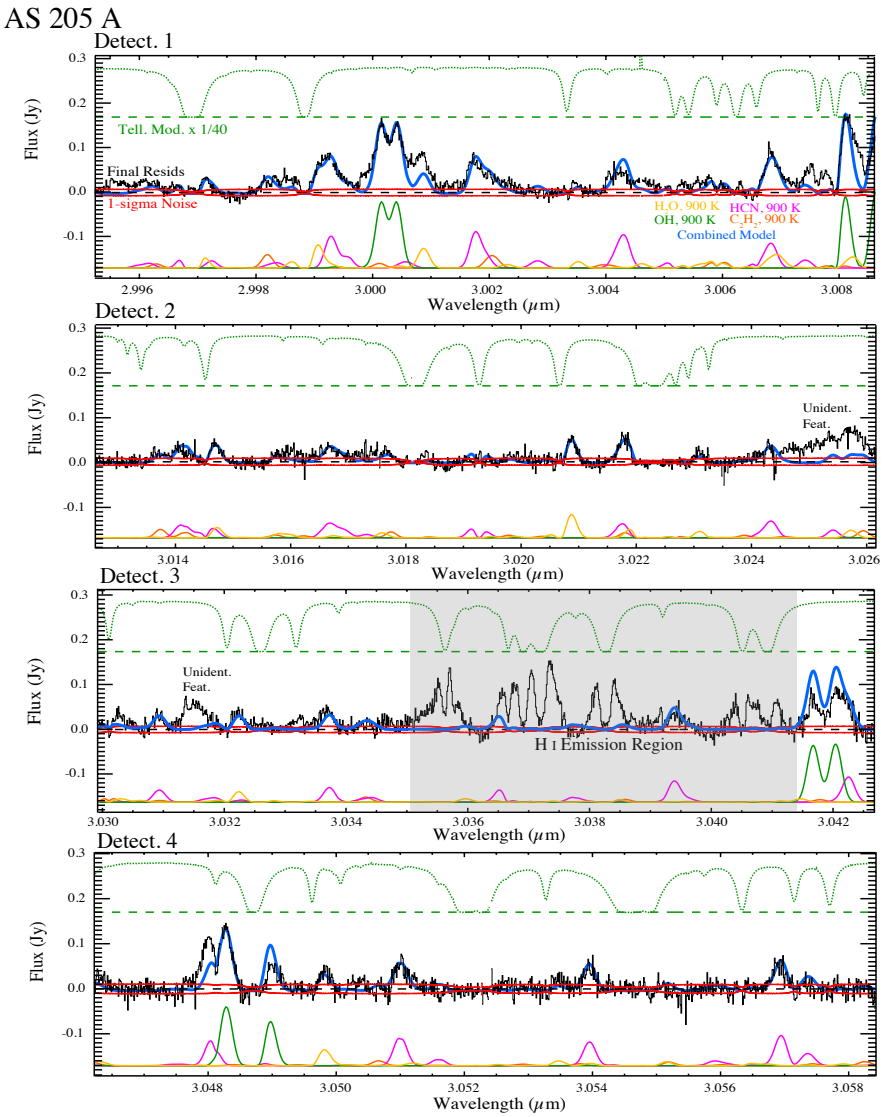

Figure 3.2 VLT-CRIRES data for AS 205 A overplotted with model spectra of LTE molecular emission from a simple slab model convolved with a Gaussian line shape. Emission from H_2O, OH, and HCN is clearly detected; emission features from C_2H_2 are also detected but the lines are weaker and blending with other features makes the detection less secure.

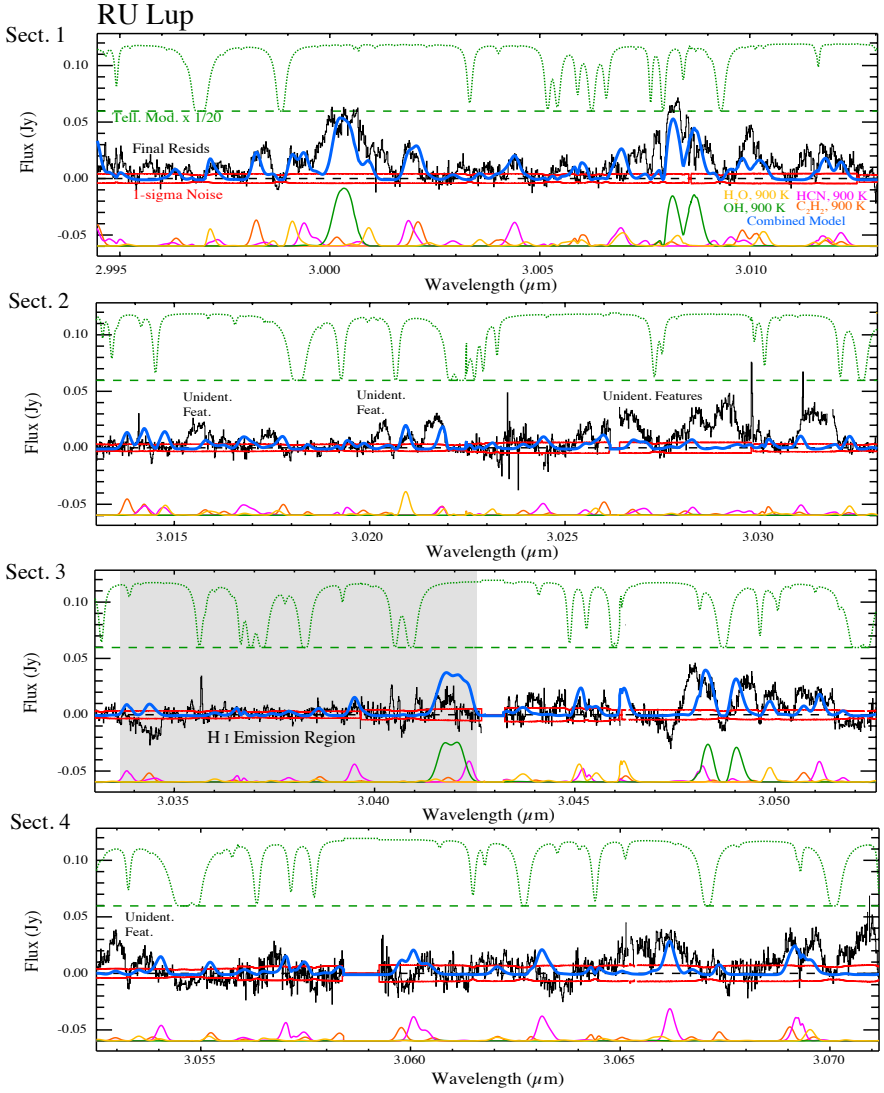

Figure 3.3 VLT-CRIRES data for RU Lup overplotted with model spectra from an LTE slab model. Emission from H_2O, OH, and HCN is present, but emission features from C_2H_2 are less secure than for AS 205 A.

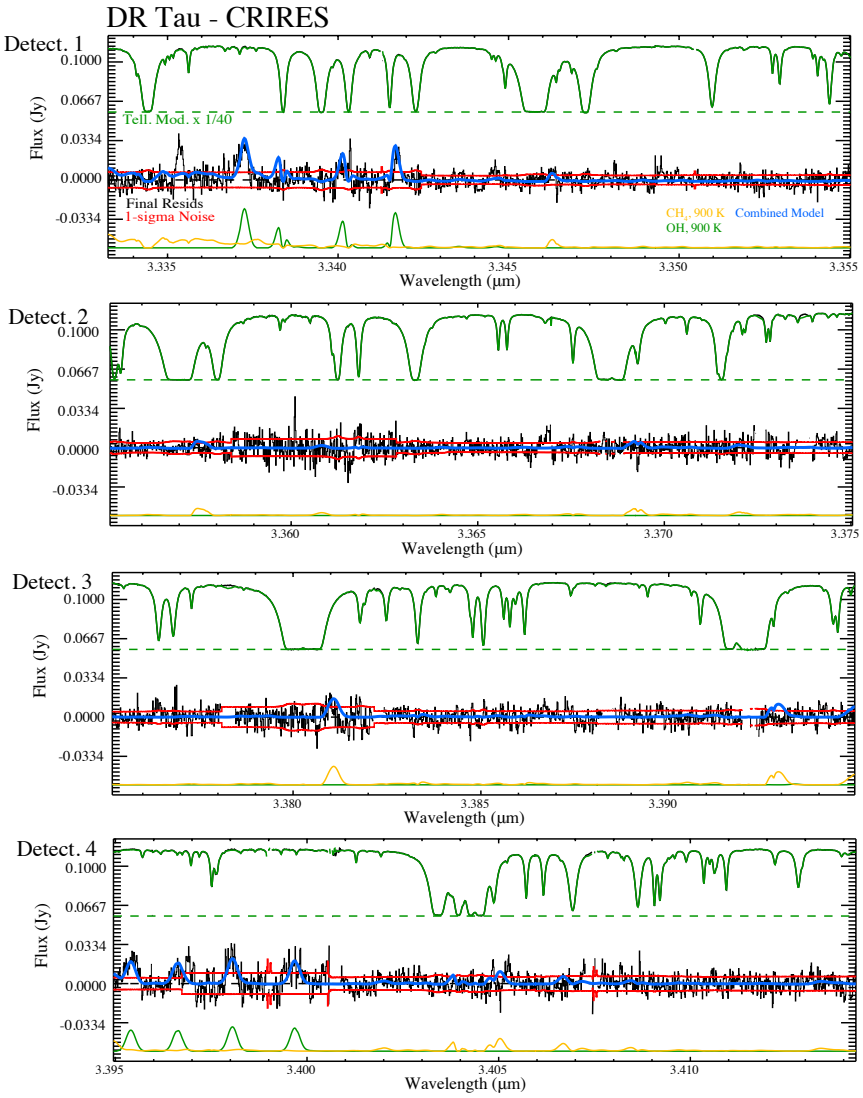

Figure 3.4 VLT-CRIRES data for DR Tau overplotted with model spectra for OH and CH_4 from an LTE slab model. Several high-J OH lines are clearly detected, but the evidence for CH_4 is not conclusive. There is a possible features at 3.346 and 3.381 μm, but other features at 3.358 and 3.393 μm are not present. We therefore only list an upper limit for the abundance of CH_4.

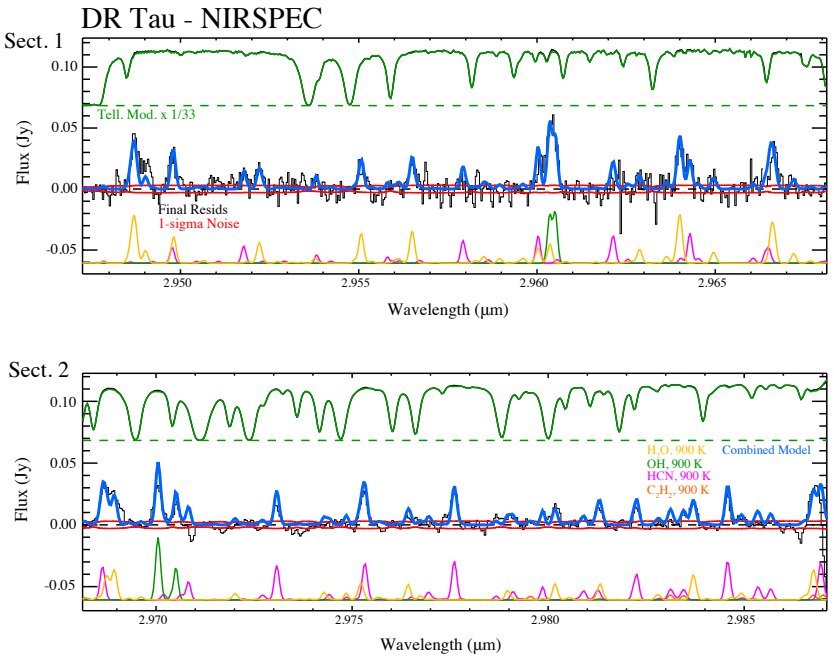

Figure 3.5 Keck-NIRSPEC Data for DR Tau overplotted with model spectra from an LTE slab model. Emission from H_2O, OH, and HCN is present, but emission features from C_2H_2 are too weak to be detected.

Table 3.3 Molecular ratios, relative to H_2O, estimated by using the slab model and constant abundance disk model (Model 1), respectively. Abundances for DR Tau (except for CH_4) were calculated from data obtained with the NIRSPEC instrument on Keck; all other abundances were determined from data obtained with the CRIRES instrument on the VLT.

Model	Source	HCN/H_2O	OH/H_2O	CH_4/H_2O	NH_3/H_2O	C_2H_2/H_2O	CO/H_2O	FWHM (km s^{-1})
Slab[a]	AS 205 A	0.06± 0.01	0.25± 0.03	-	< 0.16	0.05± 0.01	11.6	22.5
	DR Tau	0.05± 0.01	0.16± 0.02	< 0.07	-	< 0.03	29.0	10.8
	RU Lup	0.05± 0.02	0.3–0.6[b]	-	< 0.2	0.05± 0.02	18.3	16.2
Disk	AS 205	0.07	0.2	-	-	-	6.5	
	DR Tau	0.07	0.13	< 0.09	-	-	2.9	
	RU Lup	0.08	1.5	-	-	-	3.3	

[a]Slab model abundances were calculated with a common temperature of 900 K, except for CO which was best fit with a temperature of 600 K

[b]The OH abundance ratio from the slab model for RU Lup is given as a range, based on either a Gaussian or Keplerian fit.

Initial abundance ratios for the molecules sampled in each spectrum were determined using a simple model of molecular gas in local thermal equilibrium (LTE), which approximates an optically thin medium where the line intensities are defined purely by the temperature of the emitting gas (i.e., a Boltzmann distribution) and the relative probability of each transition; this methodology is commonly known as a "slab" model. We calculated the best-fit common temperature for the detected molecular features by varying the characteristic temperature between 300 K and 2000 K with a step of 50 K; we chose to use a common temperature in these fits due to the extensive blending of features and the narrow wavelength range being investigated. A temperature of 900 K was found to fit the relative line strengths for all species to within the uncertainties related to the complexity of the spectrum. Abundances for each molecule were then varied to fit the equivalent widths of the strongest lines. The ratio of the abundance of each molecule relative to H_2O is listed in Table 3.3. It can be seen from Figures 3.2 - 3.5 that the basic LTE models do quite well in modeling the line positions and intensities, and very few features in the observed spectrum were left unidentified. Several residual features close to 3.035 μm in both AS 205 A and RU Lup are due to the difficulty in fitting the broad H I emission feature seen in Figure 3.1. The feature at 3.0315 μm in the spectrum of AS 205 A has no identification, and the features between 3.025 and 3.032 micron in both RU Lup and AS 205 A are also unidentified.

A list of molecular ratios and upper limits referenced to H_2O are listed in Table 3.3. We choose H_2O as the reference for the abundances because the features for all three molecules occur in the same wavelength region and the similar line shapes suggest they trace approximately the same region of the disk. We also include the ratio of CO to H_2O, calculated by fitting our LTE slab model to previously reduced CO spectra from CRIRES reported in Bast et al. (2011). Our slab modeling is very similar to the methodology used in Bast et al. (2011), and we refer the reader to that paper for figures and additional details. We derived our CO abundance by fitting lines of ^{13}CO and then multiplied the value by 65 (Langer & Penzias 1990) to derive the overall CO abundance; the ^{13}CO were explicitly shown to be optically thin for DR Tau Bast et al. (2011), and we maintain the same assumption for AS 205 A and RU Lup (the CO data for these sources does not allow for confirmation of the optical depth, as discussed in Bast et al. (2011)). We use a common rotational temperature of 600 K (close to the values found for AS 205 A and DR Tau by) for consistency with the common temperature derived for the other molecules. The difference in the best-fit temperatures for CO compared with the other molecules is robust and may be related to differences in emitting location (see §3.4.1), but a detailed analysis of the molecular distributions is reserved for future work.

Previously determined inclinations for these objects from spectroastrometry range from 10° to 35° (Pontoppidan et al. 2011; see Table 3.4), and the spectra therefore should show Keplerian line shapes if the outer radius of the emitting gas is restricted to the inner disk. However, the line shapes for the newly detected molecules can be approximated quite well with a Gaussian profile, similar to the cores of the CO lines fit by Bast et al. (2011). Figure 3.7 shows single lines of

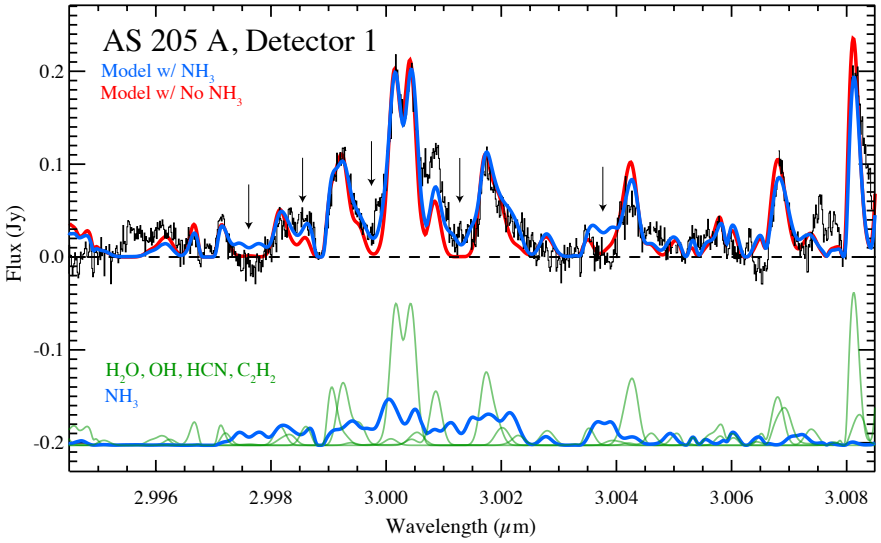

Figure 3.6 VLT-CRIRES data for AS 205 A, with best-fit models plotted both with and without the contribution from NH_3. The arrows identify locations where the models diverge, but the evidence is inconclusive as to whether emission from NH_3 is detected; we therefore only quote an upper limit.

HCN, H_2O and CO for AS 205 A normalized and plotted on top of each other. The HCN and H_2O lines are noisier due to their lower S/N but it can clearly be seen that the central regions of the three lines all have a similar single peaked line shape (we cannot stack features for improved S/N due to the extensive blending of features). Assuming a Gaussian line shape including thermal broadening and convolved with the instrumental profile, we find best-fit FWHM values between 10 km s^{-1} and 22.5 km s^{-1} for the strongest H_2O and HCN transitions in the three stars (see Table 3.3). The one exception to the single-peaked profile is the OH emission from RU Lup, whose features are clearly not fit well by a Gaussian model. Figure 3.8 demonstrates that a simple disk profile using an inner and outer radius ($0.05 - 0.5$ AU) and an exponential drop-off in flux ($I \propto R^{-3}$) provides a much better fit than the best-fit Gaussian profile for this OH line, suggesting a distribution limited to the very inner regions of the disk. This corresponds well with the limit on the outer radius of 0.5 AU for OH and H_2O emission from AS

Table 3.4 Parameters used in each specific fiducial disk model.

Parameters[a]	Source		
	AS 205 A	DR Tau	RU Lup
$M_\star$ [$M_\odot$]	1.0[1]	0.8[2]	0.7[7]
$R_\star$ [$R_\odot$]	3.7[1]	2.1[2]	1.3[8]
T_{eff} [K]	4250[1]	4060[2]	4060[8]
M_{disk} [$M_\odot$]	0.029[1]	0.01[3]	0.03[9]
R_{out} [AU]	200[1]	100[3]	100[4]
R_i [AU]	0.14[1]	0.05[4]	0.2[11]
h_p/R	0.21[1]	0.15[8]	0.20[8]
α	0.11[1]	0.07[8]	0.09[8]
β	-0.9[1]	-0.5[3]	-0.9[10]
i [°]	20[7]	9[7]	35[7]

[a]References: (1) Andrews et al. (2009) ; (2) Ricci et al. (2010); (3) Andrews & Williams (2007); (4) Schegerer et al. (2009); (5) Robitaille et al. (2007); (6) Isella et al. (2009), (7) Pontoppidan et al. (2011), (8) Herczeg & Hillenbrand (2008), (9) Lommen et al. (2007), (10) set to be the same as for AS 205 A however this parameter do not impact strongly on the line intensities, (11) Increased from 0.1 AU as found by Schegerer et al. (2009) in order to fit the narrow line shapes with the published inclination

205 A determined by Pontoppidan et al. (2011), and a similar result was found by Fedele et al. (2011) for the OH lines from at least one HAe star.

As mentioned above, in the context of a Keplerian model the lack of a resolved double peak within the central core of most of the emission features in the CRIRES data would suggest significant emission from the outer disk (especially for disks with higher inclination such as RU Lup), and with the high spatial resolution of the VLT this emission would be detectable as an enhanced PSF size within the molecular line core compared with the continuum region outside the line. The line-to-continuum ratio for the H_2O and HCN features in our own spectrum is too low to allow a measurement of any deviations in the spatial profile due to extended emission, but both Bast et al. (2011) and Pontoppidan et al. (2011) demonstrate that the measurements of the CO lines show no such emission. These authors also show that the CO line shapes can actually be optimally modeled using a combination of a broad, low-amplitude (double-peaked) profile and a stronger single-peaked line core, suggesting a two-component profile. Recent spectroastrometric modeling of the CO features suggests that emission from a slow disk wind may account for the sub-Keplerian velocity profile of the central core of the line Pontoppidan et al. (2011). The disk wind explanation for the bulk of our emission is further supported by the fact that the emission features in each star appear to be shifted from the predicted position based on the stellar radial velocity by $\sim$ 5 km s^{-1} (red-shifted for AS 205 A, blue-shifted for RU Lup), matching the shifts calculated for the narrow component of the CO profile in Bast et al. (2011); however, line blending and uncertainties in line positions make the determination of velocity shifts difficult to confirm. Since the line profile will be determined by a combination of emission from both the disk and the wind, the similarity in line

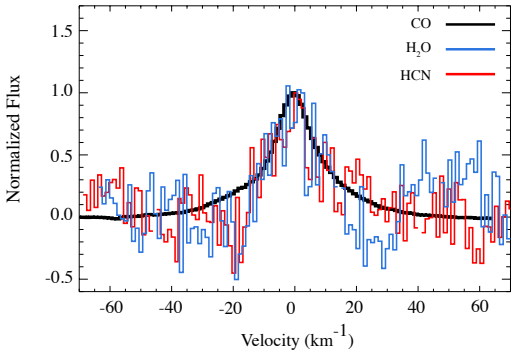

Figure 3.7 Ro-vibrational emission lines from three different molecules observed in AS 205 A. The different J-transitions are: P(8) (CO), P(11) (HCN) and $(100)8_{45}$ - $(000)9_{54}$ (H_2O). All three lines show the same shape to within measurement uncertainties, suggesting a common emitting distribution in the disk and/or the disk wind.

profiles of all three molecules suggests that the abundance ratios do not vary much between the disk and wind. We discuss the quantitative application of the disk wind model to our data in more detail in the following sections.

The HCN/H_2O, OH/H_2O and CO/H_2O ratios derived here are all approximately an order of magnitude higher than the values derived by Salyk et al. (2011; hereafter S11) for the same sources using mid-infrared spectra taken with IRS/Spitzer. Our upper limits for NH_3 with respect to water are also at least an order of magnitude higher than the Spitzer-based upper limits of ≤ 0.01 reported by S11. However, the usefulness of a direct comparison between the values derived by both slab model-based analyses is limited by several factors. First, it is important to note that emission from molecular gas originates from a range of radial and vertical positions in the disk, and that a different portion of this range is probed by each wavelength regime. Thus, there is no requirement that the molecular abundance ratios remain the same at each wavelength observed, and we could, in theory, observe radial variation in disk chemistry. Nevertheless, one obvious limitation of both studies may resolve much of the discrepancy - the assumption of a common emitting location for all molecules. This may especially affect the mid-IR abundance ratios, in which the pure-rotational water lines appear to probe lower temperatures ($300 - 500$ K), and hence larger disk radii, than the other molecules observed in the Spitzer spectra ($700 - 1100$ K). Indeed, analyses of IRS/Spitzer data by Carr & Najita (2008, 2011) find smaller emitting areas for all molecules relative to H_2O and derive abundance ratios closer to those found here.

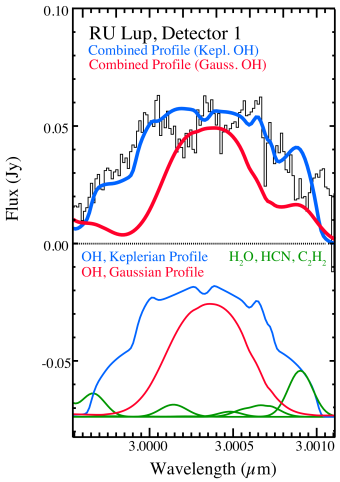

Figure 3.8 Profile for the OH transitions at 3.0 μm for RU Lup, with two different models for the line shape overplotted. A Keplerian profile with a steep decline in surface density and an outer radius of 0.5 AU clearly fits better than the simple Gaussian profile.

Similarly, the IRS/Spitzer wavelength range covers transitions with much lower excitation energies than the transitions probed by NIR observations, and therefore the optical depths measured will be different. Even at the same radial location the Spitzer observations may probe a different vertical location of the disk than the NIR observations. The abundance ratios for the different wavelength regions are also affected differently by the contribution of non-LTE excitation, since radiative pumping and collisional excitation processes can affect different transitions of various molecules in different ways. The OH/H_2O ratio is particularly uncertain since some of the OH emission may be radiatively excited and/or due to direct production into an excited state following photodissociation of H_2O (Bonev & Mumma 2006); the H_2O pure rotational mid-infrared lines are likely to be dominated by collisional excitation whereas the near-infrared lines are likely to be dominated by radiative excitation.

The limitations of the slab model approach highlight the need for proper treatment of the disk geometry and line radiative transfer. In the next section, we address the first slab-model limitation by modeling the near-infrared emission with a disk model including line radiative transfer, in which the emission derives from a range of disk radii and depths. Non-LTE excitation requires a much more sophisticated approach, and we leave this analysis for future work.

3.4 Disk radiative transfer modeling

Since disks are not single-temperature slabs, we have also investigated the molecular emission from a two-dimensional radiative transfer disk model that takes into account both radial and vertical temperature and density variations, the motion of the gas, and the geometry of the disk. The modeling procedure for producing the line intensities and profiles centers around the axisymmetric ray-tracing code called RADLite, the details of which are described extensively in Pontoppidan et al. (2009). RADLite calculates the emission intensity and the spectral line profile for a specific molecular transition by combining the emission from a grid of points across the projected surface of the disk. This allows us to accurately reproduce the effects of the Keplerian rotation of the disk and the radial surface density and temperature profiles of each molecular tracer. The initial temperature and density structure for the disk is calculated using the two-dimensional Monte-Carlo radiative transfer code called RADMC (Dullemond & Dominik 2004), and the dust temperature and source functions for each grid point are generated and then used as input for RADLite. In addition RADMC also calculates the continuum of the source.

RADLite and RADMC offer the opportunity to test a number of different parameters that may affect the disk structure and resulting spectral model, and we present results from models that incorporate several different molecular abundance distributions. Our fiducial model (Model 1) assumes a constant radial and vertical abundance for every molecule, with disk parameters taken from previous observational constraints, primarily from spectral energy distribution fits and submillimeter observations. The exact values of the parameters used for the model for each source are presented in Table 3.4. The model parameters used in RADMC are the mass of the central source ($M_\star$), its radius ($R_\star$) and effective temperature (T_{eff}), the mass of the disk (M_{disk}), outer radius of the disk (R_{out}), a flaring parameter $H/R \propto R^\alpha$, an outer pressure scale height (h_p/R), radial surface density $\Sigma = R^\beta$ and an inner radius (R_i) which sets the inner temperature. The thermal broadening is assumed to dominate the intrinsic line width with the turbulent velocity v_{turb} set to $v_{turb} = \epsilon c_s$ with $\epsilon = 0.03$. The inclination of the disk i is taken from spectro-astrometry of Pontoppidan et al. (2011) and is slightly adjusted (by less than 10°) so a good fit can be found between the model and the data. Model 1 also assumes an effective gas-to-dust ratio of 12800, based on previous modeling of water emission for T Tauri stars using RADLite (Meijerink et al. 2009). This is much higher than the canonical value of 100, but can be explained by the depletion of small dust grains from the surface layers of the disk where our detected emission originates from.

In addition to our fiducial disk model, we varied the abundance structure in RADMC in three different ways in order to test the effects of freeze-out and dust settling. The freeze-out of molecules from the gas to the solid phase may play a role in defining the location and intensity of emission from different molecules

(Meijerink et al. 2008), and the settling of dust to the midplane of the disk can lead to drastic differences in the gas-to-dust ratio in the surface regions of disks at different evolutionary stages. We first tested a density-dependent freeze-out scenario (Model 2), where the molecules are assumed to freeze out on dust grains at a specific temperature which depends on the density of the gas, as described by Pontoppidan (2006). The freeze-out usually starts at ~1 AU, depending on which type of disk is modeled, and the boundary follows the disk horizontally out to large radii. Additionally, we tested an enhanced freeze-out model known as the "vertical cold-finger effect" (Meijerink et al. (2009); Model 3) which models the diffusion of gas to below a horizontal freeze-out boundary by setting the freeze-out location based on the vertical disk temperature structure at a specific radius (see Figure 10 in that paper). In Model 4 we decreased the gas-to-dust ratio by an order of magnitude from 12800 to 1280.

The final model we examine is a disk + disk wind model, which is based on the results presented by Pontoppidan et al. (2011) showing that a Keplerian disk + disk wind can better describe both the line profiles of the broad-based single-peaked CO emission lines observed in a number of bright T Tauri stars, as well as their asymmetric spectro-astrometry signal. The disk wind is a wide-angle non-collimated wind flowing over the surface of the disk that adds a sub-Keplerian velocity distribution to the standard Keplerian disk profile, which mainly contributes an approximately Gaussian core in the inner region of the line profile. The disk wind model consists of gas flowing off of the disk along a set of streamlines with a locus point below the disk at a distance d from the centre of the star (see Figure 10 in Pontoppidan et al. (2011)); this distance d as well as the other specific parameters for the structure of the disk wind are taken from values derived by Pontoppidan et al. (2011) to reproduce the 4.7 μm CO emission line profiles for AS 205 A (for a detailed description of the disk + disk wind model see Pontoppidan et al. (2011) and Kurosawa et al. (2006)). We keep two parameters, the mass loss rate from the disk and effective temperature for the central star (which sets the irradiating flux onto the disk surface), as free parameters in order to allow us to reproduce the central peak of the observed molecular line shapes properly (see the discussion of the modeling results below for more details).

Several additional components for accurately calculating molecular abundances and temperatures are not yet included in our modeling. The disk gas is currently assumed to be coupled with the dust, i.e. the gas temperature is set to be the same as the dust temperature; however, the gas and dust temperatures may be significantly different, although this is difficult to model properly (e.g., Woitke et al. 2009, Gorti & Hollenbach 2008, Glassgold et al. 2009). Also, to calculate the emission intensity for each transition of a specific molecule, the level populations must first be calculated assuming a specific excitation mechanism. The standard formulation assumes local thermodynamic equilibrium (LTE), in which all the level populations are defined by the local temperature at that grid point. However, non-LTE excitation processes such as radiative excitation due to the central star have been shown to be important for OH (Mandell et al. 2008) whereas collisional

excitation controls the H_2O rotational level populations (Meijerink et al. 2009). Such processes will be described for HCN in Bast et al. 2011 (in prep). However, a non-LTE formulation for multiple molecules is time-consuming and difficult to implement. Moreover, collisional rate coefficients for vibration-rotation transitions are largely unknown. We therefore use only LTE excitation in our modeling and reserve the implementation of non-LTE excitation for a future analysis. Since our model is incomplete, we leave an exhaustive parameter study for future work; however, we can begin to compare line intensities and profiles with the data and derive preliminary molecular mixing ratios based on a realistic disk structure.

3.4.1 Disk modeling results

The top and bottom panels in Figure 3.9 present the best fit models for AS 205 A and RU Lup for HCN, H_2O and OH using Model 1 for a constant abundance distribution; Figure 3.10 presents HCN and OH models for DR Tau. The fiducial model produces a double-peaked line profile for all of the molecular species since the bulk of the line intensity originates from the hot inner disk (see Figure 3.11). Since the double-peaked model line profile clearly cannot fit the observed single-peaked line shapes, molecular abundances using the disk-only model are therefore obtained by matching the integrated intensity of the model lines with those of the observed lines; relative abundance ratios (compared with H_2O) are presented in Table 3.3. The best fit for the constant abundance model for AS 205 A resulted in abundances (with respect to H_2) of $x_{HCN} = 2{\times}10^{-7}$, $x_{OH} = 6{\times}10^{-7}$ and $x_{H_2O} = 3{\times}10^{-6}$; however, due to uncertainties in the emission mechanism and the sensitivity of absolute abundances to specific model parameters, abundance ratios provide a more reliable measure for comparison between different objects. Our model as presented in Figure 3.9 does not include higher vibrational excitation lines ($v' > 1$) for HCN from the line list - the LTE model produces detectable lines for excited vibrational transitions but these are not observed for any of these sources. This is likely due to non-LTE excitation of the emitting gas, which produces sub-thermal intensities for higher-energy transitions as shown, for example, for water in Meijerink et al. (2009).

The CO abundance was once again derived by fitting the ^{13}CO lines from our previous CRIRES observations and then multiplying the inferred abundance by 65; for AS 205 A we find $x_{CO} = 1.95{\times}10^{-5}$. For CH_4, an upper limit was obtained for DR Tau, but upper limits were not calculated for NH_3 and C_2H_2 due to the complexity of the spectral region where these molecules are present and the uncertainties in factors such as the line intensities of components within the NH_3 Q branch. Considering the similarity in the abundance ratios for the detected molecules using the slab model compared with the full disk model, we determined that any upper limits calculated for these molecules using the full disk model did not add useful information and might produce spurious results.

As mentioned previously, we tested three disk models in addition to our fiducial

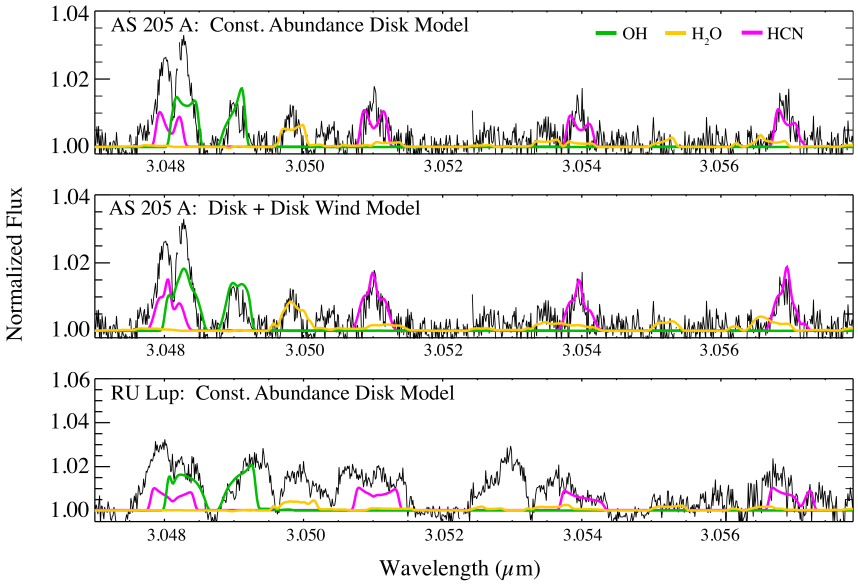

Figure 3.9 RADLite disk model results overplotted on the CRIRES data of AS 205 A (top and middle panels) and RU Lup (bottom planel). The top and bottom panels show results for the disk model only; the middle shows the disk + disk wind model. The disk + disk wind model clearly fits the centrally peaked line shape for AS 205 A much better than the disk-only model.

constant abundance disk model: temperature- and density-dependent freeze-out (Model 2), a vertical cold finger effect (Model 3), and a lowered gas-to-dust ratio (Model 4). Fig 3.12 demonstrates that the line shapes for Models $1-3$ are very similar, due to the fact that the detected line emission in this wavelength region originates from within a few AU and is not modified by either the vertical cold finger effect or the freeze-out (i.e. the molecular condensation fronts), which only affect emission from the outer disk. The HCN line shows a slight decrease in depth for the cold finger model due to the reduced self-absorption of the colder gas; this effect is not seen for the H_2O and OH since the near-IR emission originates from gas within a radius which is smaller than the condensation radius for these molecules even when using the constant abundance model (this is in contrast with the mid-IR lines modeled by Meijerink et al. (2009)). Lowering the gas-to-dust ratio from 12800 to 1280 (Model 4) clearly decreases the line intensity due to the decrease in the amount of emitting gas present above the optically thick dust layer, therefore requiring higher molecular abundances to fit the data. The final abundance ratios between H_2O and OH, HCN, C_2H_2 are not affected by the lowered gas-to-dust ratio but the CO abundances is more sensitive, most likely due to the higher abundance

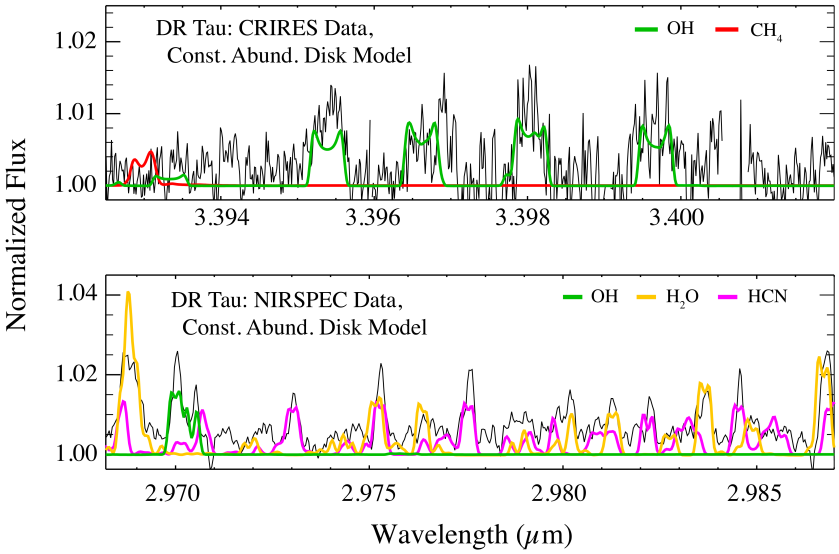

Figure 3.10 RADLite disk model results overplotted on the CRIRES (top) and NIRSPEC (bottom) data for DR Tau. Note that at the NIRSPEC resolution the discrepancy between model and observed line shapes is less noticeable.

of CO across a large vertical scale height (i.e. Walsh et al. (2010)).

The middle panel in Figure 3.9 show the disk + disk wind model for AS 205 A, as discussed above. We originally calculated a model using the parameters for the disk wind derived by Pontoppidan et al. (2011) for these sources from spectro-astrometry of the strong CO features at 4.7 μm. We expected this combined model to produce the most accurate match to the single-peaked line profiles seen in the data. Interestingly, while the fit was better than the disk-only models, this model still produces a double-peaked line profile for HCN and H_2O, while the CO line profile has a central single peak, as illustrated in Figure 3.13. This most likely indicates that the temperature in the disk wind model derived from the CO lines is too low to excite HCN and H_2O sufficiently. We were able to produce an adequate fit to the HCN and H_2O features using a wind model with either an enhanced mass loss rate (×3) or an increased effective temperature for the central star (×2); however, these solutions are clearly ad-hoc and only further emphasize the need for an improved treatment of the disk temperature structure (taking into account the different types of cooling and heating mechanisms) and the chemistry and infrared pumping of the wind. In addition to modeling the line shapes, spectro-astrometry of the HCN, OH and H_2O lines would help to further constrain the location and temperature of the emitting gas.

The molecular abundance ratios of ~0.05 for HCN/H_2O and C_2H_2/H_2O and

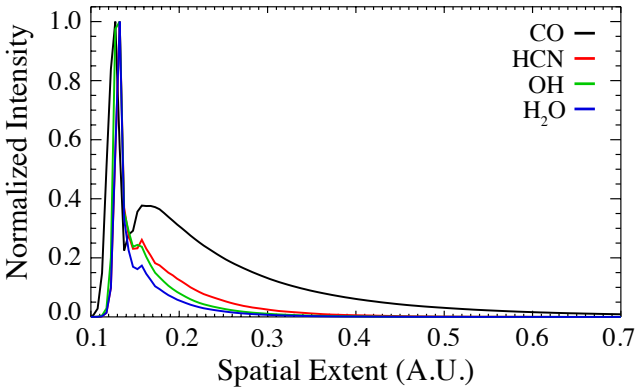

Figure 3.11 Distributions of the four primary molecules derived from disk modeling with RADLite. All of the molecules emit primarily from within 0.2 AU, and only CO has emission extending out to 0.5 AU.

0.2 – 0.3 for OH/H_2O extracted from the models show little difference between the 3 sources, suggesting a common origin for the molecular material and similar excitation conditions. This is not surprising, since we have chosen these three objects due to their similarly bright CO emission and centrally peaked line shape. The relatively good agreement between the slab and disk models reinforces the conclusion by Meijerink et al. (2009) that a slab model can produce reliable results because the emission arises from only a very narrow range of radii (and thus limited range of temperatures) in the disk model and because the emission is largely optically thin (the one exception is the OH line in RU Lup, which shows a complex line shape and therefore leads to somewhat divergent results between the two models). The most dissimilar abundance ratio between the different objects is CO/H_2O, which varies by a factor of 3 between the different sources. The fact that this ratio is larger than unity indicates that H_2O is not the major oxygen reservoir in the surface regions of the inner disk, assuming solar abundance ratios, but the derived values for the CO/H_2O ratio are dependent on the detailed temperature and density structure of the gas and the SED of the underlying dust continuum, and a more comprehensive modeling strategy utilizing a consistent model over a wide range of transition energies is needed to improve these constraints.

3.5 Comparison with chemical models

A number of models of inner disk chemistry exist in the literature, each with different levels of sophistication and each one taking different physical and chemical processes into account (Markwick et al. 2002, Agúndez et al. 2008, Willacy &

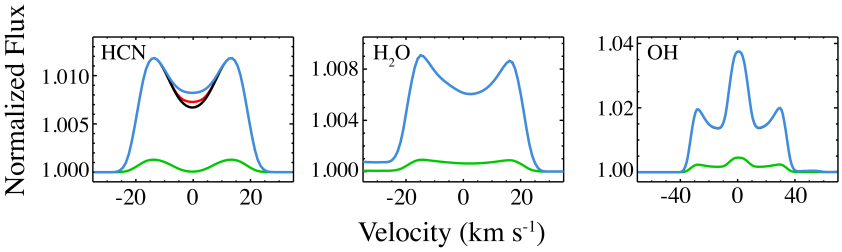

Figure 3.12 Radiative transfer disk models of HCN, OH and H_2O including parameters for AS 205 A. Black = constant abundance (Model 1), red = freeze out (Model 2), blue = "vertical cold finger" model (Model 3) and green = gas-to-dust ratio of 1280 (Model 4; all other models using gas/dust = 12800). The HCN line shows a slight variation for Models 2 and 3 in the line core due to freeze-out at large distances, but emission from the other molecules originates from within the freeze-out distance (the red and black lines underlie the blue line). The emission for the low gas-to-dust model is decreased in amplitude but the line shape does not change.

Woods 2009, Glassgold et al. 2009, Walsh et al. 2010, Najita et al. 2011). The models show a range of molecular ratios; typical HCN column densities relative to H_2O vary from 10^{-4} - 10^{-1} for the warm (T > 200 K) molecular atmosphere of the disk, which agrees well with our results, while OH values relative to H_2O vary between 10^{-5} - 10^{-2}, which is more than an order of magnitude below what we find. Bethell & Bergin (2009) and Najita et al. (2011) have shown that the OH abundance is sensitive to photodissociation of parent molecules by both UV and X-rays, but detailed models including a complete treatment of the radiative environment have not been developed. Additionally, as mentioned above, abundances from both our slab model and disk model are calculated using the assumption that the emission originates from an environment that can be described by LTE, but it has been proven previously by both observations (Mandell et al. 2008, Pontoppidan et al. 2010) and by modeling (Meijerink et al. 2009) that H_2O and OH ro-vibrational line emission in particular are almost certainly enhanced by radiative pumping from the central star, therefore making direct comparisons with models premature. The relative importance of LTE versus non-LTE excitation and de-excitation for all the relevant molecules requires detailed modeling and availability of collisional rate coefficients, and we leave these calculations to future work.

Najita et al. (2011) also explore the effects of larger dust grain sizes, lower accretion-related heating in the disk interior, and differing C/O ratios on the relative molecular abundances. In particular, the ratios for carbon-bearing molecules are especially sensitive to the C/O ratio - values for the HCN/H_2O ratio vary

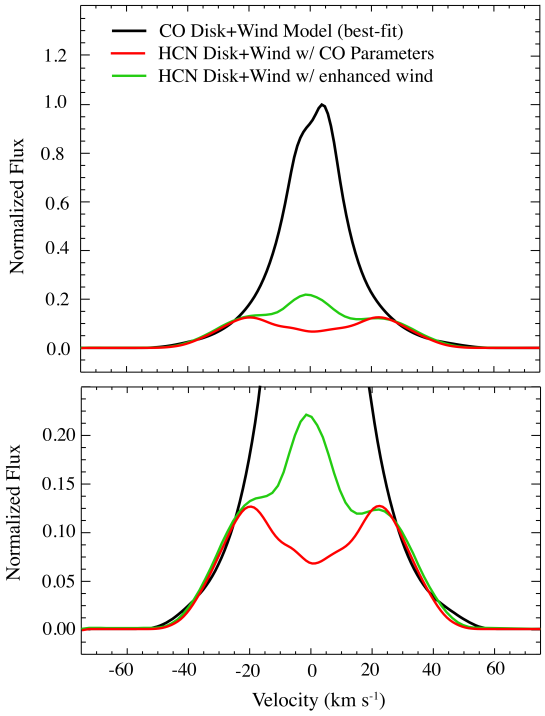

Figure 3.13 A CO (black) and HCN (red) line modeled using the disk wind model parameters for AS 205 A found by Pontoppidan et al. (2011). The HCN line should show a double-peaked profile, but our data clearly shows a profile very similar to the CO line profile. To achieve a centrally-peaked profile (green), we require either a higher mass-loss rate or increased stellar irradiation compared with the values derived for the CO lines.

dramatically from O/C = 0.25 (5×10^5) to O/C = 2.0 ($1{\times}10^{-3}$). Our abundance ratios most closely match their calculated values for O/C = 1.5, with O/C = 1 producing values that are clearly larger than what we find. C_2H_2 abundances vary across an even wider range, and additional processes such as the destruction of PAHs at high temperatures (Kress et al. 2010) may also affect the abundance of acetylene. The detailed impact of processes such as grain destruction and transport on the local O/C ratio and molecular abundances is still largely unexplored, and we leave any additional analysis to future work.

Our reported upper limits for CH_4 and NH_3 provide complementary information to the abundance ratios derived for the simpler organic species. If these molecules are formed primarily through grain surface chemistry in cold gas and then transported to warmer regions, they should then exhibit a different radial and

vertical profile compared with HCN and C_2H_2. Our observed limit on CH_4/H_2O of $< 0.07 - 0.09$ is close to the average CH_4/H_2O ice abundance ratio of 0.05 found toward low-mass protostars, whereas our NH_3/H_2O limits are a factor of $3 - 4$ larger (Öberg et al. 2011). Our limits for CH_4/CO for DR Tau are also similar to upper limits found by Gibb et al. (2004) and Gibb et al. (2007) in an edge-on disk, suggesting that thermal desorption of CH_4 from grains is not efficient in the surface regions of the disk or that CH_4 has been transformed into other species. However, both C_2H_2, HCN and CH_4 can also be produced effectively by high-temperature gas-phase reactions above ~ 600 K (Doty et al. 2002). Agúndez et al. (2008) predict large CH_4 and NH_3 abundances very close to the star ($R < 0.5$ AU), with a sharp drop-off as the gas temperature decreases. Their model ratios with respect to HCN or H_2O are consistent with our observed upper limits except for the innermost rim at ~0.1 AU where the model CH_4 abundance becomes higher than that of HCN. Willacy & Woods (2009) predict similarly low abundance ratios of both CH_4 and NH_3, and attribute the low NH_3 values to efficient conversion to HCN in the warm inner disk.

In future work we will expand our modeling with RADLite to explore additional parameter space with regard to these disk characteristics. We will also augment our radiative transfer modeling to include the contribution from non-LTE radiative pumping, in order to allow us to model both the NIR and MIR emission in a self-consistent manner. Another important constraint when modeling emission lines is the gas temperature, which here is set to be the same as the dust temperature. Both Glassgold & Najita (2001) and Kamp & Dullemond (2004) show that the gas is decoupled from the dust, hence future models that can include different temperatures for the dust and the gas would be better able to model the molecular line emission from T Tauri stars.

3.6 Conclusions

We have successfully detected emission from organic molecular gas tracers in T Tauri disks in the NIR for the first time. Emission from HCN as well as H_2O and OH was detected from all three sources, and we detected emission from several transitions of C_2H_2 in AS 205 A. Strong upper limits were placed on emission from CH_4 in DR Tau and on NH_3 in AS 205 A and RU Lup. Based on models, the emission likely arises from the inner $0.1 - 1$ AU of the disk. These first detections demonstrate the feasibility of constraining molecular abundance ratios and temperatures for organic molecules in the planet-forming regions of circumstellar disks using spectrally resolved NIR transitions, and allow us to begin to constrain models of disk chemistry, dynamics and structure. These results provide a direct comparison to observations of unresolved emission from the same molecules observed in the same sources with the Spitzer telescope and upcoming observations with the Atacama Large Millimeter Array (ALMA).

Acknowledgements

AMM is supported by the Goddard Center for Astrobiology. JEB is supported by grant 614.000.605 from Netherlands Organization of Scientific Research (NWO). EvD acknowledges support from a NWO Spinoza Grant and from Netherlands Research School for Astronomy (NOVA). The authors are very grateful to Klaus Pontoppidan for his central role in the CRIRES observations and for making his RADLite program available. They also thank Daniel Harsono for help with the disk modeling, and the anonymous referee for helpful suggestions for improving the manuscript. This research made use of the ESO/ST-ECF Science Archive Facility. Some of the results herein were obtained at the W. M. Keck Observatory, which is operated as a scientific partnership among the California Institute of Technology, the University of California, and NASA. The Observatory was made possible by the generous financial support of the W. M. Keck Foundation.

IV

Investigation of HCN excitation in protoplanetary disks[1]

Context HCN absorption and emission vibration-rotation lines originating from inner planet-forming zones of protoplanetary disks have so far been modeled using local thermodynamical equilibrium (LTE) slab and disk models. However, it has not yet been investigated whether LTE is a good approximation for these HCN emitting regions.
Aim This study investigates how the HCN excitation at 3 and 14 μm is impacted by non-LTE conditions and radiative pumping.
Methods Observed line fluxes at 3 and 14 μm are compared with modeled line fluxes by using a radiative transfer slab and disk model assuming LTE. These line fluxes are then compared to the modeled line fluxes using a non-LTE slab model with different excitation temperatures, volume densities and column densities of HCN. An infrared radiation field is also included to see how the line fluxes are impacted by radiative pumping.
Results The 3 μm line flux reaches LTE at a much higher density of around 10^{14} cm^{-3} relative to the 14 μm line fluxes which reaches LTE at around 10^{9} cm^{-3}. This means that the 3 μm line fluxes are much less well modeled by assuming LTE. In addition it is shown that radiative pumping can significantly impact the line fluxes, especially of the 3 μm lines. The observed 3 μm /14 μm flux ratio cannot be modeled by a LTE slab model unless the volume density is 10^{13} – 10^{14} cm^{-3} at a temperature of $\sim$ 900 K which is at least 1 to 2 magnitudes higher than the expected volume density in the region from which this emission is assumed to originate. However, the observed flux ratio can be modeled when including non-LTE and radiative pumping using densities as low as 10^{9} cm^{-3} at a temperature

[1] J.E. Bast, S. Bruderer, D. Harsono, B. Brandl, A.G.G.M. Tielens and E. F. van Dishoeck

of 900 – 1200 K.
Conclusions Both LTE slab and disk models overestimate the 3 μm and to some extent the 14 μm HCN line fluxes and hence underestimate the HCN abundance. The conclusion can therefore be made that non-LTE conditions and radiative pumping are important to implement in future protoplanetary disk models.

4.1 Introduction

The first million years of a low mass star's life is an exciting period since this is the time when the gas and dust, mainly in the inner part (< 10 AU) of the disk around the star, transforms into building blocks for new planets. It is important to determine the chemical composition and evolution of the gas in these parts of the circumstellar disks since they provide the initial conditions for the type of atmospheres, surfaces and structures that these planets will consist of. One way to extract information about the chemistry in these disks is to observe which molecules are present and determine their relative abundances. In addition information about the physical conditions such as the temperature, which type of radiation dominates in different regions, the density of the gas and the ratio between the gas and dust will decide the chemical evolution of the gas in the disks. Several studies have been done of different molecules by detecting their emission lines in the planet-forming regions of disks, such as CO (e.g., Najita et al. 2003, Brittain et al. 2003, 2007, 2009, Blake & Boogert 2004, Pontoppidan et al. 2008, Salyk et al. 2011b, Brown et al. subm.); OH, H_2O (Carr et al. 2004, Carr & Najita 2008, Mandell et al. 2008, Salyk et al. 2008, Najita et al. 2010, Pontoppidan et al. 2010, Salyk et al. 2011, Carr & Najita 2011, Fedele et al. 2011); and HCN, C_2H_2, and CO_2 (Carr & Najita 2008, 2011, Najita et al. 2010, Salyk et al. 2011, Mandell et al. 2012). In some cases also absorption in edge-on disks has been used to detect HCN, C_2H_2, and CO_2 (Lahuis et al. 2006, Gibb et al. 2007, Doppmann et al. 2008, Kruger et al. 2011, Bast et al. subm.).

These studies use observations of molecular lines to infer the abundance structure of the molecule of interest by adopting either a slab or disk model. By modelling the lines also physical conditions such as the temperature of the emitting gas can be estimated. However these models mainly use local thermodynamical equilibrium (LTE) as an approximation to model the lines. This means that a single temperature sets the population of the excitation levels of the molecule by using the Boltzmann equation and that by implication the density is very high in order to thermalize the levels. This assumption is used since including non-LTE processes, especially in radiative transfer disk models, is complicated. In addition in many cases collisional rate coefficients for the specific molecule of interest have yet not been measured or calculated which are needed to model the lines under non-LTE conditions. The inner regions of protoplanetary disks have so far been assumed to have such high temperatures and densities so that LTE is a good approximation. However a recent study of water emission lines originating from

within 0.2 AU of the disk done by Meijerink et al. (2009) shows that using LTE in a disk model can introduce large errors in both the H_2O abundance and temperature structure of the emitting gas. That LTE is not a good approximation can be explained by the fact that the main part of the IR emission from the water lines arises in the surface of the disk where the densities are too low to provide the conditions needed for LTE. The errors in the estimated water abundance will also impact the entire view of the chemistry and chemical evolution of the disks. Since water is such an important molecule in the reaction network to form many other molecules in the disk, it is very important to have a correct determination of its abundance.

HCN is another important reactant in the chemical network of these disks (Agúndez et al. 2008, Walsh et al. 2012). Besides its role in the chemistry, HCN has another valuable characteristic, namely a dipole moment. The dipole moment means that it can be observed both at infrared wavelengths, through its rovibrational transitions, and at millimeter wavelengths, through its pure rotational transitions. This means that HCN is one of the few molecules that simultaneously can probe both the inner and outer parts of the disk and therefore can help to understand how the chemical structure of the disk changes with radius.

Observations of HCN suggest that the infrared emission from this molecule has a very similar origin as the water infrared emission (Salyk et al. 2011, Mandell et al. 2012). Salyk et al. (2011) used a LTE slab model to model the HCN Q-branch lines of the unresolved ν_2 mode at 14 μm observed using *Spitzer*. Mandell et al. (2012) modeled their observed HCN ν_3 mode emission lines at 3 μm by using both a LTE slab model and a radiative transfer disk model assuming LTE in each grid point of the disk. It was shown that the inferred abundance ratios of HCN relative to other observed molecules did not differ much between the two methods, probably because the errors introduced by the LTE assumption are comparable for the various species. However, the absolute abundances depend much more sensitively on the adopted method. HCN has also been detected through absorption lines in two sources at 14 μm by Lahuis et al. (2006) and Bast et al. (subm.) and one source at 3 μm by Gibb et al. (2007) and Doppmann et al. (2008) using a LTE absorption slab model. Again, only abundances relative to other molecules have been derived. Neither the emission nor the absorption observations of HCN have ever been modeled using a non-LTE slab or disk model.

Since describing the water emission using a non-LTE disk model has been proven to be a better approach than assuming LTE a similar investigation is performed here for HCN. As a first step, we investigate here the non-LTE effects on the 3 and 14 μm lines by comparing a LTE and non-LTE slab model rather than a full disk model. This will allow us to obtain insight into how non-LTE excitation impacts the line fluxes and whether this translates into different conclusions between line emission at 3 and 14 micron. A disk model is used to determine the typical temperatures and densities in the regions from which the 3 and 14 μm lines originate and to provide a reference for comparison with LTE excitation. In addition the impact of an infrared radiation field inducing radiative pumping is studied to see

which type of excitation processes of HCN are important in these regions. These results will decide if non-LTE and radiative pumping effects are important to include in the development of future radiative transfer models of protoplanetary disks (Bruderer et al., in prep.) and therefore also in the determination of the HCN abundance structure in the disks.

The different vibrational modes of the HCN molecule and the observations of HCN emission at 3 are 14 μm that the models will be compared with are presented in Sections 4.2 and 5.2. Section 4.4 starts with a description of the LTE radiative transfer disk model to determine the HCN emitting regions. Subsequently, the non-LTE radiative transfer slab model with and without radiative pumping and their results are presented and compared. The results and their conclusions are summarized in Section 5.5.

4.2 HCN emission at 3 and 14 μm

HCN is a linear tri-atomic molecule with three rotational-vibrational modes. These three modes are:

- ν_1 – the C-N stretch at 4.786 μm.
- ν_2 – a doubly degenerate bending at 14.043 μm at E_u=1025 K.
- ν_3 – the C-H stretch at 3.019 μm at E_u=4765 K.

The two modes that will be further investigated here are the ν_2 and ν_3 modes since they are observable at NIR and MIR wavelengths. The ro-vibrational transitions of the ν_1 mode have very low Einstein A coefficients and have so far not been observed so this mode will therefore not be further investigated. The ν_2 mode is a $\Pi \rightarrow \Sigma^+$-transition which has a P-,Q- and R-branch following the selection rules. The ν_3 mode is a $\Sigma^+ \rightarrow \Sigma^+$ transition which only allows $\Delta J = \pm 1$, so it has a P- and R-branch but no Q-branch.

4.3 Observations

Observations of the ν_3 mode at 3 μm in emission have been presented by Mandell et al. (2012), where they show detections of HCN for 3 different T Tauri stars, AS 205 N (the northern component), DR Tau and RU Lup. AS 205 N and RU Lup were observed using the spectrometer CRIRES at the Very Large Telescope (VLT) at a spectral resolving power of $R = \lambda \,/\, \Delta\lambda = 96{,}000$, whereas the HCN detection in DR Tau was done with the spectrometer NIRSPEC at the Keck telescope with $R = 25{,}000$.

The ν_2 mode at about 14 μm was detected in 24 out 48 T Tauri stars (Salyk et al. 2011) using Spitzer. All three T Tauri stars, AS 205, DR Tau and RU Lup, that show HCN detections at 3 μm also have detections at 14 μm. In this article,

Table 4.1 Parameters used in the specific fiducial disk model for AS 205.

Parameters		Ref.[a]
$M_\star$ [$M_\odot$]	1.0	1
$R_\star$ [$R_\odot$]	3.7	1
T_{eff} [K]	4250	1
M_{disk} [$M_\odot$]	0.029	1
R_{out} [AU]	200	1
R_i [AU]	0.14	1
h_p/R	0.21	1
α	0.11	1
β	-0.9	1
i [^{o}]	20	2

[a]References: (1) Andrews et al. (2009) and (2) Pontoppidan et al. (2011)

AS 205 will be taken as the standard disk for which models of the HCN lines will be made and compared with the observations. Our observations of AS 205 at 3 μm (Mandell et al. 2012) show that the P(11) line at 3.0508 μm has an absolute flux of 5.6 $\cdot 10^{-15}$ erg cm^{-2} s^{-1} with a calibration uncertainty of about 30%. This can be compared with the total absolute line flux between 13.837 – 14.075 μm of 2.2 $\cdot 10^{-13}$ erg cm^{-2} s^{-1} taken from Salyk et al. (2011). The flux ratio F_3/F_{14} between the line fluxes at 3 and 14 μm is therefore 2.5 $\cdot 10^{-2}$ with an uncertainty of about 40%. It is important to note that AS 205 is a binary and that the P(11) 3 μm line observed with CRIRES resolves the binary, with the reported flux consisting of just the emission from AS 205 N. In contrast, the 14 μm line flux applies to both sources since Spitzer cannot resolve the binary. The assumption is that the majority of the 14 μm line flux comes from AS 205 N. This seems to be a reasonable assumption since the F_3/F_{14} flux ratio is 9.0 $\cdot 10^{-2}$ and 1.1 $\cdot 10^{-2}$ for RU Lup and DR Tau respectively based on using the R(6) and R(17) lines at 3 μm for these sources.

4.4 Radiative transfer models and their results

Three different types of models will be used to simulate the excitation of HCN to investigate which model can best describe the observed line emission. These models are a LTE radiative transfer disk model, a non - LTE radiative transfer slab model and a non-LTE radiative transfer slab model including radiative pumping.

4.4.1 A standard disk model using LTE

As a first step, a LTE disk model is run to investigate how the HCN flux ratios from such a model compare with the observations. In addition this model provides an indication of the regions of the disk from which the 3 and 14 μm lines originate and their physical conditions. The continuum radiative transfer disk model called

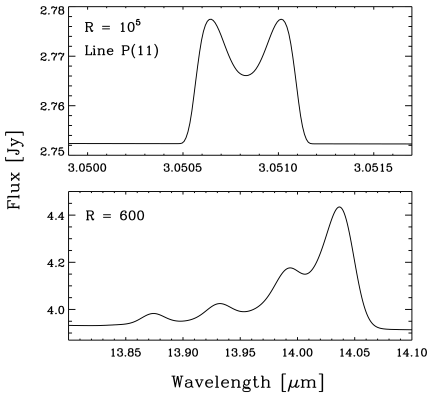

Figure 4.1 Modeled HCN emission using the radiative transfer disk model RADLite for AS 205 N at two different spectral resolving power R=600 (*Spitzer*) and 10^5 (CRIRES-VLT). In the upper figure the P(11) line at 3 μm is shown and in the lower figure the HCN emission lines between 13.837 – 14.075 μm.

RADMC (Dullemond & Dominik 2004) was used together with the line raytracing code RADLite (Pontoppidan et al. 2009) to model the 3 μm P(11) line and the 14 μm line emission between 13.837 – 14.075 μm, see Fig. 4.1. This model takes into account both radial and vertical temperature and density variations, the motion of the gas, the continuum opacity and the geometry of the disk.

The disk model parameters used in RADMC are those appropriate for the circumstellar disk of AS 205 N. This disk is chosen to be a good model for a typical protoplanetary disk since it has been modeled in detail before and its disk parameters are reasonably well known (Andrews et al. 2009, Pontoppidan et al. 2011). The different parameters are: the mass of the central source ($M_\star$), its radius ($R_\star$) and effective temperature (T_{eff}), the mass of the disk (M_{disk}), outer radius of the disk (R_{out}), a flaring parameter $H/R \propto R^\alpha$, an outer pressure scale height (h_p/R), radial surface density $\Sigma = R^\beta$ and an inner radius (R_i) which sets the inner temperature, see Table 1. The initial values for these parameters are taken from previous observational constraints, primarily from sub-millimeter observations (Andrews et al. 2009), and are the same as adopted in (Mandell et al. 2012). Figure 4.2 shows the density and temperature structure of the modeled disk.

The modeling procedure for estimating the line intensities centers around the axisymmetric ray-tracing code called RADLite, the details of which are described extensively in Pontoppidan et al. (2009). RADLite calculates the emission intensity and the spectral line profile for a specific molecular transition by combining the emission from a grid of points across the projected surface of the disk. This allows us to accurately reproduce the effects of the Keplerian rotation of the disk and

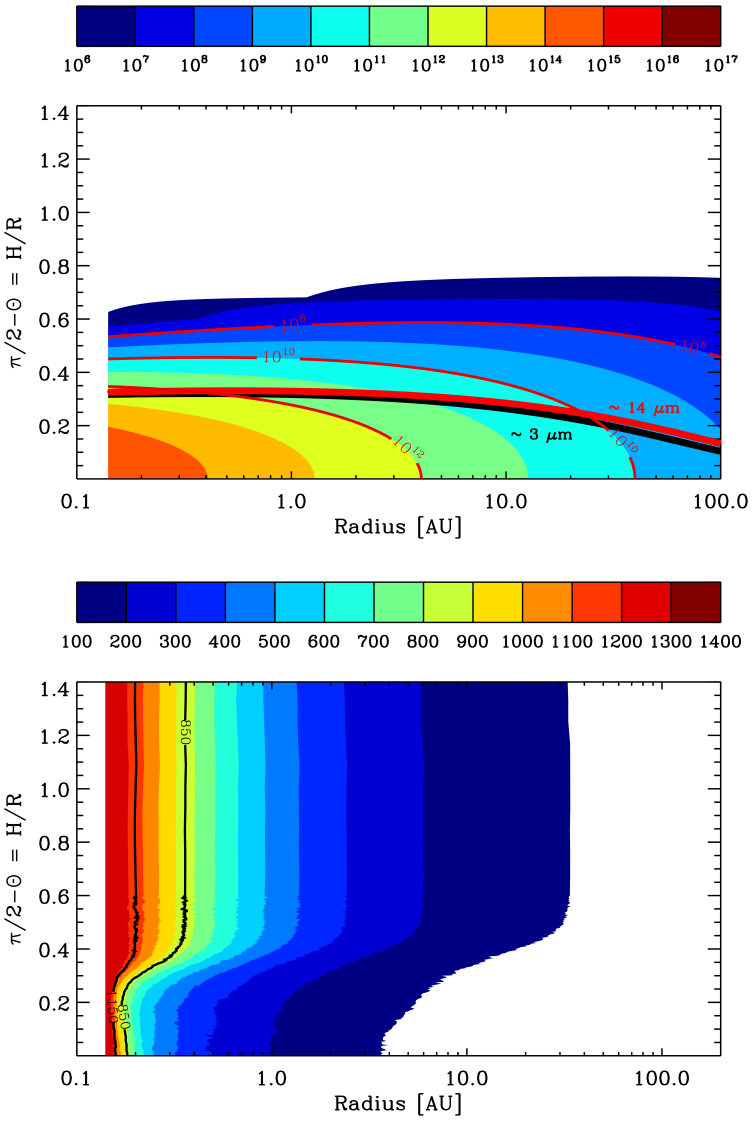

Figure 4.2 Upper panel: Contour plot of the adopted density distribution in the AS 205 N protoplanetary disk. The dark red solid lines mark the densities 10^8, 10^{10} and 10^{12} cm^{-3} and illustrate the region in the disk where the HCN emission originates. The red and black broader solid lines represent where the dust reaches an optical depth of $\tau = 1$ for 14 μm and 3 μm lines, respectively. Lower panel: Contour plot of the adopted temperature distribution in the AS 205 N protoplanetary disk. The black solid lines mark the temperature range between 850 – 1150 K and illustrates the region in the disk where most of the HCN emission originates.

Table 4.2 Observations of the R(11) line flux at 3 μm and the 14 μm total line flux between 13.837 – 14.075 μm and their modeled fluxes using a LTE protoplanetary disk model.

	Observations	LTE disk Model[a]
3 μm P(11) line [erg cm^{-2} s^{-1}]	$5.6 \cdot 10^{-15}$	$3.5 \cdot 10^{-15}$
14 line emission (13.837 – 14.075 μm) [erg cm^{-2} s^{-1}]	$2.2 \cdot 10^{-13}$	$5.1 \cdot 10^{-13}$
3/14 μm flux ratio	$2.5 \cdot 10^{-2}$	$6.8 \cdot 10^{-3}$

[a] A relative HCN abundance of $2.0 \cdot 10^{-7}$ to H_2 is used in the models.

the radial surface density and temperature profiles. The initial temperature and density structure of the disk is calculated using the RADMC two-dimensional continuum Monte-Carlo radiative transfer code using standard dust opacities (Dullemond & Dominik 2004), and the dust temperature and source functions for each grid point are generated and then used as input for RADLite. The gas is currently assumed to be coupled with the dust, i.e., the gas temperature is set to be the same as the dust temperature. The gas/dust ratio is set to 12,800 which is based on earlier modeling of water emission lines in T Tauri stars using RADLite (Meijerink et al. 2009) To calculate the emission intensity, the level populations must first be calculated assuming a specific excitation mechanism. The standard formulation assumes local thermodynamic equilibrium (LTE), in which all the level populations are defined by the local temperature at that grid point.

LTE line fluxes and ratio

A relative HCN abundance of $2.0 \cdot 10^{-7}$ to H_2 was used to model the P(11) line at 3 μm and the lines between 13.837 – 14.075 μm since this was the relative abundance that Mandell et al. (2012) found when they fitted the 3 μm lines for AS 205 using LTE excitation. The modeled lines can be seen in Fig. 4.1. The line flux of the P(11) line is about $3.5 \cdot 10^{-15}$ erg cm^{-2} s^{-1} which is close to the observed flux of $5.6 \cdot 10^{-15}$ erg cm^{-2} s^{-1}. The modeled lines between 13.837 – 14.075 μm have a total flux of $5.1 \cdot 10^{-13}$ erg cm^{-2} s^{-1} which is about a factor of two higher than the observed total line flux of $2.2 \cdot 10^{-13}$ erg cm^{-2} s^{-1}. The 3 /14 μm flux ratio in this model is inferred to be $6.8 \cdot 10^{-3}$, about a factor of 4 lower than the observed flux ratio of $2.5 \cdot 10^{-2}$, see Table 4.2. Hence either the 3 μm flux is underestimated or the 14 μm flux is overestimated when using the LTE radiative transfer disk model. This may reflect that the disk photosphere, which is the region assumed to be the origin of both the 3 and 14 μm line emission, has a range of densities below the critical densities of these two transitions. Densities below the critical density means that collisions cannot maintain the level populations and, hence, a LTE model will not describe the emission well. In addition, the lines may be radiatively pumped by the stellar or disk radiation field. Radiative pumping will also drive the populations on the different excitation levels away from LTE values.

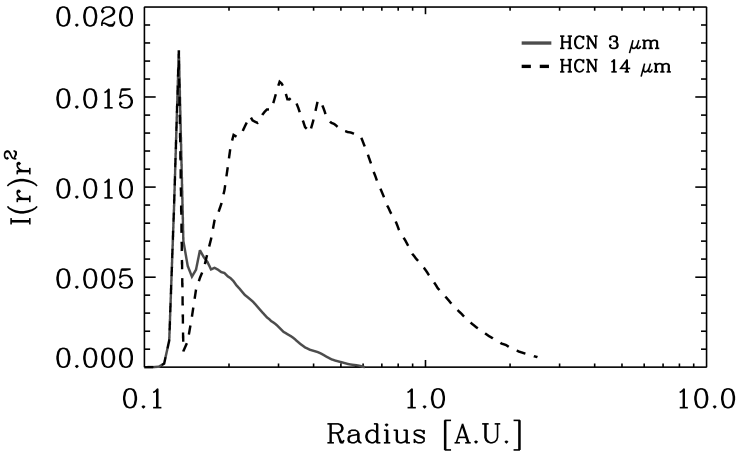

Figure 4.3 The spatial extent of HCN at 3 μm and 14 μm based on characteristics of AS 205 N LTE model (see Table 4.1). The inclination is set to 45^o for illustration purposes.

Spatial extent of 3 versus 14 μm emission

The spatial extent of the 3 relative to the 14 μm emission is important to investigate since this will help to understand the HCN excitation processes that dominate in different regions of the disk. An estimate of the distribution of the 3 and 14 μm emission is therefore made using the raytracing code RADLite, which can, by using the temperature and density structure from RADMC, calculate an intensity image containing an isovelocity curve for a given line and velocity. An isovelocity curve consists of the emission for a specific line at a certain velocity which originates alongside the curve of the disk for which the projected velocity is constant. For more details see Pontoppidan et al. (2009). An image cube consisting of a sample of intensity images within a velocity range of -100 – $+100$ km s^{-1} with a sampling of 0.5 km s^{-1} was made for the 3 μm P(11) line and for the 14 μm R(17f) line. The disk parameters used are those given in Table 4.1. However, an inclination 45^o is used to get a symmetric distribution in the intensity map along the cut through the center of the disk. The intensity map accounts only for emission from the upper surface of the disk which is directed toward the observer since the other side is not seen due to the fact that the disk is optically thick to the continuum photons and hence the view from the other side of the disk is blocked by the dust.

The images in the intensity maps in the image cube were then added and the total intensity along a cut through the disk times R^2 is plotted in Fig. 4.3, where R is the radius of the disk. The intensity times R^2 is chosen since the integrated area of the curve will give the contribution of that region to the flux of the line.

As can be seen in Fig. 4.3 both lines show two peaks. The primary peak close to the star is the emission which comes from the hot inner rim of the disk where it is hit directly by the radiation from the star and the secondary peak represents the emission originating a bit further out in the flared disk where the gas is warm enough to excite and emit the 3 and 14 μm line emission, respectively. More than 50% of the 3 μm line emission originates from within 0.2 AU (for an inner radius of 0.14 AU), whereas about 50% of the 14 μm line emission originates within 0.4 AU. The 14 μm emission is therefore, as expected, excited in a somewhat colder gas region of the disk than the 3 μm emission. Based on these results, we will assume that most of the HCN emission comes from a region in the disk within a temperature range of 850 – 1150 K and volume density range of 10^8 –10^{12} cm^{-3} (Fig. 4.2). The density estimate is in addition based on the fact that the dust reaches $\tau = 1$ within that density range for the 3 and 14 μm continuum emission. This is specified in Fig. 4.2 where $\tau = 1$ is emphasized with a black and red line for 3 respectively 14 μm. It is important to note however that the spatial distributions are based on the temperature and density structure estimated by RADMC, which does not separate the gas and dust temperatures in the disk surface, so it will underestimate the contribution from hot material at larger distances.

4.4.2 Non-LTE excitation of HCN using a slab model

The non-LTE radiative transfer slab model RADEX (van der Tak et al. 2007) is used to model both the 3 μm (in the P(11) line) and 14 μm (the integrated intensity between 13.837 – 14.075 μm) line emission fluxes to investigate how the fluxes change with the column density of HCN, the kinetic temperature and the volume density of H_2. Other input parameters, which we will keep fixed in our analysis, are the width of the molecular line ΔV which is here set to 1 km s^{-1}, the cosmic microwave background radiation which is set to be the same as that from a blackbody with a temperature of 2.73 K and the characteristics of the collisional partners for which we will adopt H_2. All results scale as $N/\Delta V$. The molecular data for HCN include the statistical weights and energies for all levels and the Einstein A coefficients for all radiative transitions.

For pure rotational transitions within the ground vibrational state, the collisional de-excitation rate coefficients were taken from the Leiden atomic and molecular database (Schöier et al. 2005) based on the data from Dumouchel et al. (2010). Data are only available for temperatures up to 500 K. For temperatures above 500 K, the collisional de-exciation rate coefficients have been set equal to those at 500 K for the different line transitions and the mean velocity dependence on temperature is ignored. To obtain rate coefficients for pure rotational transitions within the excited vibrational states, the v=0 values were scaled using the formulation of Chandra & Sharma (2001). For transitions between vibrational states, experimental measurements at 300 K have been made by Smith & Warr (1991,their Table 2). These values apply to the vibrational bands as a whole. Collisional rate

coefficients for individual vibration-rotation transitions have been derived by D. Harsono using a modified version of the formulation of Clary (1983).

The upward collisional rate coefficients (C_{lu}) are determined using Equation 4.1,

$$C_{lu} = \frac{g_u}{g_l} C_{ul} \exp[-E_{ul}/kT], \tag{4.1}$$

where E_{ul} is the energy difference between the two levels and g_u and g_l are the statistical weights for the upper and lower level.

The experimental data of Smith & Warr (1991) show that collisional de-excitation of the ν_2 band at 14 μm by H_2 is much more rapid (by a factor of ~300) than that of the ν_3 band at 3 μm. Typical values are $1.5 \sim 10^{-11}$ and 5×10^{-14} cm^{3}s^{-1}. Since the Einstein A coefficients of the two bands are 3.3 and 81.7 s^{-1}, respectively, this means that the critical densities A_{ul}/C_{ul} are 2×10^{11} and 1.6×10^{15} cm^{-3}. Thus, the densities needed to excite the 3 μm band are roughly 4 orders of magnitude larger than those for the 14 μm band. Results of the non-LTE calculations are presented below in §4.4.

4.4.3 Non-LTE slab model including radiative pumping

Besides collisions, the HCN lines can also be radiatively pumped. To investigate how this will affect the line fluxes for the 3 and 14 μm emission, an IR radiation field was added in the non-LTE slab model simulated by RADEX. The radiation field is estimated using the RADMC radiative transfer code for the AS 205 disk model using the parameters given in Table 1. Using the resulting dust temperature and density structure, a radiation field in each grid point in the modeled disk is computed. The radiation field in the grid points within the temperature range 850 – 1150 K and volume densities of 10^8, 10^{10} and 10^{12} cm^{-3} has been extracted. These temperature and density ranges were selected because the LTE analysis in Section 4.4.1 shows them to be typical for the region from where the HCN line emission originates. At wavelengths larger than a few micron the photon noise in this Monte Carlo method is considerable and we have smoothed these results. The radiation field does not change much within the volume density range of 10^8 – 10^{12} cm^{-3}. Hence we have adopted the average radiation field indicated by the red line. The blue line shows a blackbody for 1000 K which is clearly not a good approximation for the averaged radiation field. However, the green line shows a blackbody for 1000 K, scaled with the dilution factor W set to 0.2, which provides a fair fit to the radiation field at wavelengths > 3 micron. In these calculations, we will adopt a blackbody at 1000 K with a dilution factor of 0.02 and 0.2 to estimate the effect of a radiation field on the HCN line emission (see Fig. 4.4).

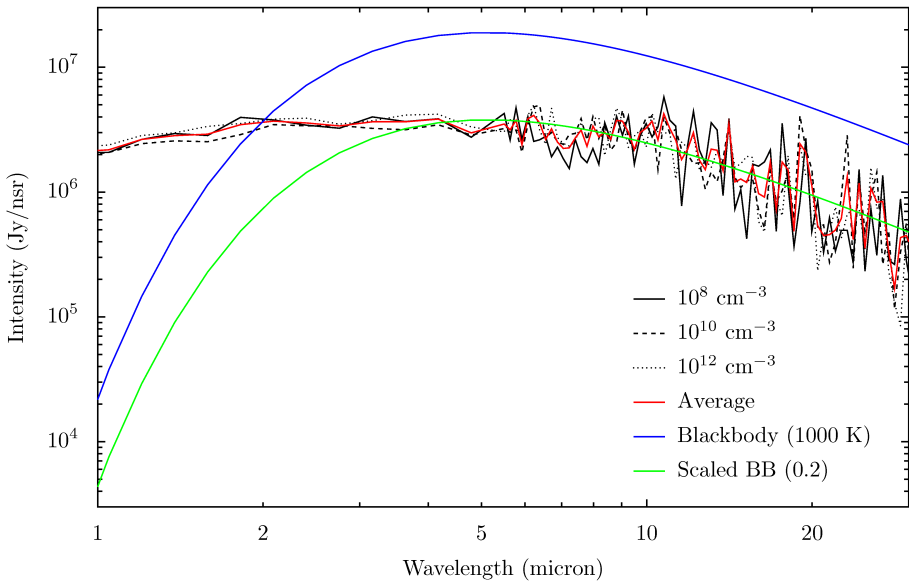

Figure 4.4 The extracted radiation field (in black) using the radiative transfer model RADMC of the standard AS 205 disk for three different volume densities: 10^8 (solid), 10^{10} (dotted) and 10^{12} cm^{-3} (dashed). Their average radiation field is plotted in red. The radiation from a blackbody at 1000 K is plotted in blue and the same blackbody with a dilution factor of 0.2 is presented in green.

4.4.4 Results introducing non-LTE and radiative pumping of HCN

Figure 4.5 shows the 3 and 14 μm line fluxes as a function of the volume density of H_2 for four different temperatures, 300, 600, 900 and 1200 K, and two different HCN column densities 10^{13} (black line) and 10^{15} cm^{-2} (red line). The ratio of the 3 and 14 μm fluxes is shown in the bottom 4 panels shown in Fig. 4.5. In addition, the computed fluxes including the radiation field with a dilution factor of 0.2 (dashed lines) and a radiation field including a dilution factor of 0.02 (dashed dotted lines) are plotted in the figure.

Fig. 4.5 shows, as expected, that the flux (not including a radiation field) increases with both the volume density and the column density. At low density, the line flux increases with $n(H_2)N(HCN)$ and hence, for constant column density, the line flux scales linearly with density. At high densities ($n >> n_{cr}$), the line fluxes scale with N(HCN) and becomes independent of $n(H_2)$. The main difference between the 3 and 14 μm lines is that the 14 μm flux starts to flatten out at around 10^9 cm^{-3} while the 3 μm flux keeps increasing until a much higher density of 10^{14} cm^{-3}. Essentially the 14 μm flux reaches LTE, hence collisional excitation takes over, at a much lower density than the 3 μm flux. This reflects the much higher critical density for the 3 μm line (10^{15} cm^{-3}) than the 14 μm emission lines (10^{11} cm^{-3}). It can clearly be seen in the figure that the 3/14 μm flux ratio is sensitive to density between 10^9 and 10^{14} cm^{-3}, i.e., the density range where the 14 μm levels have reached LTE while the 3 μm flux still increases. However, as expected, no difference in the 3/14 μm flux ratio is apparent between the two different column densities of 10^{13} and 10^{15} cm^{-2} since both types of lines are optically thin.

Another way to plot these results is shown in the left and middle panel of Fig. 4.6 which presents loci in the $n - T$ plane of a constant flux (10^{-8}, 10^{-7} and 10^{-6} erg cm^{-2} s^{-1} for the 3 μm line P(11) and 0.01, 0.05 and 0.1 erg cm^{-2} s^{-1} for the 14 μm flux) for the two different HCN column densities 10^{13} and 10^{15} cm^{-3}. These figures illustrate that when the density is lowered a higher gas temperature is needed to give the same flux of the line and that this effect is stronger for the 3 μm emission than the 14 μm emission. Essentially, the line flux scales with the Planck function at the excitation temperature of the levels. For a two level system, the excitation temperature, T_x is given by

$$\frac{T_x}{T} = \left[1 + \frac{kT}{E_{ul}} \ln\left(1 + \frac{n_{cr}}{n}\right)\right]^{-1} \tag{4.2}$$

Thus for a lower density a higher temperature is needed to collisionally excite the lines to achieve the same intensity in the lines. Only when the density exceeds the critical density will (T_x) approach T and will the line flux become constant. Because E_{ul} is larger for the emission at 3 μm than for the emission at 14 μm, the 14 μm lines need less of a temperature change to compensate for a change in the volume density as the 3 μm emission. The right panel of Fig 4.6 shows the

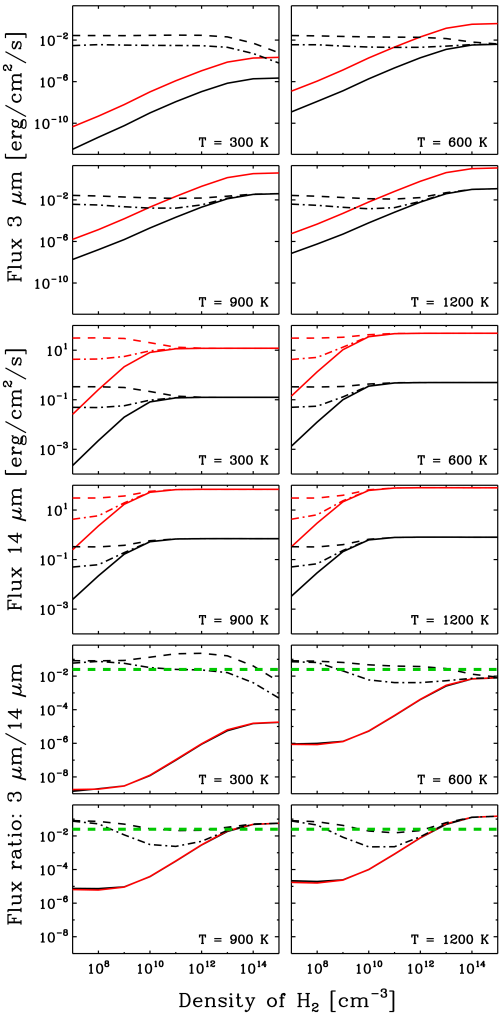

Figure 4.5 The modeled line flux of the HCN P(11) line (3.0305 μm), the total HCN line flux between 13.837 – 14.075 μm and the 3/14 μm line flux ratio as a function of density using a slab model at four different temperatures 300, 600, 900 and 1200 K and for two different column densities. The dashed lines represent a slab model for a HCN column density of 10^{13} cm^{-2} including a radiation field using a blackbody of 1000 K which is scaled with a dilution factor of 0.2 and the dashed-dotted line includes a radiation field using a blackbody for 1000 K which is scaled with a dilution factor of 0.02. The two different HCN column densities (10^{13} and 10^{15} cm^{-2}) are represented by the black and red color on the different types of lines. The observed 3/14 μm line flux ratio for AS 205 N is shown in the four lower panels (green dashed line).

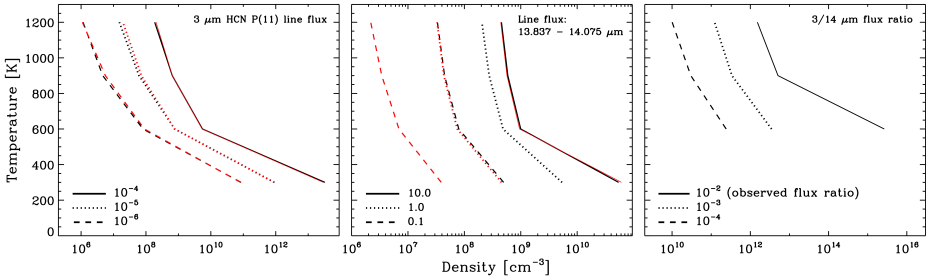

Figure 4.6 Curves of constant P(11) HCN line flux, 13.837 – 14.075 μm total HCN line flux and 3/14 μm HCN flux ratios are plotted as a function of density and temperature for models without radiative excitation. Black (red) lines are for a column density of 10^{13} (10^{15}) cm^{-2}. Left panel: The three different fluxes are 10^{-6} (dashed line), 10^{-5} (dotted line) and 10^{-4} (solid line) erg cm^{-2} s^{-1}. Middle panel: The three different fluxes are 0.1 (dashed line), 1.0 (dotted line) and 10.0 (solid line) erg cm^{-2} s^{-1}. Right panel: The three different ratios are 10^{-4} (dashed line), 10^{-3} (dotted line) and 10^{-2} (solid line).

temperature and volume density that are needed to get three different 3/14 μm flux ratios 10^{-2}, 10^{-3} and 10^{-4}. There is no difference in this curve between the different HCN column densities 10^{13} and 10^{15} cm^{-2}.

As can be seen the observed flux ratio of $2.5 \cdot 10^{-2}$ can only be reached with a minimum volume density of $5.0 \cdot 10^{12}$ cm^{-3} at temperatures >900 K if no radiative pumping is included. However, at a temperature of 900 K, which is also close to what is estimated for three different T Tauri stars using a LTE slab model for HCN (Mandell et al. 2012), the emission would originate in a region with a volume density of around 10^{13} - 10^{14} cm^{-3} according to Fig. 4.5. These high densities are only reached below the limit where the 3 and 14 μm continuum emission becomes optically thick. Based on Fig. 4.2, the HCN emission is expected to arise in a region with densities of 10^{8} – 10^{12} cm^{-3}. Hence, including non-LTE without radiative pumping cannot re-produce the observed flux ratio. Therefore an infrared radiation field is included in the non-LTE slab model to see if this may be able to explain the observed flux ratio.

Including the radiation field leads to higher line fluxes. The radiation field will dominate over collisions when

$$\frac{n_{crit}}{n} \frac{W}{\exp[h\nu/kT_R] - 1} >> 1 \tag{4.3}$$

where T_R is the temperature of the radiation field (1000 K in our case). This happens when the volume density is much lower than the critical density or when $h\nu/kT_R$ <<1. When the radiation field dominates, the line fluxes scale with the dilution factor times the Planck function at the excitation (=radiation) temper-

ature. As a result, at low densities and temperatures, the calculated line flux is much higher than expected from a pure collisional model (Fig. 4.5). At densities above the critical density, the 'collisional' results are recovered. Again, the effects are larger at shorter than at longer wavelengths because of the higher critical densities for the 3 μm lines. This explains why the flux ratio is higher at the lower volume densities and temperatures, since this is the region where the radiation field dominates over the collisions and the excitation temperature is close to the radiation temperature.

The green line in Fig. 4.5 indicates the observed 3/14 μm flux ratio. It is seen that the models including radiative pumping at a dilution factor of 0.2 now reproduce the observed flux ratio (within a factor of a few) over a very wide range of densities and temperatures, including the range of densities of $10^8 - 10^{12}$ cm^{-3} appropriate for the upper disk layers from which the HCN emission is thought to originate. For the smaller dilution factor of 0.02, the flux ratio drops somewhat below the observed value in the relevant density range, but still provides a closer match to the observational data than the model without a radiation field. That the flux ratio is getting closer to the observed flux ratio over a wide range of densities when including an infrared radiation field demonstrates that infrared radiative pumping may play an important role when exciting the HCN molecules in the inner region of a protoplanetary disk atmosphere.

Note that the flux ratio is not sensitive to the HCN column density: only the absolute fluxes can give estimates of the HCN column density and thus its abundance.

4.5 Summary and conclusions

The excitation processes leading to the observed HCN emission from circumstellar disks around T Tauri stars have been studied to investigate which type of slab or disk model can best describe the observations that have been made so far. This work shows that the 3 μm HCN emission is not well described with a LTE slab or disk model and that these type of models will overestimate the flux of the lines, hence underestimate the abundance of HCN. As an example, judging from Fig. 4.5, assuming LTE, the line fluxes are overestimated by about an order of a magnitude at a temperature of 900 K and a volume density of 10^{12} cm^{-3} if no radiative pumping is included. Hence, the derived column density (eg., the HCN abundance) would be underestimated by about an order of magnitude. For lower densities, the effect would be proportionally larger. This is because the critical density for the 3 μm emission is much higher than the density of the inner (<0.2 AU) regions of the upper parts of the disks from which the emission is thought to arise. LTE is a better approximation for the 14 μm HCN emission due to its lower critical density. Non-LTE models are better at describing the observed 3 μm emission if infrared radiative pumping is included in the models.

These results can be compared to the work done on H_2O emission originating

from the same region in protoplanetary disks by Meijerink et al. (2009). They show that also water emission coming from <0.2 AU is not well modeled using LTE slab or disk models. The water emission lines are also better described when including non-LTE excitation in their disk model. They in addition show that the higher vibrational band lines are even more sensitive to non-LTE effects. Mandell et al. (2012) illustrate that the line fluxes of the higher ro-vibrational band $v = 2$–1 of HCN is overestimated in their LTE disk model compared with the observed upper limits. This can be explained by the fact that the higher ro-vibrational line fluxes, as for HCN nu_3 and the H_2O lines, are lowered when introducing non-LTE in the models. Future work investigating the impact on the higher ro-vibrational lines when including non-LTE and radiative pumping in a full disk model would therefore be interesting.

Acknowledgements

The authors are grateful to Kees Dullemond for providing the RADMC code and Klaus Pontoppidan for making his RADLite code available. JEB is supported by grant 614.000.605 from Netherlands Organization of Scientific Research (NWO). EvD acknowledges support from a NWO Spinoza Grant and from Netherlands Research School for Astronomy (NOVA).

V

Exploring organic chemistry in planet-forming zones[1]

Context. Over the last few years, the chemistry of molecules other than CO in the planet-forming zones of disks is starting to be explored with Spitzer and high-resolution ground-based data. However, these studies have focused only on a few simple molecules.
Aim. The aim of this study is to put observational constraints on the presence of more complex organic and sulfur-bearing molecules predicted to be abundant in chemical models of disks.
Methods. High S/N Spitzer spectra at 10–30 μm of the near edge-on disks IRS 46 and GV Tau are used to search for mid-infrared absorption bands of various molecules. These disks are good laboratories because absorption studies do not suffer from low line/continuum ratios that plague emission data. Simple LTE slab models are used to infer column densities and excitation temperatures for detected lines and upper limits for non-detections.
Results. Mid-infrared bands of HCN, C_2H_2 and CO_2 are clearly detected toward both sources. As found previously for IRS 46 by Lahuis et al. (2006), the HCN and C_2H_2 absorption arises in warm gas with excitation temperatures of 400–700 K, whereas the CO_2 absorption originates in cooler gas of ~250 K. Absolute column densities and their ratios are comparable for the two sources. No other absorption features are detected at the 3σ level. Column density limits of the majority of molecules predicted to be abundant in the inner disk — C_2H_4, C_2H_6, C_6H_6, C_3H_4, C_4H_2, CH_3, HNC, HC_3N, CH_3CN, NH_3 and SO_2—are determined. Simulations are also performed for future higher spectral resolution instruments such as on

[1]Based on: J.E. Bast, F. Lahuis, E.F Dishoeck and A.G.G.M. Tielens, 2012, submitted to A&A.

JWST, SOFIA, SPICA or ELTs.
Conclusions. The inferred abundance ratios and limits with respect to C_2H_2 and HCN are roughly consistent with models of the chemistry in high temperature gas. Models of UV irradiated disk surfaces generally agree better with the data than pure X-ray models. The limit on NH_3/HCN implies that evaporation of NH_3-containing ices is only a minor contributor. The inferred abundances and their limits also compare well with those found in comets, suggesting that part of the cometary material derives from warm inner disk gas. Future higher resolution data will provide up to an order of magnitude deeper tests of the models.

5.1 Introduction

The chemical composition of the gas in the inner regions of circumstellar disks plays an important role in determining the eventual composition of the comets and atmospheres of any planets that may form from that gas (see reviews by Prinn 1993, Ehrenfreund & Charnley 2000, Markwick & Charnley 2004, Bergin 2009). In the last few years, observations with the *Spitzer Space Telescope* have revealed a rich chemistry in the inner few AU of disks around low-mass stars, containing high abundances of HCN, C_2H_2, CO_2, H_2O and OH (Lahuis et al. 2006, Carr & Najita 2008, Salyk et al. 2008, Pascucci et al. 2009, Carr & Najita 2011, Kruger et al. 2011, Najita et al. 2010, Pontoppidan et al. 2010, Salyk et al. 2011). Spectrally and spatially resolved data of CO using ground-based infrared telescopes at 4.7 μm show that the warm molecular gas is indeed associated with the disk (e.g., Najita et al. 2003, Brittain et al. 2003, 2007, 2009, Blake & Boogert 2004, Pontoppidan et al. 2008, Salyk et al. 2011b, Brown et al. subm.), with in some cases an additional contribution from a disk wind (Bast et al. 2011, Pontoppidan et al. 2011). Spectrally resolved ground-based observations have also been obtained of OH and H_2O at 3 μm (Carr et al. 2004, Mandell et al. 2008, Salyk et al. 2008, Fedele et al. 2011), and most recently of HCN and C_2H_2 (Gibb et al. 2007, Doppmann et al. 2008, Mandell et al. 2012). All of these data testify to the presence of an active high-temperature chemistry in the upper layers of disks that drives the formation of OH, H_2O and small organic molecules. However, it is currently not known whether this gas contains more complex organic molecules which may eventually become part of exoplanetary atmospheres.

Observations of large interstellar molecules are usually carried out using (sub-)millimeter telescopes. A wide variety of complex organic species have been found in low- and high-mass protostars at the stage when the source is still embedded in a dense envelope (see Herbst & van Dishoeck 2009,for review). For disks, the pure rotational lines of CO, H_2O, HCO^+, H_2CO, HCN, N_2H^+, CN, C_2H, SO, DCO^+ and DCN have been reported but more complex molecules have not yet been detected (e.g., Dutrey et al. 1997, Kastner et al. 1997, Thi et al. 2004, Fuente et al. 2010, Henning et al. 2010, Öberg et al. 2011, Hogerheijde et al. 2011). Although these millimeter data have the advantage that they do not suffer from dust extinction and can thus probe down to the midplane, current facilities are only sensitive to the cooler gas in the outer disk (> 50AU). Even the Atacama Large Millimeter/submillimeter Array (ALMA) with its much improved spatial resolution and sensitivity can only readily image molecules at ∼5 AU or larger in the nearest disks. Moreover, ALMA cannot detect molecules without a permanent dipole moment such as C_2H_2 and CH_4, which are among the most abundant species in the inner disk. Results so far show that there is no clear correlation between the chemistry in the inner and outer parts of the disk (Öberg et al. 2011). The chemistry in the inner regions seems to be sensitive to different shapes of radiation fields and the accretion luminosities (Pascucci et al. 2009, Pontoppidan et al. 2010), but these

quantities do not seem to have an impact on the chemical composition of the colder gas further out in the disk.

Searches for more complex molecules in the inner few AU must therefore rely on infrared techniques. However, the strong mid-infrared continuum implies very low line/continuum ratios for emission lines, even at high spectral resolution. Indeed, the recent VLT-CRIRES ($R = \lambda/\Delta\lambda = 10^5$) searches in the 3 μm atmospheric window show that lines of molecules other than CO have line/continuum ratios of typically only a few %, and that even relatively simple species like CH_4 are not detected at the ~1% level (Mandell et al. 2012). On the other hand, absorption lines offer a much better chance of detecting minor species for a variety of reasons. First, absorption occurs from the ground vibrational level where the bulk of the population resides, so that the signal is much less sensitive to temperature. Another advantage is that absorption lines are relative in strength to the continuum whereas emission lines are absolute. So the strength of the absorption lines relative to the continuum will stay the same in sources which have a stronger continuum whereas the emission lines will be dominated by the continuum. Both these advantages imply that absorption lines are easier to detect for less abundant molecular species than emission lines.

Detection of absorption lines requires, however, a special orientation of the disk close to edge-on, so that the line of sight to the continuum passes through the inner disk. Only a few disks have so far been found with such a favorable geometry: that around Oph-IRS46 (Lahuis et al. 2006), GV Tau N (Gibb et al. 2007, Doppmann et al. 2008) and DG Tau B (Kruger et al. 2011). In all cases, the mid-infrared absorption bands of HCN, C_2H_2 and CO_2 have depths of 5–15%, even at the low spectral resolution $R \approx 600$ of *Spitzer*. For high $S/N > 100$ spectra, detection of absorption features of order 1% should be feasible, providing a dynamic range of up to an order of magnitude in abundances to search for other molecules. With increased spectral resolution and sensitivity offered by future mid-infrared instruments such JWST-MIRI ($R \approx 3000$), and SOFIA, SPICA and ELTs ($R \geq 50000$), another order of dynamic range will be opened up.

A large variety of increasingly sophisticated physico-chemical models of the inner regions of disks exist (e.g., Willacy et al. 1998, Aikawa et al. 1999, Markwick et al. 2002, Nomura et al. 2007, Agúndez et al. 2008, Gorti & Hollenbach 2008, Glassgold et al. 2009, Nomura et al. 2009, Willacy & Woods 2009, Woitke et al. 2009, Kamp et al. 2010, Walsh et al. 2010, Aresu et al. 2011, Gorti et al. 2011, Heinzeller et al. 2011, Najita et al. 2011, Vasyunin et al. 2011, Walsh et al. 2012). The models differ in their treatments of radiation fields (UV and/or X-rays), the gas heating and resulting disk structure, dynamical processes such as accretion flows and disk winds, grain properties and chemical networks (e.g., grain opacities, treatment of gas-grain chemistry including H_2 formation at high temperature). Some models consider only the simplest molecules in the chemistry, others have a large chemical network but publish primarily results for species that can be observed at millimeter wavelengths. Only Markwick et al. (2002) list the most abundant species, including complex molecules that do not have a dipole moment, at 1, 5 and 10 AU as

obtained from vertically integrated column densities. Since infrared observations probe only part of the disk down to where the continuum becomes optically thick, these models may not be representative of the surface layers. Column densities appropriate for comparison with infrared data have been presented by Agúndez et al. (2008), Najita et al. (2011) but do not provide data for more complex molecules. Woods & Willacy (2007) and Kress et al. (2010) consider PAH processing in the inner disk and study its impact on the abundances of related species like benzene and C_2H_2. Note that PAHs are generally not detected in disks around T Tauri stars, including the two disks studied here, at levels a factor of 10–100 lower than found in the interstellar medium (Geers et al. 2006, Oliveira et al. 2010).

Observations of molecules in comets provide another interesting data set for comparison with protoplanetary disks. Solar system comets were likely formed at distances of about 5–30 AU in the protosolar nebula. Many volatile molecules are now routinely observed in cometary atmospheres at infrared and millimeter wavelengths, including species as complex as C_2H_6, CH_3OH, and even $(CH_2OH)_2$ (see Mumma & Charnley 2011, Bockelée-Morvan 2011,for reviews). It is still debated whether the abundances measured in comets directly reflect those found in the dense envelopes around protostars or whether they result from processing and mixing material from the inner and outer disk into the comet-forming zone. Putting constraints on the inner disks abundances of these molecules will be important to probe the evolution of material from the natal protosolar nebula to the formation of icy bodies.

In this study we use the existing high S/N *Spitzer* spectra of IRS 46 and GV Tau to, for the first time, put upper limits on various molecules in the inner disk: HNC, CH_3, C_2H_4, C_2H_6, C_3H_4, HC_3N, C_6H_6, NH_3, C_4H_2, CH_3CN, H_2S and SO_2. These molecules were selected to include most of the top 15 highest vertical column density molecules at 1 and 5 AU by Markwick et al. (2002). The selected species can in principle directly test the predictions of models of inner disk chemistry. The list also contains several molecules observed in cometary atmospheres and two more molecules with a permanent dipole moment, HNC and HC_3N, which together with HCN can be observed at both infrared and millimeter wavelengths and can thus be used to connect the inner and outer disk chemistries through ALMA imaging.

The mid-infrared spectra of IRS 46 and GV Tau contain detections of C_2H_2, CO_2 and HCN which are analyzed here in terms of column densities and abundances, following the same strategy as for IRS 46 in Lahuis et al. (2007). The earlier detections of HCN and C_2H_2 toward GV Tau were performed in the 3 μm window with higher spectral resolution (Gibb et al. 2007).

A description of the observations and the reduction of the data for IRS 46 and GV Tau is presented in Section 5.2 together with some information about these two protoplanetary disks. Section 5.3.1 presents an overview of the observed and modeled spectra, whereas 5.3.2 uses a synthetic local thermodynamic equilibrium (LTE) model to estimate column densities and excitation temperatures for HCN, C_2H_2 and CO_2 toward GV Tau and compares the results with those for IRS 46.

Section 5.3.3 presents the upper limits for the various molecules toward the two sources and Section 5.3.4 shows how future instruments can provide more stringent limits. Discussion and comparison to chemical models is performed in Section 5.4. A summary of the main conclusions is found in Section 5.5.

5.2 Observations

5.2.1 IRS 46 and GV Tau

The observations of IRS 46 and GV Tau were made using *Spitzer*-IRS in both the Short-High (SH; $9.9 - 19.6\,\mu$m) and Long-High (LH; $18.7 - 37.2\,\mu$m) modes with a spectral resolving power of $R = \lambda/\delta\lambda = 600$.

Oph-IRS 46 was observed at $\alpha = 16^h27^m29^s.4$ and $\delta = -24^o39'16''.3$ (J2000), located in the Ophiuchus molecular cloud at a distance of around 120 pc (Loinard et al. 2008). IRS 46 was initially observed in 2004 as part of the Cores to Disks *Spitzer* legacy program (Evans et al. 2003) and in 2008 and 2009 at multiple epochs to search for variability. Its mid-infrared spectral energy distribution rises strongly with wavelength, as expected for a near edge-on disk (Crapsi et al. 2008). Strong HCN, C_2H_2 and CO_2 absorption has been detected with *Spitzer* and attributed to arise from warm gas in the surface layers of the inner few AU of the disk, seen in absorption against the continuum produced by the hot inner rim on the near and far side of the star (Lahuis et al. 2006). Lahuis et al. (2011,and in prep.) show that hot water emission lines are also detected. More interestingly, strong variation in the depth of the molecular absorption bands as well as in the strength of the water emission lines and the mid-IR contiuum is observed on timescales of a few years. The data used here are the original observations obtained on August 29, 2004 as part of AOR# 0009829888 and published by Lahuis et al. (2006). These show the deepest molecular absorptions, thus providing the best upper limits of column densities of other species relative to the observed C_2H_2, HCN and CO_2 column densities.

GV Tau is a T Tauri star that is partly embedded in the L1524 molecular cloud. Its observations were positioned at $\alpha = 4^h29^m25^s.8$ and $\delta = +24^o33'00''5$ (J2000). It has an infrared companion about $1.2''$ to the north. The companion is named GV Tau N and the primary optical source is called GV Tau S. Gibb et al. (2007) detected HCN and C_2H_2 toward GV Tau N using Keck-NIRSPEC at L-band, however, no such detections were made toward GV Tau S. GV Tau has subsequently been observed using the IRS SH mode at multiple epochs with *Spitzer* in a GO4 program (PI, F.Lahuis; program ID 50532). For the SH part of the spectrum the GO4 data (AOR # 0022351616, 0028247808, 0028247552 and 0031618304) were used. For the LH part, data from the *Spitzer* GTO program observed on 02 March 2004 as part of AOR # 0003531008 were adopted. Note that the *Spitzer*-IRS aperture does not resolve the GV Tau binary, in contrast to NIRSPEC. The *Spitzer* spectra therefore combine emission and absorption of GV Tau N and GV Tau S.

Both GV Tau N and GV Tau S are variable at 2 μm (Leinert et al. 2001, Koresko et al. 1999) and at 8 – 13 μm (Przygodda 2004, Roccatagliata et al. 2011). This variability has been attributed to variable accretion mechanisms for GV Tau N and variation in the extinction due to inhomogeneities in the circumstellar material for GV Tau S (Leinert et al. 2001). However, the multi-epoch *Spitzer* data do not show significant mid-infrared variation on timescales of a few months up to a few years, in contrast with IRS 46. The continuum of GV Tau N is about an order of magnitude brighter than the continuum of GV Tau S between $8 - 13$ μm (Przygodda 2004, Roccatagliata et al. 2011). The factor changes between $5 - 10$ due to variations in the continuum emission from both the northern and southern source. Since no absorption was seen in GV Tau S in Gibb et al. (2007), Doppmann et al. (2008) it is assumed that the majority of the absorption arises toward GV Tau N. However, the continuum emission from the southern source captured in the *Spitzer*-IRS aperture slightly reduces the total optical depth of the absorption lines in the spectrum. To put an upper limit on the added uncertainty caused by the additional continuum emission from GV Tau S, it is assumed that the mid-IR continuum of GV Tau N is at least 5 times stronger than that of GV Tau S, resulting in an additional uncertainty of $\sim 1 - 4\,\%$ for features that are $\sim 5 - 20\,\%$ deep. Since the effect is minor, no correction is made for the column densities derived here.

5.2.2 Data reduction

The data reduction started with the BCD (Basic Calibrated Data) images from the *Spitzer* archive processed through S18 pipeline. The BCD images were then processed using the Cores to Disks (c2d) analysis pipeline (Lahuis et al. 2006b, Kessler-Silacci et al. 2006). The main processing steps are background correction, bad-pixel removal, spectral extraction, defringing, order matching and spectral averaging. Two extraction methods were used; 1) a full aperture extraction from the BCD images and 2) an optimal extraction using an analytical psf (Lahuis et al. 2007) defined using a set of high S/N calibration stars. For both extractions a relative spectral response function (RSRF) calibration is applied with ξ Dra as the main reference star using MARCS models taken from the *Spitzer* science center (Decin et al. 2004).

For all observations the extraction method giving the best S/N was used to produce the final spectra. The two (partly) independent extraction methods further allow to better discriminate between artifacts and true science features.

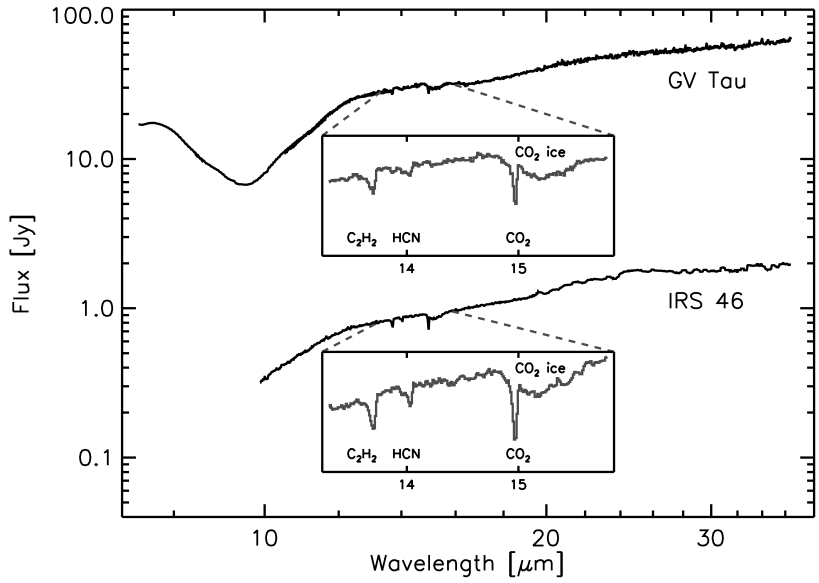

Figure 5.1 Spectra of the protoplanetary disks around IRS 46 and GV Tau taken with the *Spitzer*-IRS.

5.3 Results

5.3.1 Spectra

Figure 5.1 shows the spectra of IRS 46 and GV Tau over the $10 - 37\,\mu$m region. The absorption bands of gaseous C_2H_2 ν_5, HCN ν_2 and CO_2 ν_2 can be clearly seen at 13.7, 14.0 and 15.0 μm, together with the solid CO_2 feature at $15 - 16\,\mu$m. To search for other molecules, a local continuum has been fitted to the broad spectral features and divided out. The S/N on the continuum is typically 100 or better. No other obvious absorption features are detected at the few % absorption level. The model spectra with derived column densities and upper limits are described below.

5.3.2 C_2H_2, HCN and CO_2

To extract quantitative information from the spectra, a simple local thermodynamical equilibrium (LTE) absorption slab model has been used to fit the data. The free parameters in the model are the excitation temperature, the integrated column density along the line of sight and the intrinsic line width, characterized by

the Doppler b-value. The excitation temperature sets the level populations of the molecule using the Boltzmann distribution. The lack of collisional rate coefficients for many of the species considered here prevents non-LTE analyses. The model spectrum is convolved with the spectral resolution of the instrument and resampled to the observed spectra. More details about the model and the molecular parameters and data that are used for the three detected molecules can be found in Lahuis & van Dishoeck (2000), Lahuis et al. (2007), Boonman et al. (2003) and in Table 1.

Table 5.1 Basic molecular data

Molecule	Formula	Band	$\tilde{\nu}$[a]	S_{lit}[a]	S_{int}[b]	Source[c]
			[cm^{-1}]	[$atm^{-1}\,cm^{-2}$]	[$atm^{-1}\,cm^{-2}$]	
Acetylene	C_2H_2	ν_5 CH bending	729.1	630	816	H08
Carbon Dioxide	CO_2	ν_2 bending	667.4	200	249	H08
Hydrogen Cyanide	HCN	ν_2 bending	713.5	257	286	H08
Hydrogen Isocyanide	HNC	ν_2 bending	464.2	1570	798	G09
Methyl Radical	CH_3	ν_2 out-of-plane bending	606.5	611	616	FPH
Ethylene	C_2H_4	ν_7 CH2 waggling	949.2	324	320	G09
Ammonia	NH_3	ν_2 symmetric bendng	950.0	568	614	H08
Sulphur Dioxide	SO_2	ν_2 bending	517.6	113	97	G09
Ethane	C_2H_6	ν_9 CH3 rocking	822.0	36	29	H08
Diacetylene / Butadiyne	C_4H_2	ν_8 CH bending	627.9	437	229	G09
Benzene	C_6H_6	ν_4 CH bending	673.5	250	212	G09
Propyne / Methyl Acetylene	C_3H_4	ν_9 CH bending	638.6	360	201	G09
Cyanoacetylene / Propynenitrile	HC_3N	ν_5	663.4	278	94	G09
Methyl Cyanide / Acetonitrile	CH_3CN	ν_4 CC stretch	920.3	6	3	G09

[a]Central wavenumber of band and band strengths from *Constants for molecules of astropysical interest in the gas phase* by J. Crovisier
http://wwwusr.obspm.fr/~crovisie/basemole/

[b]Band strength of the simulated spectra. $S = N_L \times \int \tau(\nu)\delta\nu \,/\, n$, (see App. A.1 Helmich 1996). Calculations were performed for $T = 298\,\mathrm{K}$, $b = 20\,\mathrm{km\,s^{-1}}$ and $n = 1 \cdot 10^{15}\,\mathrm{cm^{-2}}$ at a resolution of 3000 to keep all bands far from saturation

[c]H08: HITRAN 2008 (Rothman et al. 2009), G09: GEISA 2009 (Jacquinet-Husson et al. 2011) and FPH: Helmich (1996)

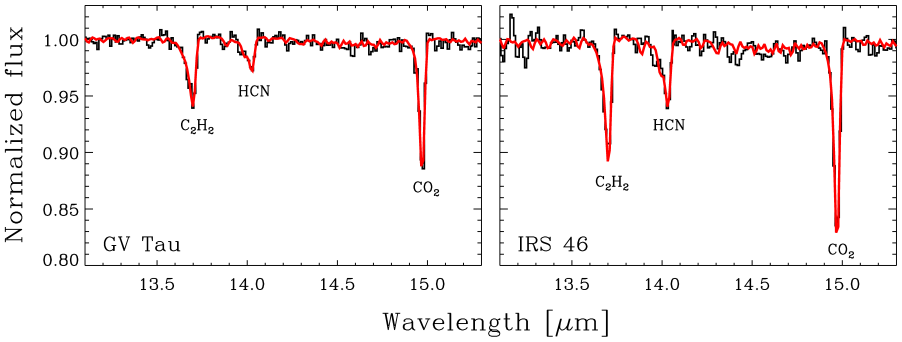

Figure 5.2 Continuum normalized spectra of GV Tau and IRS 46. Plotted in black are the observed spectra and overplotted in red the best-fit synthetic spectra to the absorption bands of C_2H_2 ν_5=1–0, HCN ν_2=1–0 and CO_2 ν_2=1–0. See Table 5.2 for best fit model parameters.

Figure 5.2 presents a blow-up of the $13-15\,\mu$m range of the GV Tau and IRS 46 spectra with the continuum divided out. Included are the best-fitting model spectra. The figure clearly shows that the *P*- and *R*-branch lines are difficult to detect at the *Spitzer*-IRS spectral resolution of $R = 600$, however the *Q*-branches of C_2H_2, HCN and CO_2 are easily seen. In addition the *Q*-branch changes its form and depth with excitation temperature and column density. In particular, the depth of the *Q*-branch decreases with increased excitation temperature for the same total column density and broadens to the blue side due to an increase in the population of the higher rotational levels. A higher column density on the other hand increases the central depth of the *Q*-branch since more molecules absorb photons. As can be seen in Lahuis & van Dishoeck (2000) the *Q*-branch is sensitive to the adopted Doppler *b*-value with the magnitude of the effect depending on the temperature and column density. The C_2H_2 lines become more easily optically thick than those of the other molecules at lower temperatures so care should be taken. Spectrally resolved data obtained with Keck-NIRSPEC (Salyk et al. 2011b, Lahuis et al. 2006) and within our VLT-CRIRES survey (Pontoppidan et al. 2011b, Brown et al. subm.) show that the HCN and CO lines have $b \approx 12$ km s^{-1}. In our analysis we therefore adopt a Doppler *b*-value of 10 km s^{-1}. This means that at typical temperatures of ~400 K saturation plays a role for column densities above 4 and 15×10^{16} cm^{-2} for C_2H_2 and HCN, respectively. For CO_2 the saturation limit is significantly higher.

A grid of synthetic spectra of C_2H_2, HCN and CO_2 was made for a range of column densities and temperatures and fitted to the data obtained for GV Tau. The best fit as presented in Fig. 5.2 was determined by finding the minimum difference between data and model as measured by the χ^2 values. The derived column

Table 5.2 Results from molecular fits to GV Tau and IRS 46 absorption features

	Temperature [K]		Column density [10^{16} cm^{-2}]	
Source	IRS 46	GV Tau	IRS 46	GV Tau
C_2H_2	$490 \pm ^{50}_{30}$	$720 \pm ^{60}_{40}$	2.1 ± 0.4	1.4 ± 0.3
HCN	$420 \pm ^{40}_{25}$	$440 \pm ^{40}_{30}$	3.7 ± 0.8	1.8 ± 0.4
CO_2	$250 \pm ^{25}_{15}$	$250 \pm ^{25}_{15}$	8.4 ± 1.1	5.1 ± 0.7

densities and excitation temperatures for the different molecules are summarized in Table 5.2. For IRS 46, the values are consistent with those of Lahuis et al. (2006) within the error bars. It is seen that the temperatures of the different molecules and their column density ratios are comparable between GV Tau and IRS 46. This supports the hypotheses that both sources are inclined disks with similar characteristics. In both sources CO_2 has the highest column density but the lowest temperature, whereas the HCN/C_2H_2 ratio is slightly above unity. In their 2 – 5 μm study, Gibb et al. (2007) however find significantly lower temperatures for C_2H_2 (170 ± 20 K) and HCN (115 ± 20 K) compared to our estimated temperatures of about 400 to 700 K. However in later Keck-NIRSPEC L-band observations, Doppmann et al. (2008), Gibb & Troutman (2011) detect lines out to much higher J values, indicating warmer gas around 500 K. Our mid-infrared results are therefore not inconsistent with the near-IR data.

The high resolution near-IR data for IRS 46 and GV Tau N show that the spectral lines are shifted in velocity. For IRS46, CO and HCN are blueshifted by about 24 km s^{-1} with respect to the cloud (Lahuis et al. 2006) whereas for GV Tau the HCN lines are redshifted by about 13 km s^{-1} compared with the star (Doppmann et al. 2008). This could indicate that the observed HCN, C_2H_2 and CO_2 absorption originates in a disk wind or infalling envelope rather than the disk itself. However, the high densities needed to excite these higher J-transitions as well as the constraints on the size of the high abundance region (<11 AU) imply that the absorption lines have an origin in outflowing or infalling gas that must be very closely related to the disk itself with a chemistry similar to that of the disk. This is further discussed in Lahuis et al. (2006), Gibb et al. (2007), Doppmann et al. (2008), Kruger et al. (2011) and Mandell et al. (2012). Fuente et al. (2012) recently imaged the warm HCN associated with the disk of GV Tau N at millimeter wavelengths and found an emitting radius of less than 12 AU.

Figures 10, 11 and 12 in the Appendix present C_2H_2, HCN and CO_2 absorption spectra at higher spectral resolution for $R \approx 3000$, as appropriate for the JWST-MIRI instrument, and at $R \approx 50000$, as typical for future mid-infrared spectrometers on an Extremely Large Telescope (ELT) (e.g., METIS on the E-ELT, Brandl et al. 2010). The latter spectrum is also characteristic (within a factor of 2) of the spectral resolution of $R = 100000$ of EXES on SOFIA (Richter et al. 2006) or a potential high resolution spectrometer on the SPICA mission (Goicoechea &

Nakagawa 2011). As expected, the central Q branch becomes deeper with higher spectral resolution and the $P-$ and R-branches become readily detectable, allowing a more accurate model fit to the data. The inferred column density, however, should not change beyond the error bars derived from the low resolution data.

5.3.3 Other molecules

Overview

Table 5.1 summarizes the molecular data (vibrational mode, line positions, band strengths) used for all molecules for which searches have been made toward IRS 46 and GV Tau in the 10–30 μm wavelength range, together with the main references from which they have been extracted. Only the intrinsically strongest bands of each molecule have been chosen; weaker bands are ignored. Note that isotopologues and vibrationally excited states or 'hot bands' are not included in the data sets, except in the fitting of the observed spectra of HCN, CO_2 and C_2H_2. Hot bands are expected to be suppressed in full non-LTE calculations, where the excitation of the higher vibrational levels is subthermal at densities below $\approx 10^{10}$ cm^{-3}. Synthetic spectra are generated following the procedures as described in Helmich (1996), Lahuis & van Dishoeck (2000).

Our spectra use molecular data from various databases listed in Table 5.1. To assess their reliability, we have computed the integrated absorption band strengths of the simulated spectra and compared them with independent band strengths tabulated in the literature (columns 5 and 6 of Table 5.1. This table shows that the band strengths of all species agree to within factor of ~ 3 and in most cases much better. For the purpose of this paper this accuracy is sufficient and differences between databases and other literature values are not pursued here. It should be noted, however, that there are (sometimes significant) differences between line lists and not all line lists are complete.

Figure 5.3 presents an overview of the simulated LTE spectra for all molecules considered here at $T = 500$ K, $R = 50,000$ and a column density of $1{\cdot}10^{16}$ cm^{-2}. A variety of absorption patterns is seen, depending on the characteristics and symmetries of the individual bands involved. Together, they span most of the medium resolution wavelength range observed by *Spitzer*.

Upper limits from Spitzer data

To estimate the upper limits of non-detected molecules, first the rms was calculated over the region where the spectral band of the molecule of interest is expected to be. The wavelength range of this region was set to be 10 times the FWHM of the Q-branch of the molecule, except for SO_2 where the P and R-branches were taken as a reference point. The rms was then multiplied by 3 to assume a 3σ limit. The absorption LTE model was subsequently used to determine the maximum column

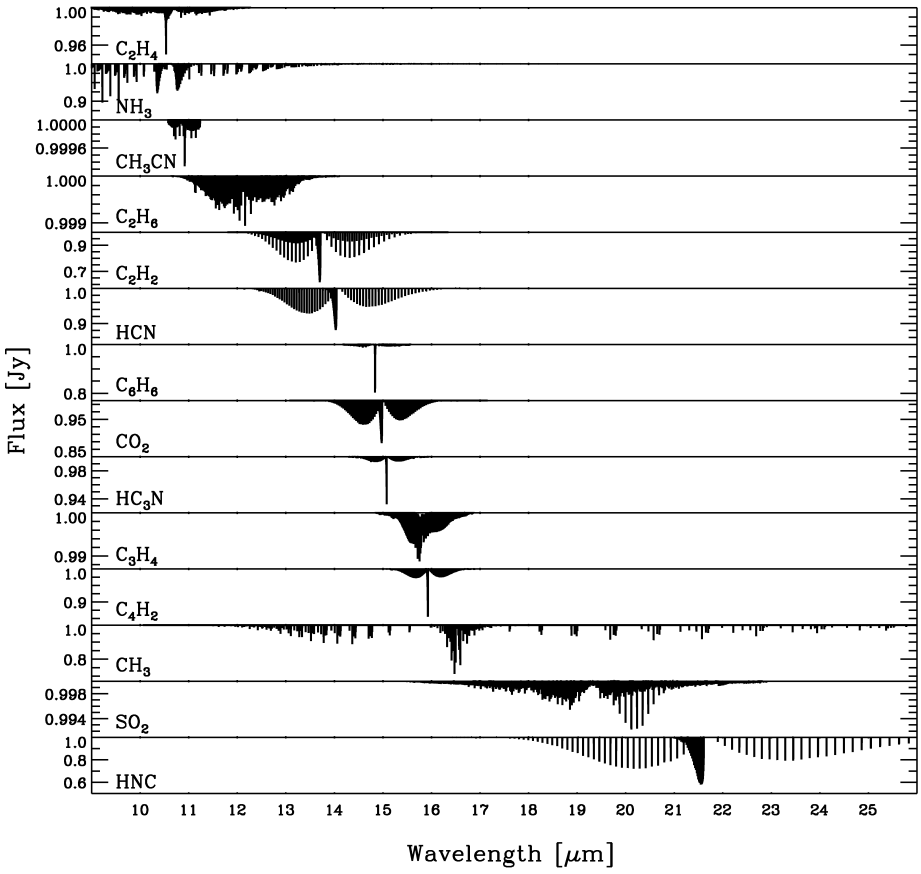

Figure 5.3 Synthetic spectra of the different molecules for T_{ex}=500 K and for a resolving power of R=50,000. The column density of each molecule is set to be $1{\cdot}10^{16}$ cm^{-2} which is the same as in Fig. 10–22

density that fits the data within the 3σ range. Three different temperatures of 200, 500 and 1000 are adopted, using $b = 5$ km s^{-1} throughout.

Plots with parts of the observed spectra for GV Tau and IRS 46 including the synthetic spectra of the different molecules set so that their Q-branch has a depth of 3σ at a temperature of 500 K are presented in Fig. 5.4 and Fig. 5.5. For reference, Figures 10 – 23 in the Appendix present an overview of the simulated LTE spectra at $R = 600$ for all the molecules considered here at additional temperatures of 200 and 1000 K.

The derived 3σ upper limits on the column densities are presented in Table 5.3 and 5.4. In addition Fig. 5.6 shows how the relative intensity in percent changes with temperature and column density for each molecule. Not all column densities follow the expected trend of a higher upper limit on the column density at a higher temperature because of a decrease in the depth of the Q-branch. This tendency can be explained when looking at the different spectra. For example, HNC follows the expected trend (Fig. 13), but not C_6H_6 (Fig. 20). The latter behavior is due to the low spectral resolving power $R = 600$ which does not resolve the intrinsically narrow $Q-$branch of this heavy molecule. At higher resolving power, however, the strength of Q-branch does in fact decrease with the temperature as expected.

Tables 5.5 and 5.6 present the upper limits on the column densities relative to C_2H_2 and HCN, respectively, for both IRS 46 and GV Tau. Abundance ratios relative to C_2H_2 and HCN are typically of order unity, except for CH_3CN and C_2H_6 which have particularly low band strengths (see Table 5.1). The most stringent ratios of <0.2–0.5 are obtained for C_4H_2 and C_6H_6. The ratios are also graphically displayed in Figures 5.7 and 5.8 where they are compared with model results. These results will be further discussed in §5.4.

5.3.4 High resolution spectra

Figures 13 – 21 present the higher resolution spectra of all molecules at R=3000 and 50,000 at $T_{ex} = 200, 500$ and 1000 K using $b = 5$ km s^{-1} and a column density of $1{\cdot}10^{16}$ cm^{-2}. The improved detectability of the molecules at higher spectral resolution is obvious. The resulting 3σ limits are included in Table 5.3 for IRS 46. For GV Tau, the limits at higher resolution scale similarly. The column density limits are lower by factors of 2–10. They do not decrease linearly with increasing resolving power, however, because the strong $Q-$branches used to set the limits are blends of many lines at low resolution which become separated at higher resolving power. In some cases (C_2H_6, CH_3CN), the gain is very small because the molecule absorbs less than 0.1% of the continuum for the adopted column density, which remains undetectable at S/N=100 even at high spectral resolution.

Tables 5.5 and 5.6 include the column density ratios with respect to C_2H_2 and HCN at higher resolving power. Since the C_2H_2 and HCN column densities remain the same, the abundance ratio limits are now up to an order of magnitude lower, thus bringing the limits in a more interesting regime where they provide more

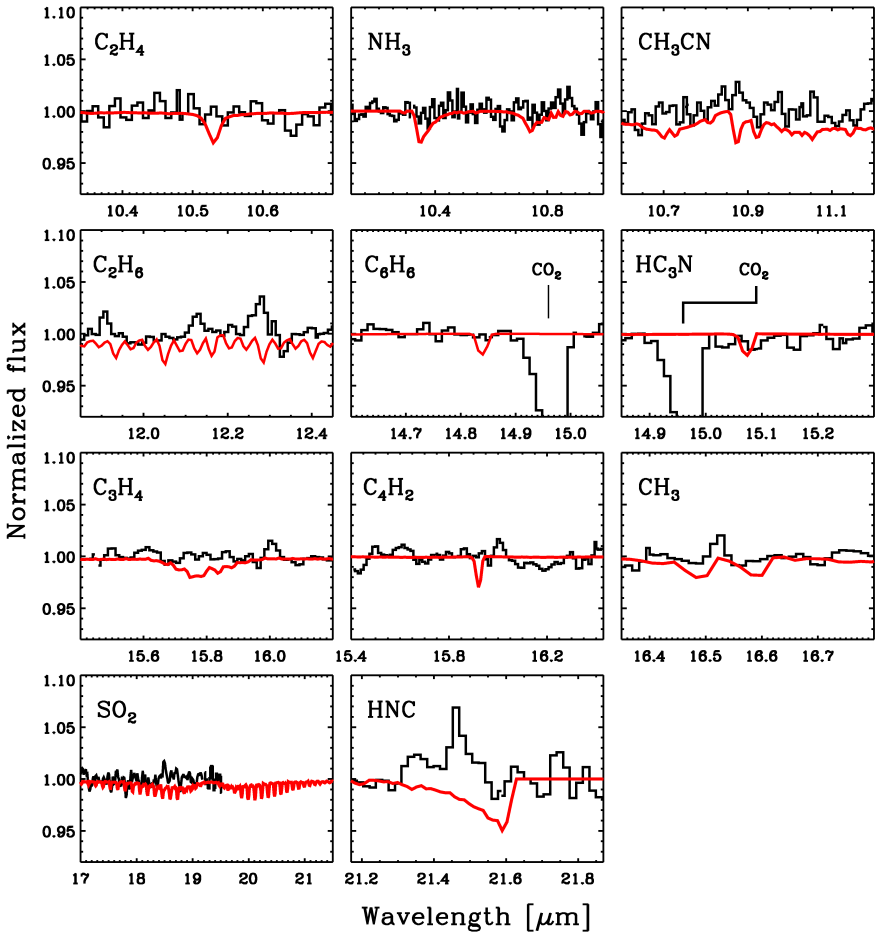

Figure 5.4 Synthetic spectra (in red) for different molecules at a 3σ maximum optical depth compared with the observed spectrum of IRS 46 (in black).

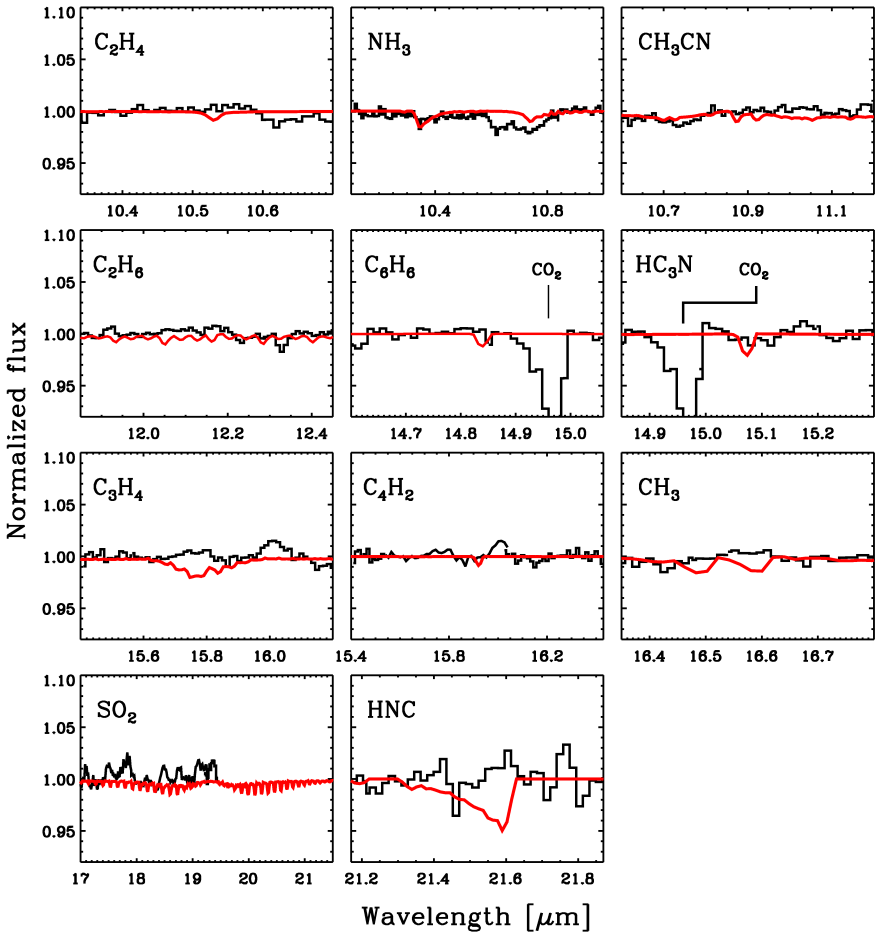

Figure 5.5 Synthetic spectra (in red) for different molecules at a 3σ maximum optical depth compared with the observed spectrum of GV Tau (in black).

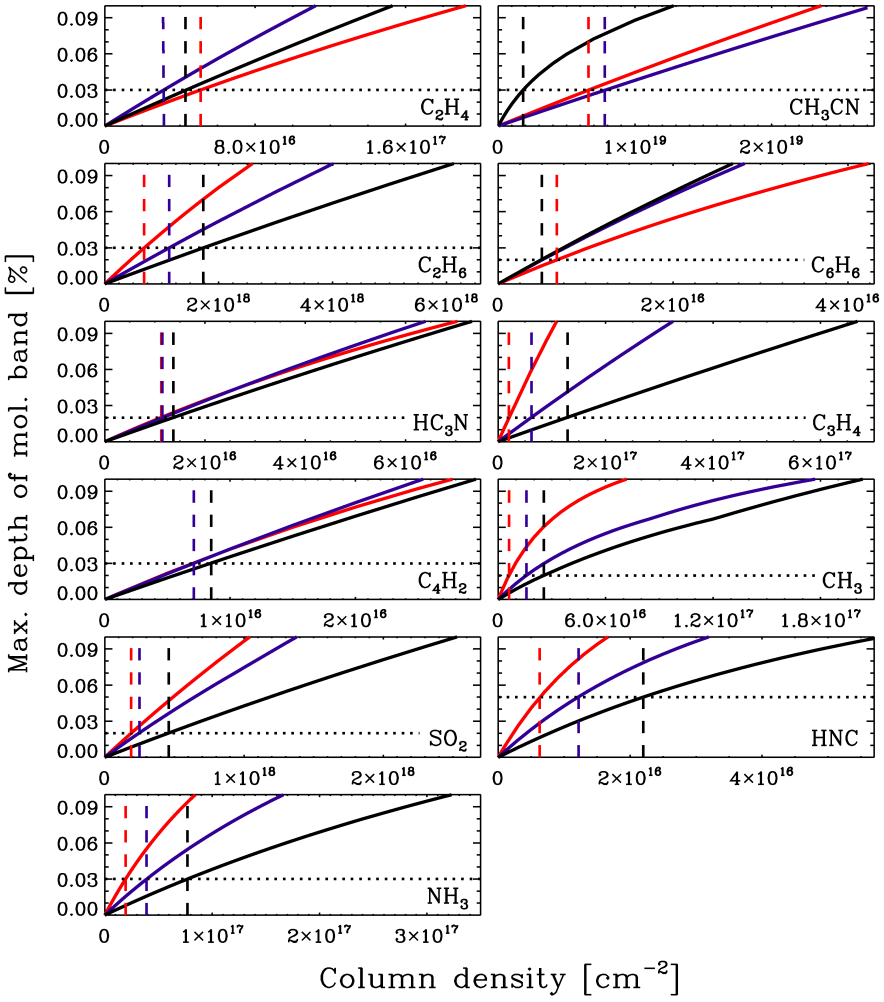

Figure 5.6 Variation of the maximum optical depth as a function of column density for different molecular bands at excitation temperatures of 200 K (red), 500 K (blue) and 1000 K (black). The 3σ observational limit for IRS 46 is marked with a black dotted line.

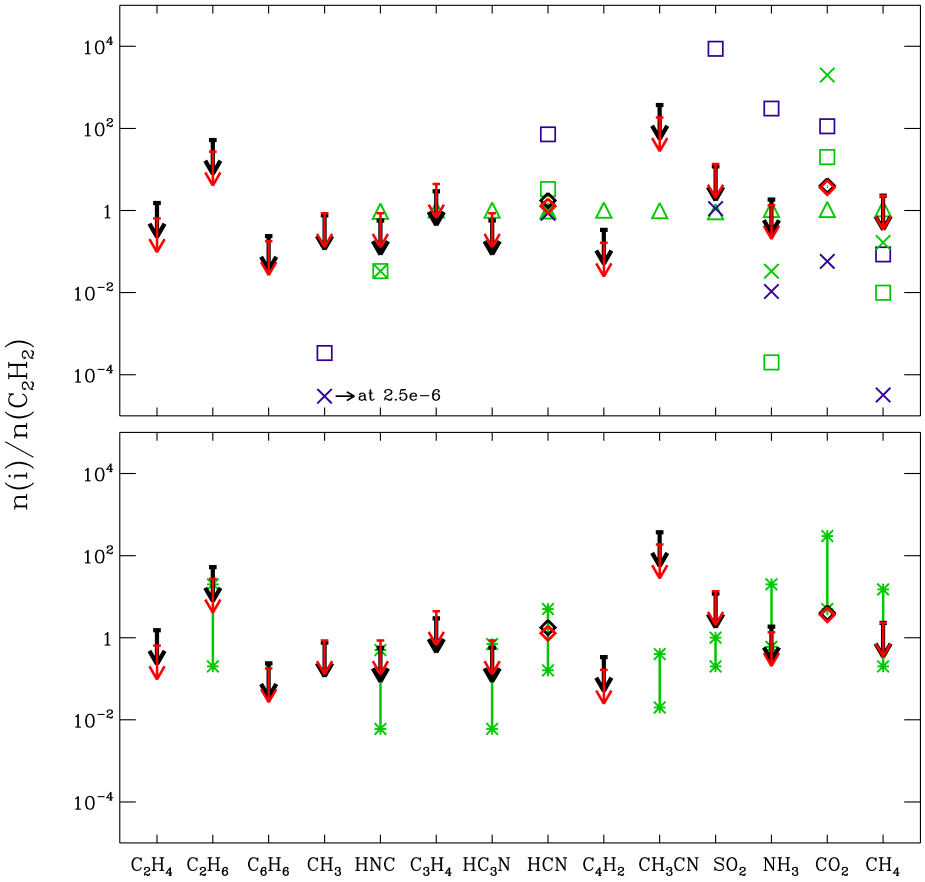

Figure 5.7 Comparison of the abundances of various species relative to C_2H_2 between inner disk observations, chemical models (upper panel) and cometary observations (lower panel). The observed upper limits for IRS 46 (black arrows) and GV Tau (red arrows) and their respective detections (black and red diamonds) are indicated. Upper panel: Abundance ratios in the disk model by Markwick et al. (2002) at 5 AU (green triangle), from the reference disk model (blue square) and for O/C = 1 (blue cross) at 1 AU by Najita et al. (2011) and from the disk model by Agúndez et al. (2008) at 1 AU (green square) and 3 AU (green cross). Lower panel: the abundance ratios detected in comets (the detection range for each molecule is indicated with 2 green stars) (Mumma & Charnley 2011).

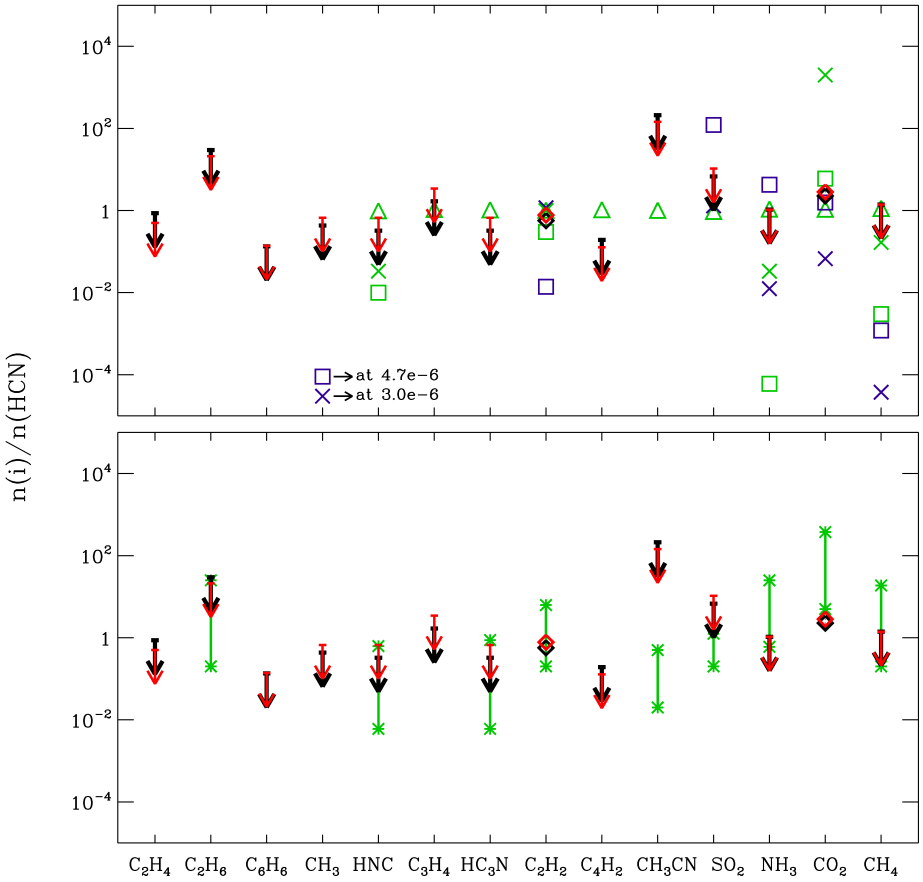

Figure 5.8 Comparison of the abundances of various species relative to HCN between inner disk observations, chemical models (upper panel) and cometary observations (lower panel). The observed upper limits for IRS 46 (black arrows) and GV Tau (red arrows) and their respective detections (black and red diamonds) are indicated. Upper panel: Abundance ratios in the disk model by Markwick et al. (2002) at 5 AU (green triangle), from the reference disk model (blue square) and for O/C = 1 (blue cross) at 1 AU by Najita et al. (2011) and from the disk model by Agúndez et al. (2008) at 1 AU (green square) and 3 AU (green cross). Lower panel: the abundance ratios detected in comets (the detection range for each molecule is indicated with 2 green stars) (Mumma & Charnley 2011).

Table 5.3 Inferred upper limits of column densities [10^{16} cm^{-2}] toward IRS 46 at different excitation temperatures and spectral resolving powers.

	C_2H_4	C_2H_6	C_6H_6	CH_3	HNC	C_3H_4
R=600, 200 K	<5.1	<69	<0.7	<0.6	<0.6	<2.0
500 K	<3.2	<110	<0.5	<1.6	<1.2	<6.2
1000 K	<4.3	<170	<0.5	<2.6	<2.2	<13
R=3000[a]	<1.8	<50	<0.2	<0.4	<0.9	<3.1
R=50,000[a]	<0.6	<29	<0.09	<0.06	<0.09	<1.8
3σ [%][b]	0.03	0.03	0.02	0.02	0.05	0.02
	HC_3N	C_4H_2	CH_3CN	SO_2	NH_3	
R=600, 200 K	<1.1	<0.7	<660	<19	<2.0	
500 K	<1.2	<0.7	<780	<25	<3.9	
1000 K	<1.4	<0.9	<180	<46	<7.7	
R = 3000	<0.4	<0.3	<310	<8.5	<1.4	
R = 50,000	<0.3	<0.2	<46	<2.6	<0.3	
3σ [%]	0.02	0.03	0.03	0.02	0.03	

[a]The upper limits at spectral resolving powers of R = 3000 and 50,000 are for a maximum of 3σ absorption at T = 500 K.

[b]The actual 3σ limit in % absorption at the location of the molecular band.

stringent tests of chemical models.

Note that these limits do not take the transmission of the Earth's atmosphere into account but assume that the strong Q-branches can be observed unobscured. For ground-based instruments, this is often not the case and detectability depends both on the transmission and on the radial velocity shifts of the sources with respect to atmospheric lines (Lacy et al. 1989).

Table 5.4 Inferred upper limits of column densities [10^{16} cm^{-2}] toward GV Tau at different excitation temperatures at a resolving power of R=600.

	C_2H_4	C_2H_6	C_6H_6	CH_3	HNC	C_3H_4
200 K	<1.2	<23	<0.3	<0.4	<0.6	<2.0
500 K	<0.9	<38	<0.3	<1.2	<1.2	<6.2
1000 K	<0.9	<57	<0.3	<1.8	<2.2	<13
3σ [%] [a]	0.010	0.010	0.010	0.015	0.050	0.020
	HC_3N	C_4H_2	CH_3CN	SO_2	NH_3	
200 K	<1.1	<0.2	<230	<14	<0.9	
500 K	<1.2	<0.2	<260	<19	<1.9	
1000 K	<1.4	<0.3	<50	<34	<3.7	
3σ [%]	0.020	0.010	0.010	0.015	0.015	

[a]The actual 3σ limit in % absorption at the location of the molecular band.

Table 5.5 Observed molecular column density ratios relative to C_2H_2 in disks compared with different chemical models and cometary observations.

Ratio rel to C_2H_2	C_2H_4	C_2H_6	C_6H_6	CH_3	HNC	C_3H_4	HC_3N	CH_4
IRS 46	<1.5	<52	<0.2	<0.8	<0.6	<3.0	<0.6	-
GV Tau	<0.6	<27	<0.2	<0.9	<0.9	<4.4	<0.9	-
DR Tau	-	-	-	-	-	-	-	<2.3[a]
$R = 3000$[b]	<0.9	<24	<0.08	<0.2	<0.4	<1.5	<0.2	-
$R = 50,000$	<0.3	<14	<0.04	<0.03	<0.04	<0.9	<0.1	-
Markwick et al. (2002) 1 AU	-	-	-	1.0	1.0	1.0	1.0	1.1
Markwick et al. (2002) 5 AU	-	-	-	-	1.0	1.0	1.0	1.1
Najita et al. (2011) ref	-	-	-	4.0E-4	-	-	-	0.09
Najita et al. (2011) O/C = 1.0	-	-	-	2.5E-6	-	-	-	3.2E-5
Agúndez et al. (2008) 1 AU	-	-	-	-	0.03	-	-	0.01
Agúndez et al. (2008) 3 AU	-	-	-	-	0.03	-	-	0.2
Mumma & Charnley (2011)	-	0.2–20	-	-	0.01–0.5	-	0.01–0.7	0.2–15

Ratio rel to C_2H_2	HCN	C_4H_2	CH_3CN	SO_2	NH_3	CO_2
IRS 46	1.8	<0.3	<370	<11.9	<1.9	4.0
GV Tau	1.3	<0.2	<190	<13.6	<1.4	3.6
DR Tau	-	-	-	-	-	-
$R = 3000$	-	<0.1	<150	<4.0	<0.7	-
$R = 50,000$	-	<0.1	<22	<1.2	<0.1	-
Markwick et al. (2002) 1 AU	1.0	1.0	1.0	0.9	1.0	1.0
Markwick et al. (2002) 5 AU	1.0	1.0	1.0	0.9	1.1	1.1
Najita et al. (2011)	70	-	-	8700	310	110
Najita et al. (2011) O/C	0.9	-	-	1.1	0.01	0.06
Agúndez et al. (2008) 1 AU	3.0	-	-	-	2.0E-4	20
Agúndez et al. (2008) 3 AU	1.0	-	-	-	0.03	2000
Mumma & Charnley (2011)	0.2–5.0	-	0.02–0.4	0.2–1.0	0.6–20	5.0–300

[a]From 3 μm emission data (Mandell et al. 2012).

[b]The R=3000 and 50,000 values refer to the 3σ limits on the abundance ratios that can be obtained toward IRS 46 if observed at higher spectral resolution.

Table 5.6 Observed molecular column density ratios relative to HCN as well as CH_3CN/NH_3 compared with chemical models and with cometary observations.

Obs/models	HNC	HC_3N	CH_3CN	NH_3	CH_3CN/NH_3
IRS 46	<0.3	<0.3	<210	<1.1	<200
GV Tau	<0.7	<0.7	<140	<1.1	<140
AS 205	-	-	-	<2.7[a]	-
$R = 3000$[b]	<0.2	<0.1	<84	<0.4	220
$R = 50,000$	<0.03	<0.08	<12	<0.08	160
Markwick et al. (2002) at 1 AU	1.0	1.0	1.0	1.0	1.0
Markwick et al. (2002) at 5 AU	1.0	1.0	1.0	1.1	0.9
Najita et al. (2011) ref	-	-	4.0	-	-
Najita et al. (2011) O/C = 1.0	-	-	0.01	-	-
Agúndez et al. (2008) 1 AU	0.01	-	-	6.0e-5	-
Agúndez et al. (2008) 3 AU	0.03	-	-	0.03	-
Mumma & Charnley (2011)	0.01–0.6	0.01–0.9	0.02–0.5	0.6–25	0.01–0.1
Garrod et al. (2008) M	-	-	-	890	7.5E-5

[a]From 3 μm emission (Mandell et al. 2012).

[b]The R=3000 and 50,000 values refer to the 3σ limits on the abundance ratios that can be obtained toward IRS 46 if observed at higher spectral resolution.

5.4 Discussion

Tables 5.5 and 5.6 and Figures 5.7 and 5.8 compare our limits with a variety of chemical models. There are two distinct routes towards molecular complexity in regions of star- and planet formation. First, at elevated temperatures such as found in the inner disks, various reactions with activation barriers open up. If atomic carbon can be liberated from CO and atomic nitrogen from N_2, high abundances of CH_4, C_2H_2 and HCN can be produced. The second route starts in the pre-stellar cores where ices are formed through grain surface reactions. At a later stage, these ices can be transported into the disk and evaporate so that a chemistry rich in hydrogenated molecules can ensue. We review each of these classes of models and then discuss our observations in the light of these models and in comparison with cometary and other data.

5.4.1 Warm chemistry

The warm gas chemistry in the photospheres of disks follows a similar chemical scheme as that in other interstellar regions with high temperature gas such as the inner envelopes of massive protostars (e.g., Doty et al. 2002, Rodgers & Charnley 2003, Stäuber et al. 2005), high density photodissociation regions (PDRs) (e.g., Sternberg & Dalgarno 1995) and shocks (e.g., Mitchell 1984, Pineau des Forêts et al. 1987, Viti et al. 2011). In fact, high abundances of C_2H_2, HCN and CO_2 were first found in gas with temperatures of several hundred K near massive protostars (Lacy et al. 1989, Evans et al. 1991, Lahuis & van Dishoeck 2000). The chemical scheme starts with separating C or C^+ from CO and N from N_2, see Fig. 5.9 (adapted from Agúndez et al. 2008). This can be done either by UV photons, cosmic rays or X-rays. A UV-dominated region will produce comparable amounts of C^+ and C, whereas cosmic rays and X-rays produce He^+ which will react with CO to produce primarily C^+.

For carbon-bearing species, the rate limiting steps of this scheme are the reactions of C and C^+ with H_2 which have activation barriers E_a of ~12,000 and 4,000 K, respectively. At temperatures of a few hundred K, the C^+ channel leads to CH_4 and C_2H_2 while at high temperatures (>800 K), the C-channel becomes active. Reactions of C_2 with H_2 have activation barriers of ~1500 K and form another route to produce C_2H and subsequently C_2H_2. For nitrogen-bearing species, the reactions of NH with H_2 (E_a ~ 7800 K) to form NH_3 and of CN with H_2 (E_a ~ 820 K) to form HCN also require high temperatures. At low temperatures < 200 K, the above reactions are closed and C^+, C and N will be driven back to CO and N_2 through reactions involving OH. Hence, the higher the temperature the more C_2H_2, CH_4 and HCN will be produced.

Similar arguments apply to the more complex hydrocarbons studied here. In fact, high temperature, high density chemistry starting with high abundances of C_2H_2 and HCN resembles the chemistry of the atmospheres of carbon-rich evolved

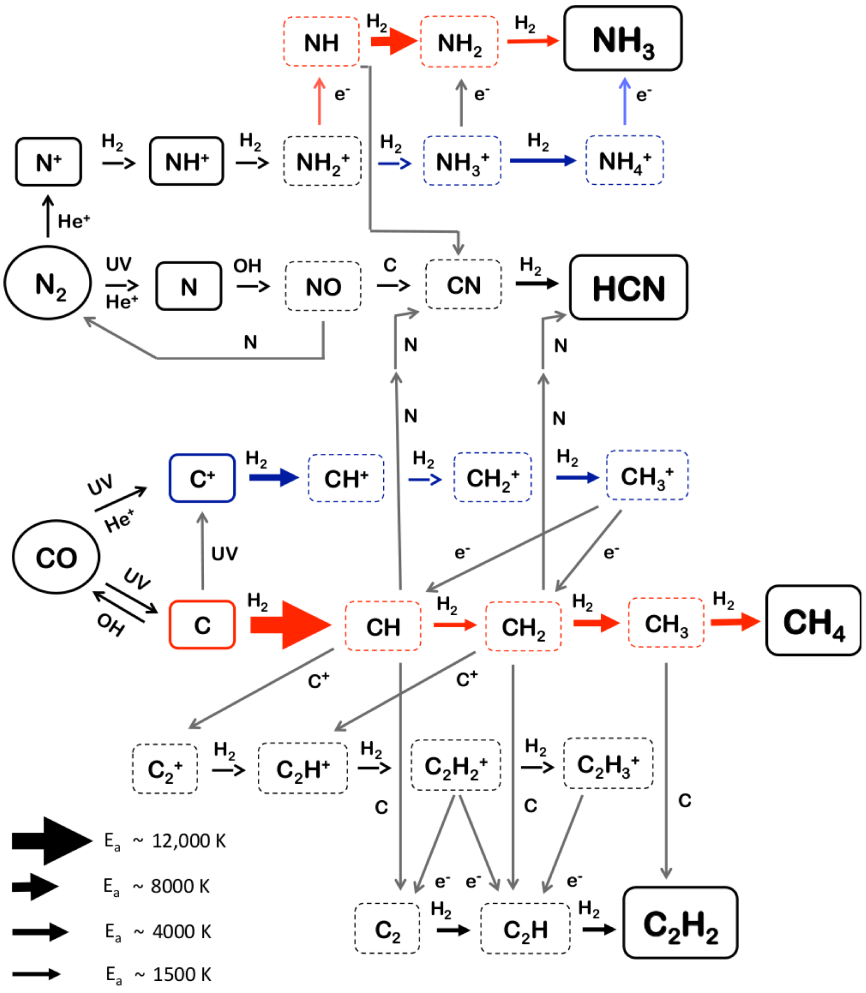

Figure 5.9 Chemical diagram describing the main reaction routes to form HCN, C_2H_2, CH_4 and NH_3 in warm gas in protoplanetary disks or hot cores depending on the radiation fields, temperature and different molecular abundances, adapted from Agúndez et al. (2008). At high temperatures of several hundred K the reaction routes (in red) starting with C reacting with H_2 to CH and NH to NH_2 dominate over lower temperature chemical routes (in blue) of C^+ going to CH^+ and NH_3^+ and NH_4^+. The different activation energy (E_a) barriers for the chemical reactions are represented by different types of arrows; the thicker the arrow, the higher the activation energy.

stars, which has been studied for decades (e.g., Cherchneff & Glassgold 1993, Millar & Herbst 1994). For example, C_2H_2 reacts with CH_3 to produce C_3H_4, with C_2H to C_4H_2, and with NH_3 to CH_3CN. If C_2H is sufficiently abundant (due to photodissociation of C_2H_2, for example), subsequent reactions may lead to large unsaturated carbon chains. More saturated molecules such as C_2H_4 and C_2H_6 need CH_4 as their starting point. Finally, nitrogen-containing species are produced by reactions of HCN or N with hydrocarbons. For example, C_2H_2 and C_2H react with HCN to form HC_3N. It is now well established that many of these neutral-neutral reactions actually have substantial rates even at low temperatures (<100 K) (Smith 2011). Thus, the bottleneck in producing the more complex organic molecules is the formation of the chemical precursors C_2H_2, HCN and CH_4.

Benzene is the most complex molecule probed here and is a precursor for building larger PAHs. One route to form benzene is through the reaction of C_3H_4 and its ion, found to be important in the inner disk chemistry in some models (Woods & Willacy 2007). Alternatively, the destruction of PAHs by high temperature gas-phase reactions inside the 'soot line' can lead to the production of small hydrocarbons, including C_2H_2 and perhaps C_6H_6 (Kress et al. 2010).

CO_2 is the product of the reaction of OH with CO. Models show that all atomic O is driven into H_2O at temperatures above ~230 K if there are no rapid H_2O destruction routes (e.g., Draine et al. 1983, Charnley 1997). The formation of OH also needs elevated temperatures, but peaks in the 100–200 K range because of the rapid reactions of OH with H_2 to form H_2O at higher temperatures. In warm gas, the CO_2 abundance follows that of OH and also peaks at 100–200 K, with a strong decrease toward higher temperatures.

In the following sections, more detailed descriptions of a few specific protoplanetary disk models are given, focussing on the simpler species.

X-ray dominated region (XDR) surface layers

Najita et al. (2011) have analyzed the chemistry of the inner (0.25–20 AU) portions of protoplanetary disks exposed to X rays. The physical structure derives from the thermochemical model developed by Glassgold et al. (2009). The thermal structure is evaluated separately for dust and gas and the surface gas temperature significantly exceeds that of the dust in the upper layers. In their model, gas and dust temperatures are decoupled for column densities less than 10^{22} cm^{-2}. If only the disk surface is considered ($N < 3{\cdot}10^{21}$ cm^{-2}), gas temperatures of 300 K are reached out to radial distances of 4 AU.

The formation of hydrocarbons in this model is triggered by X-rays which produce He^+ which liberates the C^+ from CO and N from N_2. Acetylene is subsequently produced by C and C^+ insertion reactions with small hydrocarbon radicals (Fig. 5.9). Hence, the C_2H_2 abundance is sensitive to the X-ray ionization rate. Radicals such as OH are also sensitive to X-rays. At low temperature, OH results from the recombination of H_3O^+ produced by ion-molecule reactions and its abundance scales directly with the ionization rate. The formation rate of daughter

species of OH such as NO, SO, SO_2 and CO_2 is similarly increased by X-ray ionization. However, if their destruction is also dominated by He^+, their abundances are not sensitive to the X-ray ionization flux. This is the case for CO_2, for example. Note that the models of Najita et al. (2011) do not include UV photodissociation and may thus underestimate the amount of OH that could be produced from H_2O in the upper layers.

The transformation of N back to N_2 is mediated by neutral reactions and is accompanied by significant column densities of warm nitrogen-bearing molecules such as HCN and NH_3 in these models. Specifically, HCN is influenced by X-ray ionization in its formation route because it liberates N from N_2 and then N reacts with OH to form NO, with NO subsequently reacting with C to form CN. HCN is then formed through reactions of CN with H_2. Because of lack of photodissociation in the model, HCN is destroyed by He^+ and hence destruction is also sensitive to the X-ray. In the end, the HCN decreases slightly with X-ray luminosity in the models by Najita et al. (2011).

Photodissociation region (PDR) surface layers

Various recent models have analyzed the gas phase chemistry of hot inner regions of protoplanetary disks including UV radiation for the chemistry and heating of the gas (Agúndez et al. 2008, Woitke et al. 2009, Willacy & Woods 2009, Vasyunin et al. 2011, Walsh et al. 2012). The Agúndez et al. (2008) study is particularly instructive because they present models for just the photosphere of the disk, down to H_2 column densities of 5×10^{21} cm^{-2} to which the UV penetrates. In their models, FUV photons and cosmic rays produce C, C^+ and N. Atomic N is then channeled to HCN through a similar reaction routine as that described in Fig. 5.9. The C^+ leads to a rich hydrocarbon radical chemistry. However, the formation of high abundances of C_2H_2 and CH_4 requires the reaction of atomic C with H_2 to proceed which has a very high activation barrier. This reaction only proceeds in very warm gas ($T > 500$ K) forming CH. This is reflected in the radial dependence of the C_2H_2 and CH_4 columns, which reach values of $\sim 10^{16}$ cm^{-2} out to radii of ~1 AU, but then drop by orders of magnitude in the colder gas. This rapid drop with disk radius is also seen in models by other authors. In contrast, the CO_2 column increases with radius in the inner 1 AU since it favors somewhat colder gas.

Walsh et al. (2012) present a combined UV + X-ray model which shows that a correct treatment of the photodissociation is generally more important than including X-rays. For the important species considered here —C_2H_2, HCN, CO_2, CH_4 and NH_3— the column densities in the inner disk do not change measurably when X-rays are added to the UV model.

The O/C ratio and hydrocarbon abundances

There have been suggestions that the O/C ratio in the gas changes with disk radius due to migration of icy planetesimals containing a large fraction of the

oxygen (Ciesla & Cuzzi 2006). Hydrocarbon abundances are very sensitive to the O/C ratio (Langer & Graedel 1989, Bettens et al. 1995, Najita et al. 2011). As expected, oxygen-bearing species such as H_2O and O_2 decrease dramatically in abundance when O/C is less than 1 because all volatile oxygen (rather than all carbon) is locked up in CO. Pure carbon species such as C_2H_2 increase in abundance by orders of magnitude while nitrogen species only change appreciably when they contain C (e.g., HCN). All of this reflects the presence of excess amounts of carbon that is available for hydrocarbon formation when O/C$<$ 1. Since both IRS 46 and GV Tau show large columns of gaseous CO_2, the lines of sight through the disks probed by the mid-infrared data must pass through gas with O/C$\geq$ 1.

Another parameter that may affect the abundances and the O/C ratio is the overall gas/dust ratio (e.g., Najita et al. 2011, Bruderer et al. 2012). However, comparison of the CO column density with the extinction measured from the silicate optical depth shows that this ratio is close to the interstellar value for both IRS 46 and GV Tau, indicating no significant grain growth and settling along the lines of sight through these disks (Kruger et al. 2011).

5.4.2 Surface chemistry

The more complex organic molecules such as dimethyl ether seen toward protostars are the product of an active gas-grain interaction (see Tielens & Charnley 1997, Herbst & van Dishoeck 2009,for reviews). Recent models produce these species on the grains rather than in hot gas-phase chemistry, either through direct grain surface chemistry or through mild photolysis of simple ice species resulting in radicals which then react with each other to form more complex species (Garrod et al. 2008, Öberg et al. 2009). These types of grain chemistry – either direct surface reactions or photolysis – will not result in high abundances of C_2H_2 and HCN because these species will be readily hydrogenated by H. On grain surfaces, N is quickly converted to NH_3, while in the gas phase, N flows through NO to N_2 with a slight detour to HCN. Grain surface reactions lead to very high abundances of NH_3, especially in relation to HCN. Observations and comparisons with model predictions show that also CH_4 formation is very efficient on dust grains (Öberg et al. 2008).

5.4.3 Comparison of models with observations

Table 5.5 and Figures 5.7 and 5.8 show that warm chemistry can explain the observed abundance ratios of HCN, C_2H_2 and CO_2 as well as most limits. In the Markwick et al. (2002) models, all abundance ratios are close to unity, but these ratios refer to the entire disk rather than just the surface layers. It is therefore not possible to properly test these models. The models of Agúndez et al. (2008) and Najita et al. (2011) provide column densities for just the warm surface layers,

but tabulate only a limited number of species.

The inner disk models of Agúndez et al. (2008) provide the correct range of column densities and abundance ratios in the surface layers around 1 AU. At 3 AU, the C_2H_2 column has dropped dramatically due to the lower temperature and the model overproduces the CO_2/C_2H_2 ratio by a factor >100. The XDR model results given by Najita et al. (2011), for the reference case of a disk at 1 AU, agree less well with the observations than the PDR model results at 1 AU. For example the SO_2, NH_3 and CO_2 model ratios relative to C_2H_2 are several orders of magnitude higher than our observed upper limits and detections. Lowering the O/C ratio to 1 instead of 2.5 decreases the difference between the observations and the pure X-ray models but now underproduces CO_2. Further examination of chemistry in the surface layers of combined UV + X-ray models such as produced by Walsh et al. (2012) are needed to better test their effects.

The importance of grain-gas interaction for the composition of the inner regions of the disk may well be revealed by NH_3 and CH_4 searches. As mentioned in section 5.4.2, high abundances of CH_4 and NH_3 relative to HCN and C_2H_2 indicate that the chemistry in the inner part of disks could be reset due to evaporation of ices from dust grains. Table 5.6 includes the results from model M of Garrod et al. (2008). The efficiency to form NH_3 on dust grains is the main reason why NH_3/HCN and CH_3CN/NH_3 are so different in the grain surface models of Garrod et al. (2008) compared with the warm chemistry models developed by Najita et al. (2011) and Agúndez et al. (2008). Our CH_3CN/NH_3 ratio derives from two upper limits and is thus of limited value for testing models. However, our observed limit on NH_3/HCN clearly favors a low ratio for the abundances of these species, inconsistent with a significant contribution from pure grain chemistry.

The observed upper limits on the other species investigated here are often higher or comparable to what the chemical models predict. Thus, a firm conclusion from our data is that the molecular abundance ratios cannot be higher than what is predicted in the current models. However they can be lower by up to an order of magnitude, and future observations with MIRI or ELT with their higher spectral resolution can in several cases directly test the ratios given by the chemical models (see Table 5.5). Specifically, deep searches for HNC, HC_3N, C_6H_6, SO_2 and NH_3 should distinguish between models.

5.4.4 Comparison with protostars, other disks and comets

The abundance ratios of the detected molecules —HCN, C_2H_2 and CO_2— are remarkably close (within factors of two) to those observed toward high-mass protostars (Lahuis & van Dishoeck 2000), which have been interpreted with high temperature gas-phase chemistry models (Doty et al. 2002). Since our NH_3/HCN limits of <1.1 are close to the detected NH_3/HCN ratio of ~1.2 toward one high-mass protostar (Knez et al. 2009), this suggests that deeper high resolution searches for NH_3 may be fruitful.

It is also interesting to compare the two observed C_2H_2/HCN abundance ratios of 0.6 and 0.8 for IRS 46 and GV Tau respectively with the one order of magnitude lower values presented in Carr & Najita (2011) for 5 protoplanetary disks in Taurus. Those ratios have been inferred from emission lines, whereas ours come from absorption data and thus probe a different part of the disk. This would imply that the C_2H_2/HCN abundance ratios probed through our edge-on disks presented are more similar to the hot cores and comets in Fig. 12 of Carr & Najita (2011) than to their protoplanetary disks. However, Salyk et al. (2011) and Mandell et al. (2012) present C_2H_2/HCN abundance ratios of ~1 for several protoplanetary disks derived from emission data, which is about the same abundance ratio as the comet and hot core observations. Thus, different analysis methods of emission data can lead to an order of magnitude different abundance ratios.

It is interesting to further compare our inferred molecular ratios to those observed in comets, see Table 5.5 and Figures 5.7 and 5.8. The ratios tabulated for comets are presented as ranges between the highest and lowest observed ratios (Mumma & Charnley 2011), and are all within our observed upper limits and detections. This comparison suggests that some of the HCN and C_2H_2 produced by warm chemistry in the inner disk is incorporated into cold comets. However, the presence of complex organics such as dimethyl ether in high abundances in comets (see Bockelée-Morvan 2011,for a recent review) suggests that the ice chemistry route is also important for their organic inventory.

In summary, our observed ratios suggest that warm chemistry models are most relevant for explaining the observed abundance patterns. Future higher resolution observations of these molecules with JWST-MIRI and other facilities can help in answering the question to what extent warm chemistry and surface chemistry contribute to the chemical composition of the gas in the planet- and comet-forming zones of disks.

5.5 Conclusions

In this paper, mid-infrared spectra of HCN, C_2H_2 and CO_2 have been analyzed for two edge-on disks, IRS 46 and GV Tau. The high S/N data have also been used to put upper limits on the abundances of other molecules predicted to be abundant in the inner disk. The main conclusions are:

- The two disks have similar column densities and similar abundance ratios of warm HCN, C_2H_2 and CO_2. The first two molecules probe gas with excitation temperatures $T \sim 400 - 700$ K, whereas CO_2 probes somewhat cooler gas. These results are similar to those found toward massive protostars.

- No other absorption features are detected above 3σ in either source, providing upper limits on a variety of hydrocarbon molecules, NH_3 and SO_2 that are of order unity or less with respect to C_2H_2 or HCN.

- The upper limits relative to C_2H_2 and HCN are either higher or close to values given by high temperature chemistry models of protoplanetary disks. The observed NH_3/HCN limit is much lower than would be expected if the chemistry in disks would have been reset due to evaporation of icy mantles on dust grains.
- Hot chemistry disk models including both X-ray and UV radiation produce abundance ratios in better agreement with our observations than pure X-ray models.
- The observed abundance ratios in comets are within the same range as our observed ratios or upper limits. The composition of comets could therefore be partly build up from gas in the inner regions of protoplanetary disks mixed outward to the comet-forming zone.
- Future observations using higher resolution instruments on SOFIA, JWST-MIRI, SPICA or ELT will be able to detect column densities which are an order of magnitude lower than the upper limits extracted from the *Spitzer*-IRS data. Such data would provide much better constraints of the hot gas phase chemical models of the inner disk. Edge-on systems such as IRS 46 and GV Tau remain uniquely suited for this purpose.

Acknowledgements

The authors are grateful to Catherine Walsh for further information on inner disk models. JEB is supported by grant 614.000.605 from Netherlands Organization of Scientific Research (NWO). EvD and FL acknowledge support from a NWO Spinoza Grant, from the Netherlands Research School for Astronomy (NOVA) and from A-ERC grant 291141-CHEMPLAN.

Appendix

Auxiliary figures

This appendix presents simulations of the spectra of all molecules considered here at higher spectral resolving power of $R = 3000$ and $R = 50000$, appropriate for future instruments. In addition, spectra at the *Spitzer* resolving power of $R = 600$ are included. All spectra are computed for $T_{ex} = 200$, 500 and 1000 K, $b = 5$ km s^{-1} and a column density of $1 \cdot 10^{16}$ cm^{-2}.

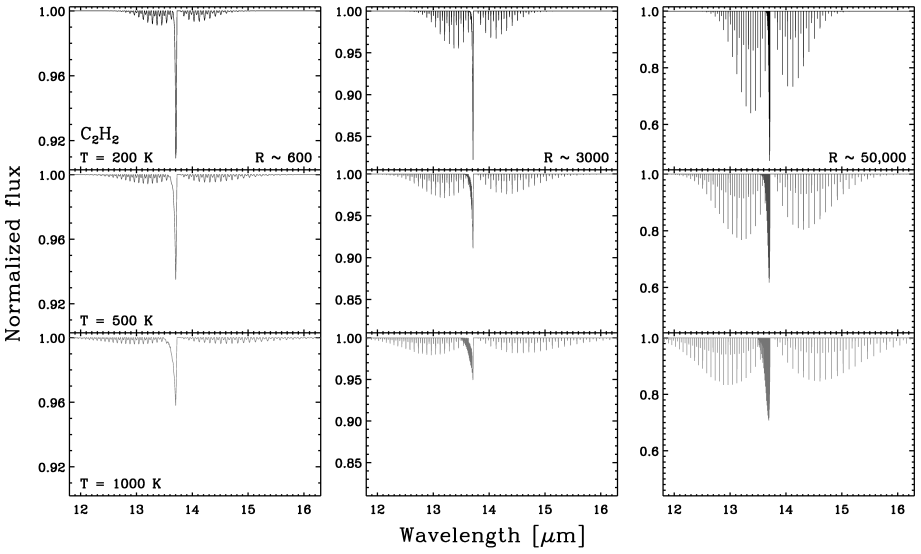

Figure 10 The synthetic spectrum of C_2H_2 at a column density of $1.0 \cdot 10^{16}$ cm^{-2}, excitation temperatures of 200 (top), 500 (middle) and 1000 K (bottom), and spectral resolving powers of 600 (left), 3000 (middle) and 50,000 (right). Note the different vertical scales for the different spectral resolving powers in this and subsequent figures .

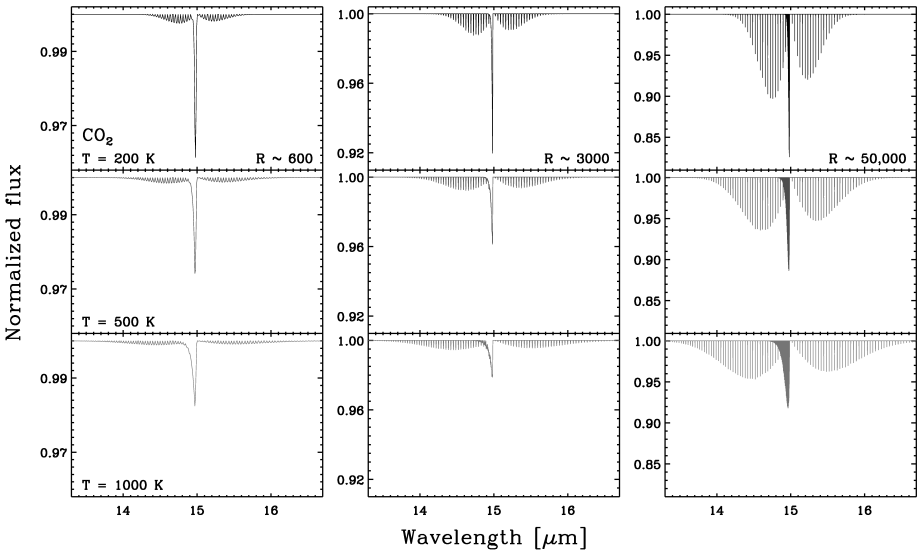

Figure 11 The synthetic spectrum of CO_2 at a column density of $1.0 \cdot 10^{16}$ cm^{-2}, excitation temperatures of 200 (top), 500 (middle) and 1000 K (bottom), and spectral resolving powers of 600 (left), 3000 (middle) and 50,000 (right).

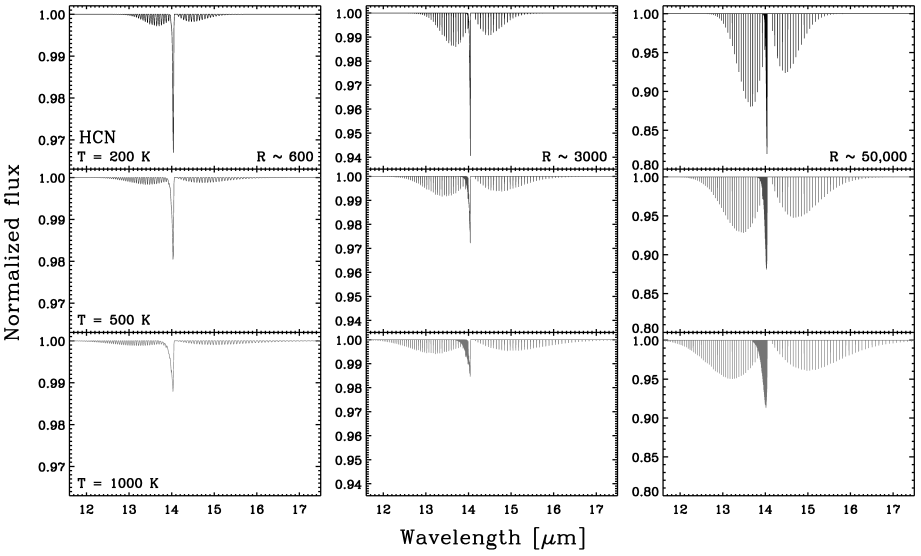

Figure 12 The synthetic spectrum of HCN at a column density of $1.0 \cdot 10^{16}$ cm^{-2}, excitation temperatures of 200 (top), 500 (middle) and 1000 K (bottom), and spectral resolving powers of 600 (left), 3000 (middle) and 50,000 (right).

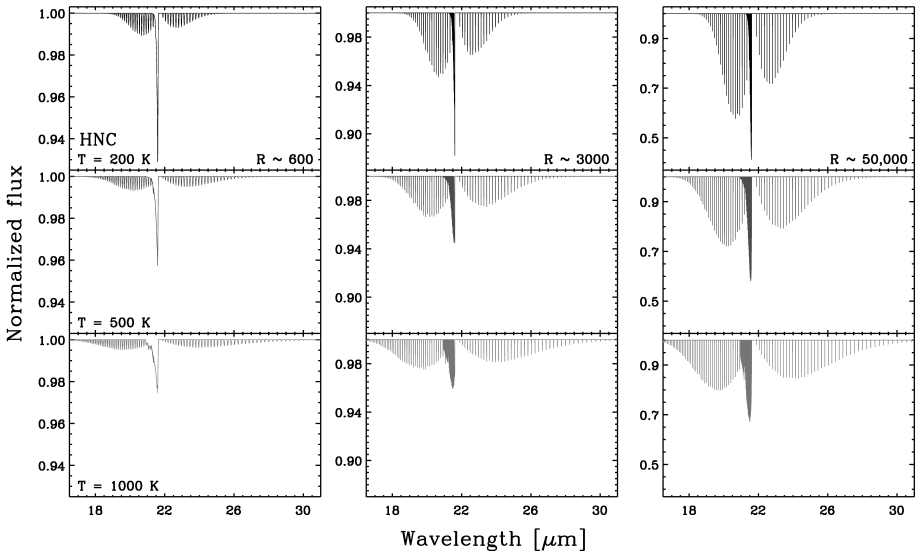

Figure 13 The synthetic spectrum of HNC at a column density of $1.0 \cdot 10^{16}$ cm^{-2}, excitation temperatures of 200 (top), 500 (middle) and 1000 K (bottom), and spectral resolving powers of 600 (left), 3000 (middle) and 50,000 (right).

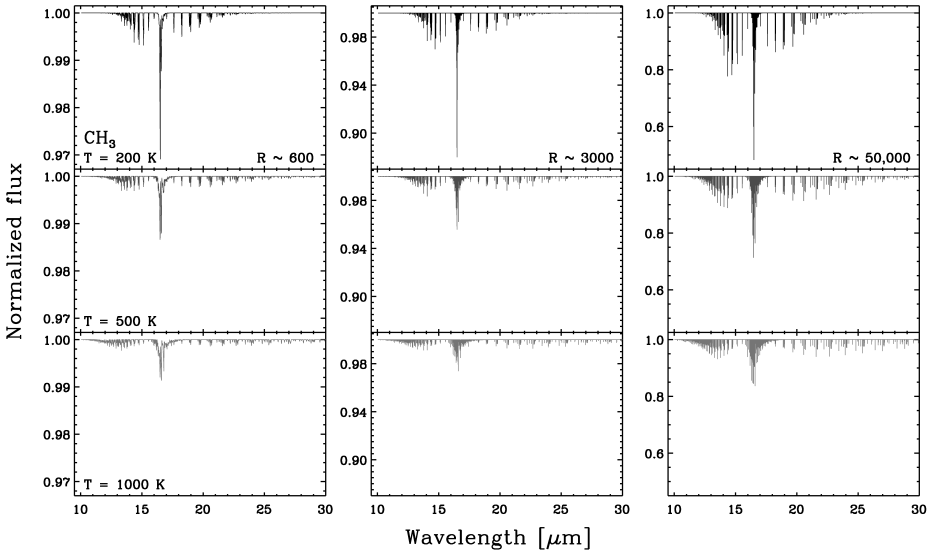

Figure 14 The synthetic spectrum of CH_3 at a column density of $1.0 \cdot 10^{16}$ cm^{-2}, excitation temperatures of 200 (top), 500 (middle) and 1000 K (bottom), and spectral resolving powers of 600 (left), 3000 (middle) and 50,000 (right).

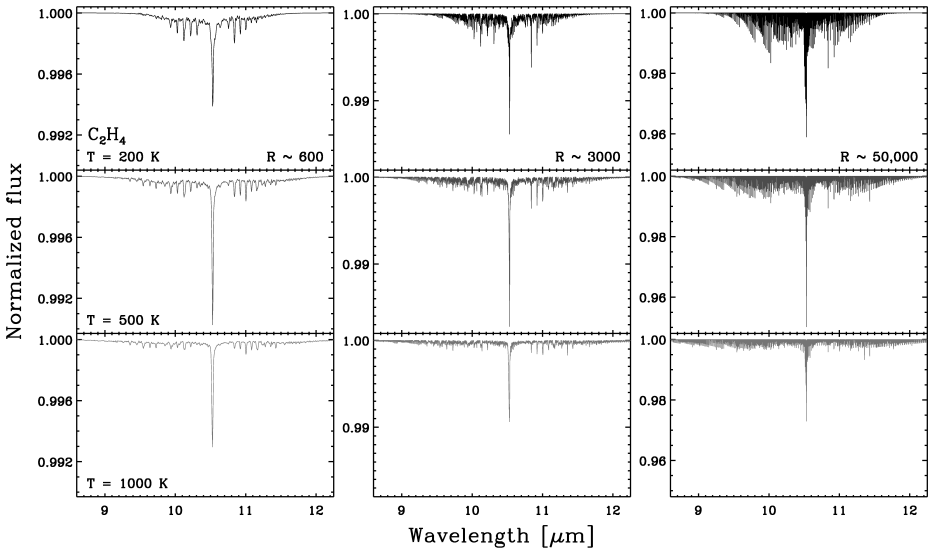

Figure 15 The synthetic spectrum of C_2H_4 at a column density of $1.0 \cdot 10^{16}$ cm^{-2}, excitation temperatures of 200 (top), 500 (middle) and 1000 K (bottom), and spectral resolving powers of 600 (left), 3000 (middle) and 50,000 (right).

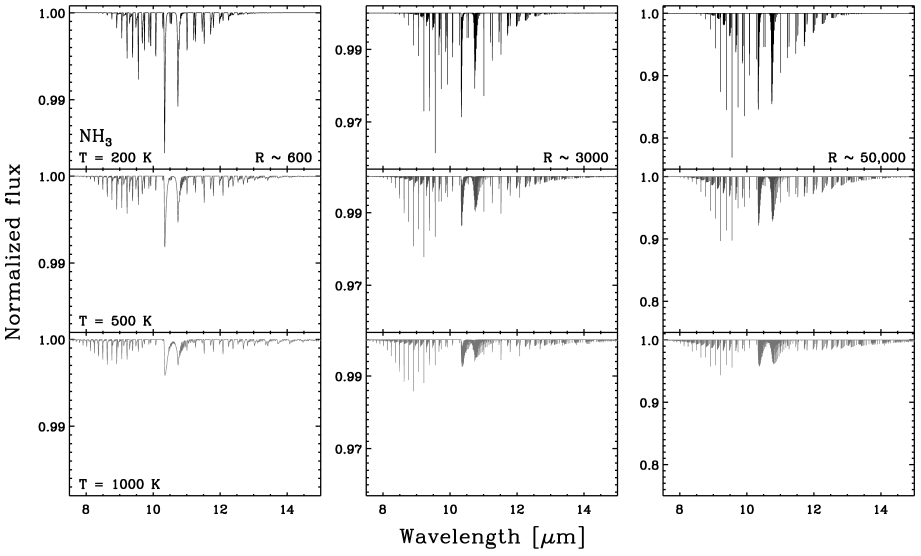

Figure 16 The synthetic spectrum of NH_3 at a column density of $1.0{\cdot}10^{16}$ cm^{-2}, excitation temperatures of 200 (top), 500 (middle) and 1000 K (bottom), and spectral resolving powers of 600 (left), 3000 (middle) and 50,000 (right).

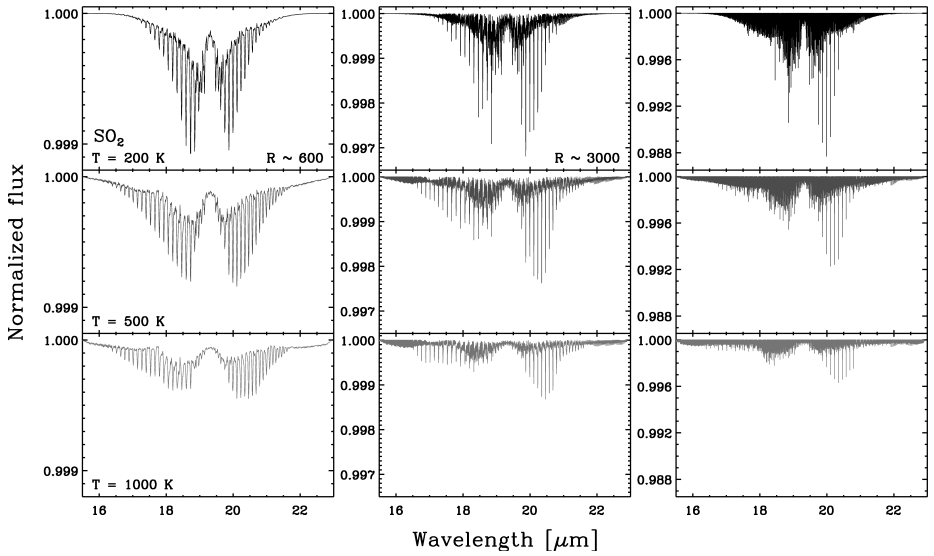

Figure 17 The synthetic spectrum of SO_2 at a column density of $1.0{\cdot}10^{16}$ cm^{-2}, excitation temperatures of 200 (top), 500 (middle) and 1000 K (bottom), and spectral resolving powers of 600 (left), 3000 (middle) and 50,000 (right).

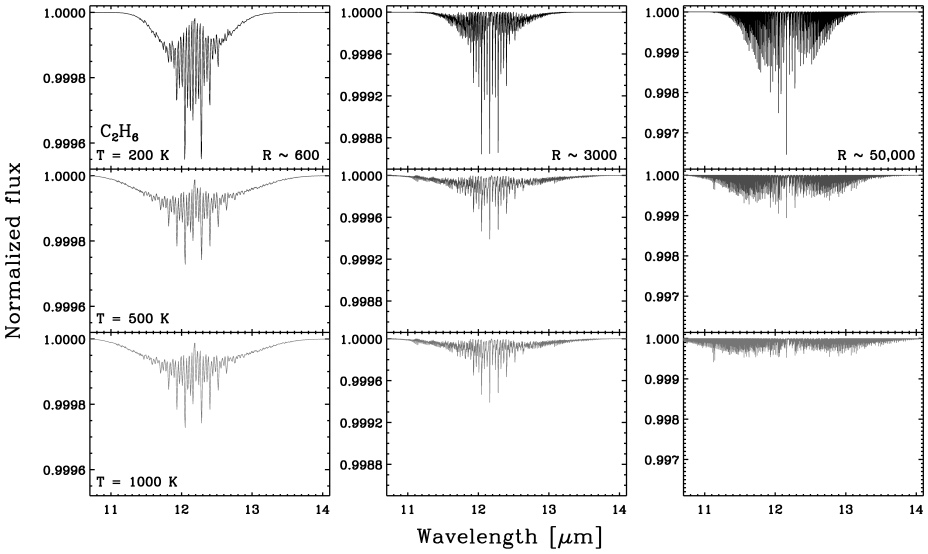

Figure 18 The synthetic spectrum of C_2H_6 at a column density of $1.0 \cdot 10^{16}$ cm^{-2}, excitation temperatures of 200 (top), 500 (middle) and 1000 K (bottom), and spectral resolving powers of 600 (left), 3000 (middle) and 50,000 (right).

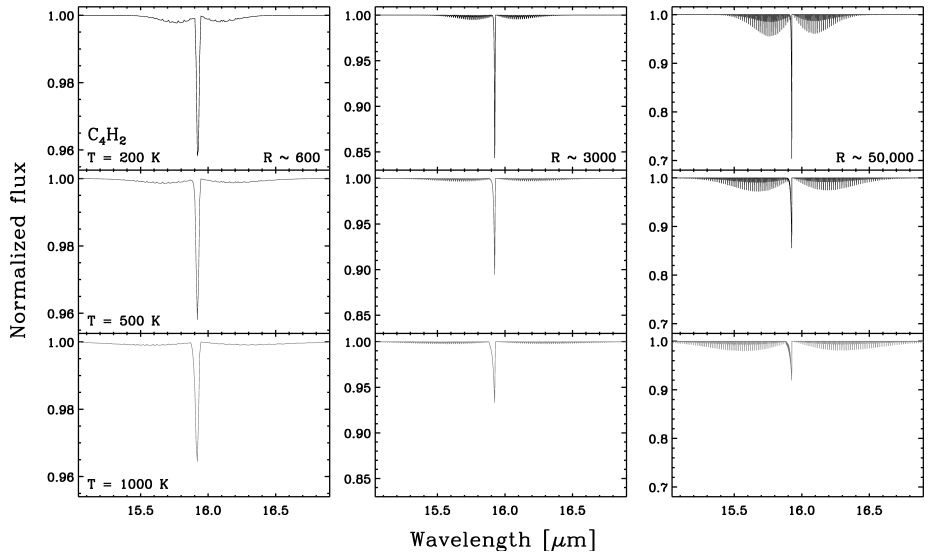

Figure 19 The synthetic spectrum of C_4H_2 at a column density of $1.0 \cdot 10^{16}$ cm^{-2}, excitation temperatures of 200 (top), 500 (middle) and 1000 K (bottom), and spectral resolving powers of 600 (left), 3000 (middle) and 50,000 (right).

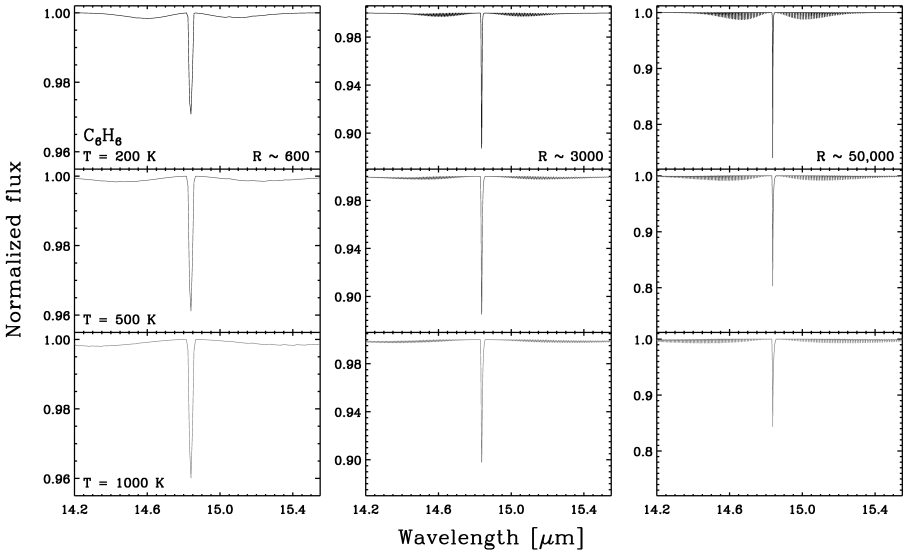

Figure 20 The synthetic spectrum of C_6H_6 at a column density of $1.0 \cdot 10^{16}$ cm^{-2}, excitation temperatures of 200 (top), 500 (middle) and 1000 K (bottom), and spectral resolving powers of 600 (left), 3000 (middle) and 50,000 (right).

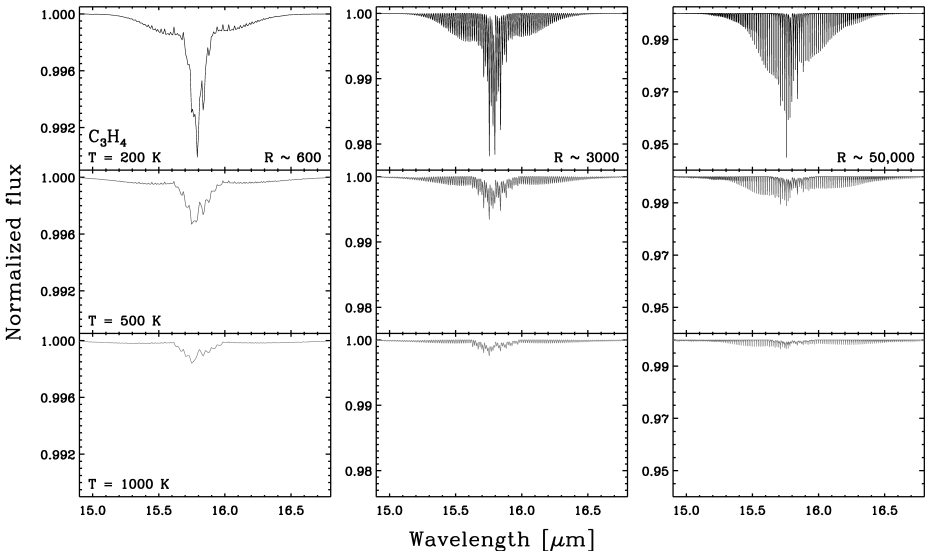

Figure 21 The synthetic spectrum of C_3H_4 at a column density of $1.0 \cdot 10^{16}$ cm^{-2}, excitation temperatures of 200 (top), 500 (middle) and 1000 K (bottom), and spectral resolving powers of 600 (left), 3000 (middle) and 50,000 (right).

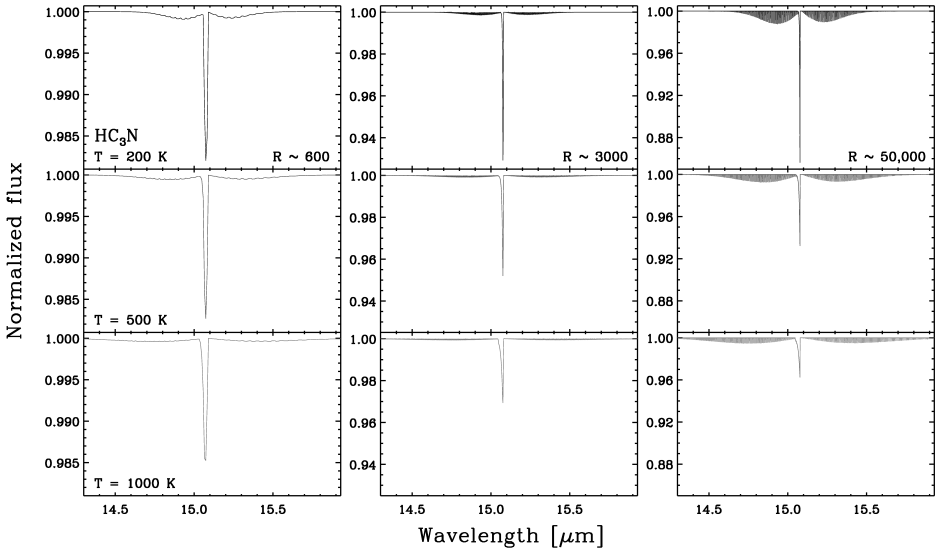

Figure 22 The synthetic spectrum of HC_3N at a column density of $1.0 \cdot 10^{16}$ cm^{-2}, excitation temperatures of 200 (top), 500 (middle) and 1000 K (bottom), and spectral resolving powers of 600 (left), 3000 (middle) and 50,000 (right).

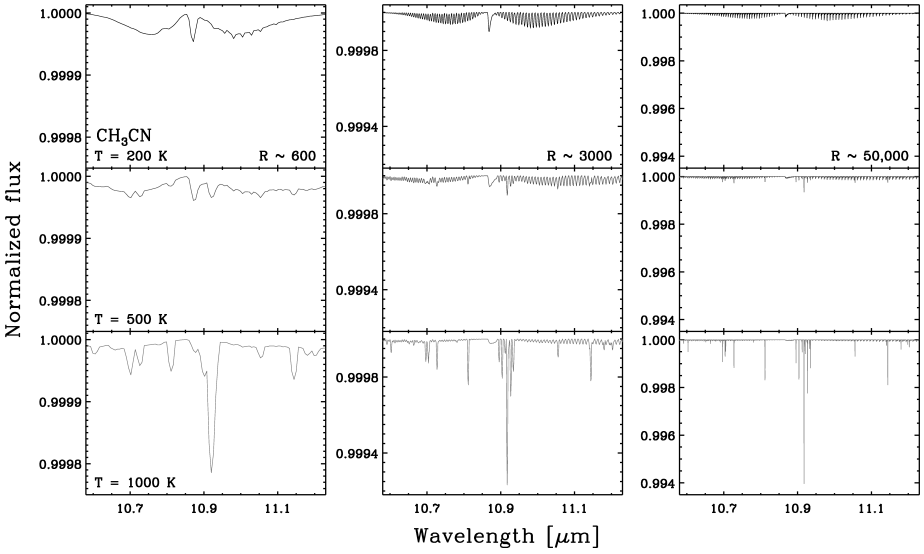

Figure 23 The synthetic spectrum of CH_3CN at a column density of $1.0 \cdot 10^{16}$ cm^{-2}, excitation temperatures of 200 (top), 500 (middle) and 1000 K (bottom), and spectral resolving powers of 600 (left), 3000 (middle) and 50,000 (right).

Bibliography

Adams, F. C., Lada, C. J., & Shu, F. H. 1987, ApJ, 312, 788

Alexander, R. D. 2008, MNRAS, 391, L64

Agúndez, M., Cernicharo, J., & Goicoechea, J. R. 2008, A&A, 483, 831

Aikawa, Y., Umebayashi, T., Nakano, T., & Miyama, S. M. 1999, ApJ, 519, 705

André, P., Ward-Thompson, D., & Barsony, M. 1993, ApJ, 406, 122

Andrews, S. M. & Williams, J. P. 2007, ApJ, 659, 705

Andrews, S., 2008, PhD thesis, University of Hawaii

Andrews, S. M., Wilner, D. J., Hughes, A. M., Qi, C., & Dullemond, C. P. 2009, ApJ, 700, 1502

Appenzeller, I., Krautter, J., & Jankovics, I. 1983, Astronomy and Astrophysics Supplement Series, 53, 291

Appenzeller, I., Jetter, R., & Jankovics, I. 1986, A&AS, 64, 65

Ardila, D. R., Basri, G., Walter, F. M., Valenti, J. A., & Johns-Krull, C. M. 2002, ApJ, 567, 1013

Aresu, G., Kamp, I., Meijerink, R., Woitke, P., Thi, W.-F., & Spaans, M. 2011, A&A, 526, A163

Augereau, J. C., Lagrange, A. M., Mouillet, D., & Ménard, F. 2001, A&A, 365, 78

Bally, J., O'Dell, C. R., & McCaughrean, M. J. 2000, AJ, 119, 2919

Bary, J. S., Matt, S. P., Skrutskie, M. F., Wilson, J. C., Peterson, D. E., & Nelson, M. J. 2008, ApJ, 687, 376

Bast, J. E., Brown, J. M., Herczeg, G. J., van Dishoeck, E. F., & Pontoppidan, K. M. 2011, A&A, 527, A119

Bast, J. E., Lahuis, F., Tielens, A. G. G. M. & van Dishoeck, E. F. 2012, submitted

Bergin, E. A., & Tafalla, M. 2007, ARA&A, 45, 339

Bergin, E. A., Aikawa, Y., Blake, G. A., & van Dishoeck, E. F. 2007, Protostars and Planets V, 751

Bergin, E. A. 2011, in 'Physical Processes in Circumstellar Disks Around Young Stars', ed. P. Garcia, (University of Chicago Press: Chicago), p. 55

Bergin, E. A. 2009, arXiv:0908.3708

Bethell, T. & Bergin, E. 2009, Science, 326, 1675
Bettens, R. P. A., Lee, H.-H., Herbst, E. 1995, ApJ, 443, 664
Bitner, M. A., Richter, M. J., Lacy, J. H., Greathouse, T. K., Jaffe, D. T., & Blake, G. A. 2007, ApJ, 661, L69
Blake, G. A., & Boogert, A. C. A. 2004, ApJ, 606, L73
Bockelée-Morvan, D. 2011, in 'The Molecular Universe', IAU Symposium 280, ed. J. Cernicharo & R. Bachiller (Cambridge University Press), p. 261
Bonev, B. P. & Mumma, M. J. 2006, ApJ, 653, 788
Boonman, A. M. S., van Dishoeck, E. F., Lahuis, F., & Doty, S. D. 2003, A&A, 399, 1063
Borucki, W. J., Koch, D. G., Basri, G., et al. 2011, ApJ, 736, 19
Bottinelli, S., Boogert, A. C. A., Bouwman, J., Beckwith, M., van Dishoeck, E. F., Öberg, K. I., Pontoppidan, K. M., Linnartz, H., Blake, G. A., Evans, N. J., & Lahuis, F. 2010, ApJ, 718, 1100
Bouvier, J., Alencar, S. H. P., Boutelier, T., et al. 2007, A&A, 463, 1017
Brandl, B., Blommaert, J., Glasse, A., Lenzen, R., & Pantin, E. 2010, The Messenger, 140, 30
Brittain, S. D., Rettig, T. W., Simon, T., Kulesa, C., DiSanti, M. A., & Dello Russo, N. 2003, ApJ, 588, 535
Brittain, S. D., Simon, T., Najita, J. R., & Rettig, T. W. 2007, ApJ, 659, 685
Brittain, S. D., Najita, J. R., & Carr, J. S. 2009, ApJ, 702, 85
Brogi, M., Snellen, I. A. G., de Kok, R. J., et al. 2012, Nature, 486, 502
Brown, J. M., Blake, G. A., Qi, C., Dullemond, C. P., Wilner, D. J., & Williams, J. P. 2009, ApJ, 704, 496
Brown, J., Pontoppidan, K.M., van Dishoeck, E.F., & Herczeg, G. 2012, subm.
Bruderer, S., van Dishoeck, E. F., Doty, S. D., & Herczeg, G. J. 2012, A&A, 541, A91
Calvet, N., Magris, G. C., Patino, A., & D'Alessio, P. 1992, Rev. Mexicana Astron. Astrofis., 24, 27
Carmona, A., van den Ancker, M. E., & Henning, T. 2007, A&A, 464, 687
Carr, J. S. 1989, ApJ, 345, 522
Carr, J. S., Tokunaga A. T., Najita, J., Shu, F. H., & Glassgold, A. E. 1993, ApJ, 411, L37
Carr, J. S., Tokunaga, A. T., & Najita, J. 2004, ApJ, 603, 213
Carr, J. S., & Najita, J. R. 2008, Science, 319, 1504
Carr, J. S., & Najita, J. R. 2011, ApJ, 733, 102
Chandler, C. J., Carlstrom, J. E., Scoville, N. Z., Dent, W. R. F., & Geballe, T. R. 1993, ApJ, 412, L71
Chandra, S., & Sharma, A. K. 2001, A&A, 376, 356
Charnley, S. B. 1997, ApJ, 481, 396
Cherchneff, I., Glassgold, A.E. 1993, ApJ, 419, L41

Chiang, E. I., & Goldreich, P. 1997, ApJ, 490, 368
Ciesla, F. J., Cuzzi, J. N. 2006, Icarus, 181, 178
Clampin, M., Krist, J. E., Ardila, D. R., et al. 2003, AJ, 126, 385
Clary, D. C. 1983, J. Chem. Phys., 78, 4915
Clough, S. A., Iacono, M. J., & Moncet, J. -L. 1982, J. Geophys. Res., 97, 15,761-15785.
Clough, S. A., Shephard, M. W., Mlawer, E. J., Delamere, J. S., Iacono, M. J., Cady-Pereira, K., Boukabara, S., & Brown, P. D. 2005, Journal of Quantitative Spectroscopy and Radiative Transfer, 91, 233
Crapsi, A., van Dishoeck, E. F., Hogerheijde, M. R., Pontoppidan, K. M., & Dullemond, C. P. 2008, A&A, 486, 245
Cutri, R. M., Skrutskie, M. F., van Dyk, S., Beichman, C. A., Carpenter, J. M., Chester, T., Cambresy, L., Evans, T., Fowler, J., Gizis, J., Howard, E., Huchra, J., Jarrett, T., Kopan, E. L., Kirkpatrick, J. D., Light, R. M., Marsh, K. A., McCallon, H., Schneider, S., Stiening, R., Sykes, M., Weinberg, M., Wheaton, W. A., Wheelock, S., & Zacarias, N. 2003, 2MASS All Sky Catalog of point sources. (The IRSA 2MASS All-Sky Point Source Catalog, NASA/IPAC Infrared Science Archive.)
D'Alessio, P., Canto, J., Calvet, N., & Lizano, S. 1998, ApJ, 500, 411
Decin, L., Morris, P. W., Appleton, P. N., et al. 2004, ApJS, 154, 408
Désert, J.-M., Bean, J., Miller-Ricci Kempton, E., et al. 2011, ApJ, 731, L40
di Francesco, J., Evans, N. J., II, Caselli, P., et al. 2007, Protostars and Planets V, 17
Doppmann, G. W., Najita, J. R., & Carr, J. S. 2008, ApJ, 685, 298
Doty, S. D., van Dishoeck, E. F., van der Tak, F. F. S., & Boonman, A. M. S. 2002, A&A, 389, 446
Draine, B. T., Roberge, W. G., Dalgarno, A. 1983, ApJ, 264, 485
Dutrey, A., Guilloteau, S., & Guelin, M. 1997, A&A, 317, L55
Dullemond, C. P., & Dominik, C. 2004, A&A, 417, 159
Dullemond, C. P., & Monnier, J. D. 2010, ARA&A, 48, 205
Dumouchel, F., Faure, A., & Lique, F. 2010, MNRAS, 406, 2488
Edwards, S., Fischer, W., Hillenbrand, L., & Kwan, J. 2006, ApJ, 646, 319
Ehrenfreund, P., & Charnley, S. B. 2000, ARA&A, 38, 427
Eisner, J. A., Hillenbrand, L. A., White, R. J., Akeson, R. L., & Sargent, A. I. 2005, ApJ, 623, 952
Ercolano, B., & Owen, J. E.
Evans, N. J., II, Lacy, J. H., & Carr, J. S. 1991, ApJ, 383, 674
Evans, N.J. et al. 2003, PASP, 115, 965
Evans, N. J., Dunham, M. M., Jørgensen, J. K., et al. 2009, ApJS, 181, 321
Fedele, D., Pascucci, I., Brittain, S., Kamp, I., Woitke, P., Williams, J. P., Dent, W. R. F., & Thi, W.-F. 2011, ApJ, 732, 106

Fuente, A., Cernicharo, J., Agúndez, M., Berné, O., Goicoechea, J. R., Alonso-Albi, T., & Marcelino, N. 2010, A&A, 524, A19
Fuente, A., Cernicharo, J., & Agúndez, M. 2012, arXiv:1206.5076
Fukagawa, M., Hayashi, M., Tamura, M., et al. 2004, ApJ, 605, L53
Garcia Lopez, R., Natta, A., Testi, L., & Habart, E. 2006, A&A, 459, 837
Garrod, R. T., Weaver, S. L. W., & Herbst, E. 2008, ApJ, 682, 283
Geers, V. C., et al. 2006, A&A, 459, 545
Gibb, E. L., Rettig, T., Brittain, S., Haywood, R., Simon, T., & Kulesa, C. 2004, ApJ, 610, L113
Gibb, E. L., Van Brunt, K. A., Brittain, S. D., & Rettig, T. W. 2007, ApJ, 660, 1572
Gibb, E. & Troutman, M., 2011, IAU Symposium 280, Poster 31
Glass, I. S. & Penston, M. V. 1974, Royal Astronomical Society, 167, 237
Glassgold, A. E. & Najita, J. R. 2001, Young Stars Near Earth: Progress and Prospects, 244, 251
Glassgold, A. E., Meijerink, R., & Najita, J. R. 2009, ApJ, 701, 142
Goicoechea, J. R., & Nakagawa, T. 2011, in 'Conditions and impact of star formation', EAS series, vol. 52, ed. M. Röllig et al. (EDP Sciences), p. 253
Gorti, U., & Hollenbach, D. 2008, ApJ, 683, 287
Gorti, U., Dullemond, C. P., & Hollenbach, D. 2009, ApJ, 705, 1237
Gorti, U., & Hollenbach, D. 2009, ApJ, 690, 1539
Gorti, U., Hollenbach, D., Najita, J., & Pascucci, I. 2011, ApJ, 735, 90
Grady, C. A., Woodgate, B., Bruhweiler, F. C., et al. 1999, ApJ, 523, L151
Grady, C. A., Woodgate, B. E., Bowers, C. W., et al. 2005, ApJ, 630, 958
Grady, C. A., et al. 2009, ApJ, 699, 1822
Gras-Velázquez, À., & Ray, T. P. 2005, A&A, 443, 541
Gregory, S. G., Matt, S. P., Donati, J.-F., & Jardine, M. 2008, MNRAS, 389, 1839
Guenther, E. W., Esposito, M., Mundt, R., Covino, E., Alcalá, J. M., Cusano, F., & Stecklum, B. 2007, A&A, 467, 1147
Günther, H. M., & Schmitt, J. H. M. M. 2008, A&A, 481, 735
Gullbring, E., Hartmann, L., Briceno, C., & Calvet, N. 1998, ApJ, 492, 323
Hartigan, P., Hartmann, L., Kenyon, S. J., Strom, S. E., & Skrutskie, M. F. 1990, ApJ, 354, L25
Hartmann, L., Hewett, R., & Calvet, N. 1994, ApJ, 426, 669
Hartmann, L., Calvet, N., Gullbring, E., & D'Alessio, P. 1998, ApJ, 495, 385
Heap, S. R., Lindler, D. J., Lanz, T. M., et al. 2000, ApJ, 539, 435
Heinzeller, D., Nomura, H., Walsh, C., & Millar, T. J. 2011, ApJ, 731, 115
Helmich, F. P. 1996, PhD thesis, Leiden Observatory, Leiden University
Henning, T., et al. 2010, ApJ, 714, 1511
Herczeg, G. J., & Hillenbrand, L. A. 2008, ApJ, 681, 594
Herbst, E., & van Dishoeck, E. F. 2009, ARA&A, 47, 427

Hogerheijde, M. 1998, Ph.D. Thesis,
Hogerheijde, M., et al. 2011, Science, 334, 338
Hughes, A. M., Wilner, D. J., Cho, J., Marrone, D. P., Lazarian, A., Andrews, S. M., & Rao, R. 2009, ApJ, 704, 1204
Ida, S., & Lin, D. N. C. 2004, ApJ, 604, 388
Isella, A., Carpenter, J. M., & Sargent, A. I. 2009, ApJ, 701, 260
Jacquinet-Husson, N., Crepeau, L., Armante, R. et al. 2011 JQSRT, 112, 2395
Kamp, I. & Dullemond, C. P. 2004, ApJ, 615, 991
Kamp, I., Tilling, I., Woitke, P., Thi, W.-F., & Hogerheijde, M. 2010, A&A, 510, A18
Kasting, J. F., Whitmire, D. P., & Reynolds, R. T. 1993, Icarus, 101, 108
Kastner, J. H., Zuckerman, B., Weintraub, D. A., & Forveille, T. 1997, Science, 277, 67
Käufl, H.-U., Ballester, P., Biereichel, P., et al. 2004, Proc. SPIE, 5492, 1218
Kenyon, S. J., & Hartmann, L. 1987, ApJ, 323, 714
Kessler-Silacci, J., Augereau, J.-C., Dullemond, C. P., et al. 2006, ApJ, 639, 275
Klahr, H., & Bodenheimer, P. 2006, ApJ, 639, 432
Kley, W., Bitsch, B., & Klahr, H. 2009, A&A, 506, 971
Knez, C., Lacy, J. H., Evans, N. J., II, van Dishoeck, E. F., & Richter, M. J. 2009, ApJ, 696, 471
Kominami, J., & Ida, S. 2002, Icarus, 157, 43
Koresko, C. D., Herbst, T. M., & Leinert, C. 1997, ApJ, 480, 741
Koresko, C. D., Blake, G. A., Brown, M. E., Sargent, A. I., & Koerner, D. W. 1999, ApJ, 525, L49
Kress, M. E., Tielens, A. G. G. M. & Frenklach, M. 2010, Advances in Space Research, 46, 44
Krotkov, R., Wang, D., & Scoville, N. Z. 1980, ApJ, 240, 940
Kruger, A. J., Richter, M. J., Carr, J. S., et al. 2011, ApJ, 729, 145
Kurosawa, R., Harries, T. J., & Symington, N. H. 2006, MNRAS, 370, 580
Lacy, J. H., Evans, N. J., II; Achtermann, J. M., Bruce, D. E., Arens, J. F., Carr, J. S. 1989, ApJ, 342, L43
Lahuis, F., & van Dishoeck, E. F. 2000, A&A, 355, 699
Lahuis, F., & Boogert, A. 2003, SFChem 2002: Chemistry as a Diagnostic of Star Formation, ed. C. L. Curry & M. Fich (NRC Press, Ottawa, Canada), p. 335
Lahuis, F., et al. 2006, ApJ, 636, L145
Lahuis, F., et al. 2006b, c2d Spectroscopy Explanatory Suppl. (Pasadena: Spitzer Science Center)
Lahuis, F., van Dishoeck, E. F., Blake, G. A., et al. 2007, ApJ, 665, 492
Lahuis, F., Kamp, I., Thi, W. F., van Dishoeck, E. F. & Woitke, P. 2011, IAU Symposium 280, Poster 44
Langer, W. D.; Graedel, T. E. 1989, ApJS, 69, 241

Langer, W. D. & Penzias, A. A. 1990, ApJ, 357, 477
Leinert, C., Beck, T. L., Ligori, S., Simon, M., Woitas, J., & Howell, R. R. 2001, A&A, 369, 215
Lissauer, J. J. 1993, ARA&A, 31, 129
Loinard, L., Torres, R. M., Mioduszewski, A. J., & Rodríguez, L. F. 2008, ApJ, 675, L29
Lommen, D., Wright, C. M., Maddison, S. T., Jørgensen, J. K., Bourke, T. L., van Dishoeck, E. F., Hughes, A., Wilner, D. J., Burton, M., & van Langevelde, H. J. 2007, A&A, 462, 211
Luhman, K. L., Allen, L. E., Allen, P. R., et al. 2008, ApJ, 675, 1375
Madhusudhan, N., Harrington, J., Stevenson, K. B., et al. 2011, Nature, 469, 64
Madhusudhan, N. & Seager, S. 2011, The Astrophysical Journal, 729, 41
Mandell, A. M., Mumma, M. J., Blake, G. A., Bonev, B. P., Villanueva, G. L., & Salyk, C. 2008, ApJ, 681, L25
Mandell, A. M., Deming, L. D., Blake, G. A., Knutson, H. A., Mumma, M. J., Villanueva, G. L., & Salyk, C. 2011, ApJ, 728, 18
Mandell, A. M., Bast, J., van Dishoeck, E. F., et al. 2012, ApJ, 747, 92
Markwick, A. J., Ilgner, M., Millar, T. J., & Henning, T. 2002, A&A, 385, 632
Markwick, A. J., & Charnley, S. B. 2004, Astrobiology: Future Perspectives, 305, 33
Martin, S. C. 1997, ApJ, 478, L33
Mayor, M., & Queloz, D. 1995, Nature, 378, 355
McCaughrean, M. J., & O'Dell, C. R. 1995, NASA, PRC95-45b,ST Sci OPO
Meijerink, R., Poelman, D. R., Spaans, M., Tielens, A. G. G. M., & Glassgold, A. E. 2008, ApJ, 689, L57
Meijerink, R., Pontoppidan, K. M., Blake, G. A., Poelman, D. R., & Dullemond, C. P. 2009, ApJ, 704, 1471
Melo, C. H. F. 2003, A&A, 410, 269
Men'shchikov, A. B., & Henning, T. 1997, A&A, 318, 879
Millar, T. J., & Herbst, E. 1994, A&A, 288, 561
Mitchell, G. F. 1984, ApJS, 54, 81
Mordasini, C., Alibert, Y., & Benz, W. 2009, A&A, 501, 1139
Mordasini, C., Alibert, Y., Benz, W., & Naef, D. 2009, A&A, 501, 1161
Mumma, M. J., et al. 2011, ApJ, 734, L7
Mumma, M. J. & Charnley, S. B. 2011, Annual Review of Astronomy and Astrophysics, 49, 471
Muzerolle, J., Calvet, N., & Hartmann, L. 2001, ApJ, 550, 944
Muzerolle, J., Calvet, N., Hartmann, L., & D'Alessio, P. 2003, ApJ, 597, L149
Najita, J., Carr, J. S., Glassgold, A. E., Shu, F. H. & Tokunaga, A. T. 1996, ApJ, 462, 919
Najita, J. R., Edwards, S., Basri, G., & Carr, J. 2000, Protostars and Planets IV,

eds. V. Mannings, (Tucson: Univ. of Arizona), 457
Najita, J., Carr, J. S., & Mathieu, R. D. 2003, ApJ, 589, 931
Najita, J. R., Carr, J. S., Glassgold, A. E., & Valenti, J. A. 2007, Protostars and Planets V, ed. B. Reipurth, (Tucson: Univ. of Arizona), 507
Najita, J. R., Carr, J. S., Strom, S. E., Watson, D. M., Pascucci, I., Hollenbach, D., Gorti, U., & Keller, L. 2010, ApJ, 712, 274
Najita, J. R., Ádámkovics, M., & Glassgold, A. E. 2011, ApJ, 743, 147
Natta, A., Meyer, M. R., & Beckwith, S. V. W. 2000, ApJ, 534, 838
Natta, A., Testi, L., & Randich, S. 2006, A&A, 452, 245
Natta, A., Testi, L., Calvet, N., et al. 2007, Protostars and Planets V, 767
Najita, J. R., Ádámkovics, M., & Glassgold, A. E. 2011, ApJ, 743, 147
Nomura, H., Aikawa, Y., Tsujimoto, M., Nakagawa, Y., & Millar, T. J. 2007, ApJ, 661, 334
Nomura, H., Aikawa, Y., Nakagawa, Y., & Millar, T. J. 2009, A&A, 495, 183
Öberg, K. I., Boogert, A. C. A., Pontoppidan, K. M., et al. 2008, ApJ, 678, 1032
Öberg, K. I., Garrod, R. T., van Dishoeck, E. F., & Linnartz, H. 2009, A&A, 504, 891
Öberg, K. I., et al. 2011, ApJ, 734, 98
O'Dell, C. R., Wen, Z., & Hu, X. 1993, ApJ, 410, 696
Oliveira, I., et al. 2010, ApJ, 714, 778
Pascucci, I., Apai, D., Luhman, K., Henning, T., Bouwman, J., Meyer, M. R., Lahuis, F., & Natta, A. 2009, ApJ, 696, 143
Paufique, J., Biereichel, P., Donaldson, R., et al. 2004, Proc. SPIE, 5490, 216
Pineau des Forêts, G., Flower, D. R., Hartquist, T. W., Millar, T. J. 1987, MNRAS, 227, 993
Pontoppidan, K. M. 2006, A&A, 453, L47
Pontoppidan, K. M., Dullemond, C. P., Blake, G. A., Boogert, A. C. A., van Dishoeck, E. F., Evans, N. J., II, Kessler-Silacci, J., & Lahuis, F. 2007, ApJ, 656, 980
Pontoppidan, K. M., Blake, G. A., van Dishoeck, E. F., Smette, A., Ireland, M. J., & Brown, J. 2008, ApJ, 684, 1323
Pontoppidan, K. M., Meijerink, R., Dullemond, C. P., & Blake, G. A. 2009, ApJ, 704, 1482
Pontoppidan, K. M., Salyk, C., Blake, G. A., Meijerink, R., Carr, J. S., & Najita, J. 2010, ApJ, 720, 887
Pontoppidan, K. M., Blake, G. A., & Smette, A. 2011, ApJ, 733, 84
Pontoppidan, K. M., van Dishoeck, E., Blake, G. A., et al. 2011, The Messenger, 143, 32
Prato, L., Greene, T. P., & Simon, M. 2003, ApJ, 584, 853
Prinn, R. G. 1993, Protostars and Planets III, ed. E. Levy & J. I. Lunine (Tucson: University of Arizona Press), 1005

Przygodda, F. 2004, Ph.D. Thesis, , Max-Planck Institute of Astronomy, Heidelberg
Qi, C., Wilner, D. J., Calvet, N., Bourke, T. L., Blake, G. A., Hogerheijde, M. R., Ho, P. T. P., & Bergin, E. 2006, ApJ, 636, L157
Reipurth, B., & Zinnecker, H. 1993, A&A, 278, 81
Rettig, T. W., Haywood, J., Simon, T., Brittain, S. D., & Gibb, E. 2004, ApJ, 616, L163
Ricci, L., Testi, L., Natta, A., Neri, R., Cabrit, S., & Herczeg, G. J. 2010, A&A, 512, A15
Richter, M. J., Lacy, J. H., Jaffe, D. T., Mar, D. J., Goertz, J., Moller, W. M., Strong, S., Greathouse, T. K. 2006, SPIE, 6296, p.62691
Robitaille, T. P., Whitney, B. A., Indebetouw, R., & Wood, K. 2007, The Astrophysical Journal Supplement Series, 169, 328
Roccatagliata, V., Ratzka, T., Henning, T., et al. 2011, A&A, 534, A33
Rodgers, S. D., & Charnley, S. B. 2003, ApJ, 585, 355
Rothman, L. S., Gordon, I. E., Barbe, A. et al. 2009, JQSRT, 110, 533
Salyk, C., Blake, G. A., Boogert, A. C. A., & Brown, J. M. 2007, ApJ, 655, L105
Salyk, C., Pontoppidan, K. M., Blake, G. A., Lahuis, F., van Dishoeck, E. F., & Evans, N. J., II 2008, ApJ, 676, L49
Salyk, C., Blake, G. A., Boogert, A. C. A., & Brown, J. M. 2009, ApJ, 699, 330
Salyk, C., Pontoppidan, K. M., Blake, G. A., Najita, J. R., & Carr, J. S. 2011, ApJ, 731, 130
Salyk, C., Blake, G. A., Boogert, A. C. A., & Brown, J. M. 2011, ApJ, 743, 112
Schegerer, A. A., Wolf, S., Hummel, C. A., Quanz, S. P., & Richichi, A. 2009, A&A, 502, 367
Schöier, F. L., van der Tak, F. F. S., van Dishoeck, E. F., & Black, J. H. 2005, A&A, 432, 369
Smith, I. W. M., & Warr, J. F. 1991, J. Chem. Soc., Faraday Trans., 87, 807
Smith, R. L., Pontoppidan, K. M., Young, E. D., Morris, M. R., & van Dishoeck, E. F. 2009, ApJ, 701, 163
Smith, I.W.M. 2011, ARA&A, 49, 29
Stäuber, P., Doty, S. D., van Dishoeck, E. F., & Benz, A. O. 2005, A&A, 440, 949
Stempels, H. C., & Piskunov, N. 2003, A&A, 408, 693
Sternberg, A., & Dalgarno, A. 1995, ApJS, 99, 565
Störzer, H., & Hollenbach, D. 1999, ApJ, 515, 669
Takami, M., Bailey, J., & Chrysostomou, A. 2003, A&A, 397, 675
Thi, W.-F., van Zadelhoff, G.-J., & van Dishoeck, E. F. 2004, A&A, 425, 955
Thompson, R. I. 1985, ApJ, 299, L41
Tielens, A. G. G. M., Charnley, S. B. 1997, Origin of Life, 27, p.23
Trilling, D. E., Lunine, J. I., & Benz, W. 2002, A&A, 394, 241
Valenti, J. A., Basri, G., & Johns, C. M. 1993, AJ, 106, 2024

Valenti, J. A., Johns-Krull, C. M., & Linsky, J. L. 2000, ApJS, 129, 399
van der Plas, G., van den Ancker, M. E., Acke, B., Carmona, A., Dominik, C., Fedele, D., & Waters, L. B. F. M. 2009, A&A, 500, 1137
van der Tak, F. F. S., Black, J. H., Schöier, F. L., Jansen, D. J., & van Dishoeck, E. F. 2007, A&A, 468, 627
Vasyunin, A. I., Wiebe, D. S., Birnstiel, T., Zhukovska, S., Henning, T., & Dullemond, C. P. 2011, ApJ, 727, 76
Viti, S., Jimenez-Serra, I., Yates, J. A., Codella, C., Vasta, M., Caselli, P., Lefloch, B., Ceccarelli, C. 2011, ApJ, 740, L3
Walsh, C., Millar, T. J., & Nomura, H. 2010, ApJ, 722, 1607
Walsh, C., Nomura, H., Millar, T. J., & Aikawa, Y. 2012, ApJ, 747, 114
Ward, W. R. 1997, Icarus, 126, 261
Whittet, D. C. B., Prusti, T., Franco, G. A. P., Gerakines, P. A., Kilkenny, D., Larson, K. A., & Wesselius, P. R. 1997, A&A, 327, 1194
Willacy, K., Klahr, H. H., Millar, T. J., & Henning, T. 1998, A&A, 338, 995
Willacy, K., & Woods, P. M. 2009, ApJ, 703, 479
Wilson, T. L., & Rood, R. 1994, ARA&A, 32, 191
Woitke, P., Kamp, I., & Thi, W.-F. 2009, A&A, 501, 383
Woods, P. M., Willacy, K. 2007, ApJ, 655, L49
Yang, H., Johns-Krull, C. M., & Valenti, J. A. 2007, AJ, 133, 73

Nederlandse samenvatting[1]

Er worden voortdurend nieuwe planeten geboren en we kunnen bijna wekelijks lezen over nieuwe planetenstelsels die worden ontdekt. Met dit in het achterhoofd, is het wonderbaarlijk hoe de menselijke wil om nieuwe werelden te verkennen de sterrenkunde een impuls heeft gegeven. Zo kunnen we, binnen 20 jaar na het detecteren van de eerste planeet buiten ons eigen zonnestelsel, bepalen welk type atmosferen deze planeten hebben en zelfs of ze aan voorwaarden voor mogelijk leven voldoen. Dit soort ontdekkingen leiden echter tot nog meer vragen dan antwoorden. Vragen als: Zijn planetenstelsels zoals ons zonnestelsel gangbaar, en zijn er andere planeten die op de Aarde lijken? Zijn wij en andere levensvormen op deze planeet ontstaan door puur toeval, en kan zoiets ook ontstaan op andere plaatsen in het heelal? Om deze vragen te kunnen beantwoorden is het van belang te begrijpen hoe verschillende soorten planeten kunnen vormen. Het belangrijkste doel van dit proefschrift is dan ook om bij te dragen aan de kennis over het ontstaan van verschillende soorten, en in het bijzonder dat van aardachtige, planeten.

Planeetvorming

Om het onderzoek in dit proefschrift te begrijpen, zullen we met wat achtergrondinformatie beginnen over wat we momenteel weten over planeetvorming. In alle sterrenstelsels, waaronder ons eigen, zijn er vele grote wolken van gas en stof met diameters tot 300 lichtjaar. Deze wolken worden koude moleculaire wolken genoemd, omdat ze temperaturen hebben rond -250 graden Celsius. Wanneer zo'n wolk begint te krimpen onder zijn eigen zwaartekracht, zal de dichtheid ervan hoger en hoger worden totdat de binnenste delen ervan zo dicht en warm zijn, dat er een ster wordt geboren. Het overblijvende gas en stof zal dan een schijf beginnen te vormen die draait rond de ster. In de loop van de tijd zal een deel van het stof en gas in de schijf aan elkaar beginnen te plakken. Zo kunnen steeds grotere klonten ontstaan, totdat enkele ervan groot genoeg zijn om van een planeet te kunnen spreken. Aangezien deze schijf de geboorteplaats is van de planeten, wordt het

[1] Translation from English to Dutch made by R.F.J. van der Burg.

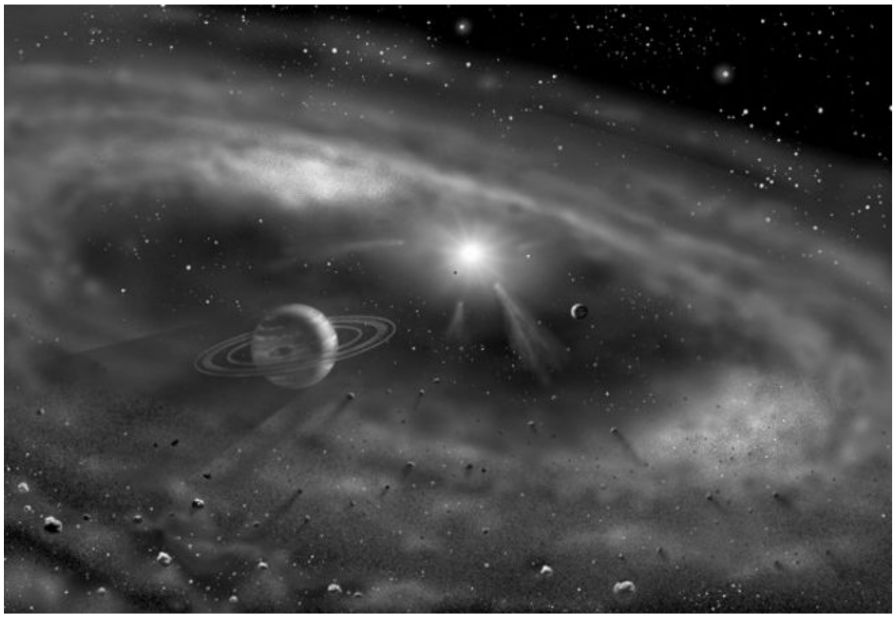

Figure 1 Een jonge ster met zijn protoplanetaire schijf waarin planeten worden gevormd (een artistieke voorstelling, © David A. Hardy/www.astroart.org).

wel een protoplanetaire schijf genoemd. Fig. 1 laat een artistieke voorstelling van zo'n protoplanetaire schijf zien.

De verschillende stadia van planeetvorming kunnen worden gesimuleerd in een planeetformatie model, en de evolutie van het gas en stof in de schijf door een schijfevolutie model. Er zijn vandaag de dag verschillende soorten planeetvorming en schijfevolutie modellen en het is nog onduidelijk welke het meest correct zijn. Een andere manier om naar deze modellen te kijken is om ze te beschouwen als recept voor het maken van planeten. De invoerwaarden in het model, bijvoorbeeld de temperatuur en dichtheid van het gas op verschillende afstanden van de ster, kunnen worden gezien als de ingrediënten in het recept voor het maken van een planetenstelsel. Het is ook interessant om te zien wat voor soort moleculen zich bevinden in de zones van schijven waar planeten vormen, omdat moleculen de bouwstenen van het leven zijn.

Een molecuul is een groep van verbonden atomen. Zo is water bijvoorbeeld een molecuul dat bestaat uit twee waterstofatomen en een zuurstofatoom. Omdat alles is opgebouwd uit moleculen is het zo belangrijk om te zien welke moleculen er in deze protoplanetaire schijven voorkomen. Hieruit kunnen we voorspellen waar de

planeten en hun atmosferen uit zullen gaan bestaan. Bovendien is het interessant om te onderzoeken hoeveel je van elk molecuul op verschillende plaatsen in de schijf aantreft. Als je bijvoorbeeld weet dat er veel water in de binnenste delen van deze protoplanetaire schijven voorkomt, dan kunnen we afleiden dat er een grote kans is dat hier ook planeten vormen met water erop. Hoe kunnen we dus helpen deze modellen te verbeteren en controleren of ze juist zijn of niet?

De eerste stap om deze modellen te verbeteren is om limieten te bepalen voor de invoerparameters, ofwel de ingrediënten, van de modellen. Dit kan worden gedaan door uit waarnemingen van het gas in deze schijven bijvoorbeeld de temperaturen en dichtheden van het gas in deze regio te schatten. Een alternatief is om de verschillende soorten moleculen die hier voorkomen op te sporen en hun relatieve hoeveelheden te schatten. Deze resultaten kunnen dan worden vergeleken met de exoplaneten die we momenteel ontdekt hebben. Voorspellen deze modellen bijvoorbeeld planeetstelsels met grote gasplaneten dicht bij de ster, zoals in sommige gevallen in de waarnemingen gevonden is? Of is het gebruikelijk dat deze regionen aan de juiste fysieke voorwaarden voldoen, zoals de juiste temperatuur en de aanwezigheid van voldoende basale organische moleculen, om complexe organische moleculen zoals aminozuren te kunnen produceren die belangrijke ingrediënten zijn voor het ontstaan van leven?

Waarnemingen van protoplanetaire schijven

Het belangrijkste doel van dit proefschrift is het verstrekken van de invoerparameters voor schijfevolutie en de planeetformatie modellen, en hier limieten op te stellen door de eigenschappen van gas in protoplanetaire schijven te bepalen. Door gebruik te maken van waarnemingen willen we een aantal specifieke vragen beantwoorden, zoals:

- Welk type moleculen vinden we in deze gebieden?
- Wat zijn de temperaturen en dichtheden van het moleculaire gas?
- Wat is de oorsprong van deze moleculen?

Waarnemingen van protoplanetaire schijven kunnen op verschillende manieren gedaan worden, afhankelijk van het deel van de protoplanetaire schijf dat we willen onderzoeken. Onze grootste interesse is om de binnenste gebieden van de schijf te onderzoeken, die op dezelfde afstand van de ster liggen als Aarde, Mars en Venus ten opzichte van de Zon. Dit is dus het gebied binnen protoplanetaire schijven waar meer aardachtige planeten gevormd zouden kunnen worden, of tenminste, in tegenstelling tot Jupiter en Saturnus die voornamelijk uit gas bestaan, planeten met een vaste ondergrond. Dit betekent dat we door het bestuderen van deze gebieden beter kunnen begrijpen hoe onze eigen planeet ongeveer 4,6 miljard jaar geleden gevormd is. Bovendien krijgen we zo meer informatie of andere sterren aan goede voorwaarden voldoen om aardachtige planeten te kunnen vormen.

Figure 2 De Very Large Telescope (VLT) op Paranal in Chili. De telescopen zijn geplaatst op één van de bergtoppen van de Atacama woestijn op 2635 meter boven zeeniveau (ESO/G.Gillet).

Omdat dit gebied van een protoplanetaire schijf behoorlijk dicht bij de ster staat, is het gas dat we bestuderen zeer warm, met temperaturen variërend van enkele honderden tot enkele duizenden graden Celsius. Dergelijk warm gas zendt infrarode straling uit (hetzelfde type straling als andere warme voorwerpen uitstralen, en wat we voelen als warmte). Dit soort straling kan worden waargenomen met behulp van één van de Very Large Telescopen (VLT), die liggen in de Atacama woestijn in Chili (zie Fig. 2). Deze 4 telescopen hebben spiegels met een diameter van 8,2 meter en bevinden zich op 2635 meter boven zeeniveau. De belangrijkste resultaten van dit proefschrift kwamen tot stand uit een groot waarneemprogramma van 24 nachten met één van deze telescopen bestaande uit waarnemingen van meer dan 50 protoplanetaire schrijven. Het voordeel van een dergelijke grote steekproef is dat we schijven met verschillende leeftijden kunnen bestuderen, wat ons informatie verschaft over de wijze waarop het gas in deze schijven evolueert met de tijd.

Hoe een astronoom temperaturen en dichtheden van gas kan schatten op lichtjaren afstand.

Dan rest ons toch nog één centrale vraag. Hoe kunnen we bijvoorbeeld de temperatuur en de dichtheid van het gas schatten, zonder de mogelijkheid er heen te gaan om het te meten? Dit is het grootste probleem voor een astronoom, we kunnen niet naar de objecten die we bestuderen reizen om onze theorieën te testen. De oplossing is om in plaats daarvan het licht van deze objecten te bestuderen, en te bepalen hoe dit licht wordt beïnvloed door fysische omstandigheden op de plaats waar het wordt uitgezonden. De belangrijkste methode om dit licht te meten en om informatie te extraheren heet spectroscopie.

Een manier om spectroscopie uit te leggen is om eerst te realiseren dat wit licht bestaat uit veel verschillende kleuren. Dat blijkt wanneer je wit licht door een prisma laat vallen. Dan kun je zien hoe het licht van wit naar alle kleuren van de regenboog gaat. Wat een spectrometer doet is meten hoeveel van elk soort kleur aanwezig is in het licht dat wordt waargenomen, dus bijvoorbeeld of het meer rood licht heeft dan blauw. De verdeling van de verschillende kleuren is gerelateerd aan de temperatuur van de lichtbron.

In dit geval kunnen we de ster beschouwen als een lamp die wit licht uitzendt. Als we dit licht met een telescoop verzamelen en door een spectrometer laten gaan, zouden we een regenboog zien. Maar als het licht een wolk van gas zou passeren, dat zich tussen ons en de ster bevindt, zou een deel van het licht worden geabsorbeerd door de gaswolk. Afhankelijk van het soort gas in de wolk, worden bepaalde kleuren geabsorbeerd en deze kleuren worden dan niet gezien in de spectrometer op Aarde. Op deze manier zie je een regenboog patroon met zwarte lijnen op plaatsen waar de kleuren geabsorbeerd zijn. Zo heeft elk type gas zijn eigen vingerafdruk. Dus door het sterlicht dat een gasschijf rond de ster passeert

te meten, kunnen we zien of er zich water bevindt of niet. We kunnen dan ook meten hoeveel water er aanwezig is, en een schatting maken van de temperatuur van zowel de ster als de waterdamp in de schijf. Dit is één van de belangrijkste methoden die in dit proefschrift wordt gebruikt voor het bestuderen van protoplanetaire schijven.

De belangrijkste ontdekkingen in dit proefschrift

Een nieuwe onverwachte locatie van koolmonoxide en water.

De detectie van water in de binnenste zones van protoplanetaire schijven was een grote ontdekking in 2008 (Carr & Najita 2008, Salyk et al. 2008). Deze ontdekking, plus daaropvolgende waarnemingen, laten zien dat water een veelvoorkomend molecuul is op plaatsen waar planeten ontstaan. Dit proefschrift laat echter zien dat deze analyses, waaruit wordt opgemaakt dat het water zich in een schijf bevindt, niet altijd het water en andere moleculen zoals koolmonoxide en het hydroxyl radicaal op een juiste manier lokaliseren. Deze moleculen lijken namelijk zowel in een roterende schijf als een schijfwind voor te komen. Een schijfwind wordt veroorzaakt door gas dat uit de schijf wordt geworpen doordat het wordt opgewarmd door straling afkomstig van de ster. Het is belangrijk om rekening te houden met de verschillende locaties van de moleculen. Anders zullen we de moleculaire abundanties verkeerd schatten, wat zou leiden tot verkeerde resultaten over de soorten planeten die kunnen vormen, of over hoe de chemie zal evolueren in de protoplanetaire schijven.

Detecties van nieuwe moleculen

In vorige studies werden uitsluitend water, koolmonoxide en hydroxyl-radicalen gedetecteerd in de warme binnengebieden van de schijf. Nu detecteren we echter ook blauwzuur en acetyleen met een nieuwe waarnemingstechniek die we hebben ontwikkeld. We laten zien dat deze methode kan worden gebruikt om naar nog meer moleculen te zoeken, zoals ammoniak en methaan. Omdat dit cruciale bouwstenen zijn voor complexere organische moleculen is het van belang om al deze moleculen te detecteren en om een schatting te maken van hun hoeveelheden. Bovendien wordt de temperatuur van het gas waarin ze zich bevinden, geschat op ongeveer 800 – 1200 graden Celsius, wat zal helpen om limieten te stellen op de temperatuurverdeling van de schijfevolutie modellen in deze gebieden.

Stralingsvelden in protoplanetaire schijf modellen

Wanneer sterrenkundigen het licht van de sterren dat door het gas is gegaan detecteren, moeten ze verschillende benaderingen maken om de temperatuur en dichtheid van het gas te kunnen schatten. Dit wordt gedaan om de berekeningen

makkelijker te maken, aangezien ze al zeer complex zijn. In dit proefschrift wordt aangetoond dat het belangrijk is om zowel de UV- als de Röntgen-straling van de ster mee te nemen in de modellen. Echter, in het algemeen wordt slechts met één van de twee rekening gehouden, wat onjuiste schattingen geeft voor de moleculaire abundanties.

Een inventarisatie van organische moleculen in schijven

Er zijn nog maar weinig moleculen ontdekt in de binnenste regionen rond sterren waar planeten vormen. De modellen voorspellen dat er daar ook grotere organische moleculen voor zouden moeten komen die belangrijk zijn voor het vormen van planeten die omgeven worden door een atmosfeer met goede leefomstandigheden. Een zoektocht naar deze grotere organische moleculen werd daarom uitgevoerd omdat dit nog niet eerder is gedaan. De resultaten toonden slechts bovengrenzen aan in plaats van duidelijke detecties. Dit komt doordat de huidige telescopen nog niet krachtig genoeg zijn. Echter, onze resultaten laten zien dat nieuwe telescopen die nu worden gebouwd deze moleculen wel kunnen gaan detecteren. We tonen ook aan dat de moleculaire abundanties in kometen vergelijkbaar zijn met die in de protoplanetaire schijven zijn waargenomen, wat de theorie ondersteunt dat kometen worden gevormd in dezelfde chemische omgeving als de planeten.

Laatste woorden

Zoals eerder vermeld, kan een planeetformatie of schijfevolutie model gezien worden als een recept over hoe we verschillende soorten planeetstelsels kunnen bouwen, waar de specifieke uitkomst afhankelijk is van de ingrediënten in het recept. Dit proefschrift heeft bijgedragen door ons veel meer van deze ingrediënten te verschaffen, door detecties van nieuwe moleculen, door het bepalen van hun locaties, door het meten van de temperatuurvariatie binnen de schijf, en door te verduidelijken hoe we verschillen soorten straling van de sterren in rekening moeten brengen. Dit toont aan hoe we met de huidige waarnemingen niet alleen kunnen leren begrijpen hoe andere planeetstelsels gevormd zijn, maar ook hoe onze naburige planeten gevormd zijn en of er andere werelden zoals de onze zijn.

English summary

Right now new planets are born and we can read almost weekly about new planetary systems that are discovered. Having that in mind it is amazing how the human quest to explore new worlds has pushed astronomy, within 20 years from detecting the first planet outside of our own solar system to being able to determine which type of atmospheres these planets have and if they may have conditions which are even suitable for life. These types of discoveries however lead to even more questions than answers. Questions such as: Are planetary systems like our own common and are there other Earth-like planets out there? Are we and other life forms on this planet just a pure coincidence or something that can also be created in other places in the Universe? One important part of being able to answer these questions is to understand how different types of planets can form. The main goal of this thesis is therefore to contribute to the understanding of how different types of planets form and then especially the formation of Earth-like planets.

Planet-formation

To be able to understand the studies in this thesis we will start with some background on what we know today about planet-formation. In all galaxies, including our own, there are many large clouds of gas and dust with diameters up to 300 light years. These clouds are called cold molecular clouds, since they have temperatures of around -250 degrees Celsius. Such a cloud can suddenly start to contract under its own gravity so parts of it will get more and more dense, until the inner parts of it becomes so dense and warm that a star is born there. The rest of the gas and dust will then start building a disk that is spinning around the star. With time, part of the dust and gas in the disk will start to stick together and build up larger clumps until some of the clumps in the end evolve into being large enough to be called a planet. Since this disk is the birth place of planets it is called a protoplanetary disk. In Fig. 1 an artist's impression of such a protoplanetary disk is presented.

The different stages of planet-formation can be simulated in a planet-formation model and the evolution of the gas and dust in the disk is described in a disk

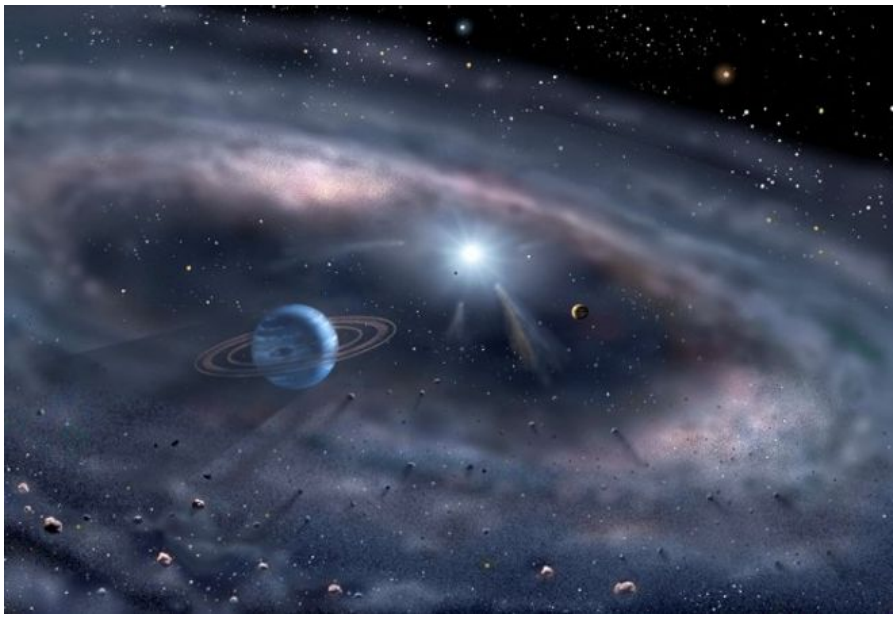

Figure 1 A young star with its protoplanetary disk around it that is in the process of forming planets (An artist's impression, © David A. Hardy/www.astroart.org).

evolution model. There are today several different kinds of planet-formation and disk evolution models and we still do not know which of them are the most correct ones. Another way to look at these models can be to see them as recipes for how to form planets. The input values in the model, for example the temperatures and densities of the gas at different radii can be seen as the ingredients in the recipe for making a planetary system. It is also interesting to see what type of molecules you have in the planet-forming zones of disks, since molecules are the building blocks of life.

A molecule is a group of atoms that are bound together. For example, water is a molecule that consists of two hydrogen atoms and one oxygen atom. Everything is built up by molecules which is why it is so important to see which molecules you have in these protoplanetary disks since this will tell us what the planets and their atmospheres will consist of. In addition it is interesting to investigate how much you have of each molecule at different radii of the disk. For example if you know that there is a lot of water in the inner parts of these protoplanetary disks then you can conclude that there is a high probability that you can also form planets with water on them in these regions. So how can we help to improve these models and check if they are correct or not?

The first step to be able to improve these models is to help constrain the input parameters, hence the ingredients, to the models. This can be done by using observations of the gas in the disks to estimate, for example, which temperatures and densities the gas has in these regions. Another way is to detect the different types of molecules that exist there and calculate their relative abundances. These results can then be compared to the exoplanets that we see today. Hence, do these models predict, for example, planetary systems with giant gaseous planets close to the star, as in some cases have been detected already during observations? Or is it common that these regions have good physical conditions such as the right temperatures and enough amounts of basic organic molecules to be able to produce more complex organic molecules, such as amino acids, that are important ingredients for building life on a planet?

Observations of protoplanetary disks

The main goal of this thesis is to provide and constrain the input parameters for disk evolution and the planet-formation models by determining the characteristics of gas in protoplanetary disks. By using observations we want to answer some specific questions such as for example:

- Which type of molecules can we find in these regions?
- What are the temperatures and densities of molecular gas?
- What is the origin of these molecules?

Figure 2 The Very Large Telescope (VLT) at Paranal in Chile. These telescopes are placed on one of the mountains peaks in the Atacama desert at 2,635 meters above sea level (ESO/G.Gillet).

The observations of protoplanetary disks can be done in several different ways depending on which part of the protoplanetary disk we want to study. Our main interest was to probe the inner regions of the disk which lie within the same distance from the star as Earth, Mars and Venus are from the Sun. Hence this is the zone in a protoplanetary disks where more Earth-like planets could be forming or at least planets which have a solid surface and in contrast to Jupiter and Saturn do not consist primarily of gas. This means that by studying these regions we can better understand how our own planet formed around 4.6 billion years ago and also get more information about if other stars have good conditions for Earth-like planets to be able to form.

Since this region of a protoplanetary disk is rather close to the star it means that the gas that we are studying is very warm, ranging from temperatures of a few hundred to a few thousand degrees Celsius. Such warm gas emits infrared radiation (which is the same type of radiation that other warm bodies emit and we feel as heat). This type of radiation can be observed using one of the Very Large Telescopes (VLT) which lie in the Atacama desert in Chile (see Fig. 2). These 4 telescopes have mirrors with a diameter of 8.2 meters and are positioned at 2,635 meters above sea level. The main results of this thesis come from a large observational program of 24 nights of observations of a sample of over 50

protoplanetary disks using one of these telescopes. The advantage of having such a large sample is that we can study disks with different ages and therefore giving us information about how the gas within the disks evolves with time.

How an astronomer can estimate temperatures and densities of gas light years away from Earth.

So one main question remains, though. How can we estimate for example the temperature and the density of the gas without being able to go there and measure it. This is the main problem for an astronomer, we cannot go to the objects we study to test our theories. The solution is to instead study the light these objects emit and how this light is affected by physical conditions in the place it is emitted. The main method to measure this light and to extract information is called spectroscopy.

One way to explain spectroscopy is to first understand that white light consist of many different colours. That can be seen when you let white light go through a prism. Then you can see how the light goes from white light to all the colours of the rainbow. What a spectrometer does is to measure how much of each kind of colour is present in the light that is observed, hence if it, for example, has more red light than blue. The variations of the different amounts of colour are related to which temperature the source of the light has.

In this case, we can see the star as a lamp that emits white light. If we would gather this light with a telescope on Earth and let the light go through a spectrometer we would see a rainbow. However if we would have a cloud of gas between us and the star, that the light would pass on its way to us, some of the light would be absorbed by the gas cloud. Depending on which type of gas it is, different colours gets absorbed and this colour will not be seen in the spectrometer at Earth. Hence you will see a rainbow pattern with black lines in it where the colour should have been which got absorbed. Hence, each type of gas has its own finger print. So by just measuring the light from a star which goes through the gas which lies in the disk around the star we can see for example if there is water or not. We can also then measure how much water is present and estimate which temperatures both the star and the water vapour in the disk have. This is one of the main methods used in this thesis for studying protoplanetary disks.

The main discoveries in this thesis

New unexpected location of carbon monoxide and water.

Detection of water in the inner zones of protoplanetary disks was a big discovery in 2008 (Carr & Najita 2008, Salyk et al. 2008). This discovery plus subsequent detections showed that water seems to be a common molecule in regions where

planets form. What this thesis shows however is that their analysis, which concludes the water to be in the disk, does not always correctly locate the water and some of the other detected molecules such as carbon monoxide, hydroxyl radical, and prussic acid. These molecules instead seem to be located both in a rotating disk and in a disk wind. A disk wind is caused by gas thrown off from the disk due to radiation from the star that heats of the gas so it leaves the disk. It is important to be aware of these different origins of the molecules since it means that if we are not doing this, we will estimate the wrong molecular abundances which will lead to the wrong results of which type of planets can form there or how the chemistry will evolve in the protoplanetary disks.

Detections of new molecules

In previous studies just water, carbon monoxide and hydroxyl radical molecules were detected in the inner warm regions of the disk. However, we now also detect prussic acid and acetylene using a new observational tool that we developed. We show that this tool can also be used to detect even more molecules such as for example ammonia and methane. All of these molecules are important to detect and estimate their abundances since they are crucial building blocks for more complex organic molecules. In addition the temperatures of the gas in which they are located are estimated to be around 800 – 1200 degrees Celsius which will help to constrain the temperature structure in the disk evolution models of these regions.

Radiation fields in protoplanetary disk models

When astronomers detect the light from the stars that has gone through the gas in the disks they have to make several approximations to be able to estimate the temperatures and densities of the gas. This is done to make the calculations easier since they are already very complex. What is shown in this thesis is that it is important to take both the UV-field and X-rays from the star into account in the models and not just one of them as is usually done. Not doing this will give incorrect estimates of the molecular abundances.

An organic inventory of protoplanetary disks

There are still very few molecules detected in these inner planet-forming zones around stars. Models predict that there should also be other larger organic molecules in these regions which are very important for building up planets with atmospheres which provide good conditions for life. A search for these larger organic molecules was therefore performed since this has not been done before. The results gave only upper limits rather than clear detections. This is because the telescopes today are still not powerful enough. However, our results show that new telescopes that are being built now will be able to detect these molecules. We

also show that the molecular abundances in comets are similar to those detected in the protoplanetary disks which supports the theory that comets are formed in the same chemical environment as the planets.

Final words

As was stated earlier, a planet-formation or disk evolution model can be seen as a recipe on how to build different kinds of planetary systems and the specific outcomes depend on the ingredients we put into this recipe. This thesis has contributed by giving us many more of these ingredients, such as for example detections of new molecules by improving the knowledge of their location, by determining the temperature variation within the disk, and by clarifying how we should include different types of radiation fields from the star. This shows how with today's observations we can start to understand not just how other planetary systems form, but also how our neighbouring planets one time formed and if it is possible that other worlds like ours are out there.

Publications

Refereed papers

1. *Exploring organic chemistry in planet-forming zones*
   Jeanette E. Bast, Fred Lahuis, Ewine F. van Dishoeck & Alexander G. G. M. Tielens; Submitted to Astronomy & Astrophysics (Chapter 5)

2. *First detection of near-infrared line emission from organics in young circumstellar disks*
   Avi M. Mandell, **Jeanette E. Bast**, Ewine F. van Dishoeck, Geoffrey A. Blake, Colette Salyk, Michael J. Mumma, M. & Geronimo Villanueva; 2012, The Astrophysical Journal, 747, 92 (Chapter 3)

3. *Single peaked CO emission line profiles from the inner regions of protoplanetary disks*
   Jeanette E. Bast, Joanna M. Brown, Gregory J. Herczeg, Ewine van F. Dishoeck & Klaus M. Pontoppidan; 2011, Astronomy & Astrophysics, 527, A119 (Chapter 2)

4. *The abundance of SiS in circumstellar envelopes around AGB stars*
   Fredrik L. Schöier, **Jeanette E. Bast**, Hans Olofsson & Michael Lindqvist; 2007, Astronomy & Astrophysics, 473, 871

Non-refereed papers

Planet-forming regions at the highest spectral and spatial resolution with VLT-CRIRES
Klaus M. Pontopppidan, Ewine F. van Dishoeck, Geoffrey A. Blake, Rachel Smith, Joanna M. Brown, Gregory J. Herczeg, **Jeanette E. Bast**, Avi M. Mandell, Alain Smette, Wing-Fai This, Edward D. Young, Mark R. Morris William Dent & Hans Ulrich Käufl; 2011, Messenger, 143, 32

Conference proceedings

1. *New probes of the chemistry in the inner regions of planet-forming disks*
   Jeanette. E. Bast, Avi M. Mandell, Ewine F. van Dishoeck, Daniel Harsono & Simon Bruderer, 2011, in The Molecular Universe, IAU Symposium 280 poster proceedings

2. *SiS line emission as a probe of chemistry and grain formation in circumstellar envelopes of AGB stars*
   Jeanette E. Bast, Fredrik L. Schöier & Hans Olofsson; 2007, Molecules in Space and Laboratory

Curriculum Vitae

I was born on the Swedish summer day of the 25th of July 1979 in Stockholm. Nineteen years later I graduated from Sjödalsgymnasiet, finishing the science program. After my studies at the gymnasium, I worked for 7 months at an asphalt and stone laboratory. During the evenings, I took an introductory course in astronomy at Stockholm University. This course started my interest in astronomy since my professor Gösta Gahm so enthusiastically shared his knowledge. However, at this time my mind was set to become a doctor in medicine. The only obstacle to do this was that I needed to upgrade my grades, since you have to have absolute top grades in all topics before can get admitted to any program in medicine in Sweden. While studying to improve my grades, I decided to take chemistry courses for one year at Stockholm University since it would be useful knowledge to have as a doctor. After a year of chemistry studies, I decided to continue with studies in physiotherapy since it would provide a job similar to a doctor but it would be easier to get accepted to. The next 6 months, I studied physiotherapy at the Karolinska Institute. While doing so, I read about a summer science school at Karolinska Institute for medicine students. I applied to this school, and I got accepted, even though I was not a student in medicine, since my chemistry studies compensated for this. For 10 weeks I worked on a pilot project doing research studying the sensitivity of insulin producing cells to a specific toxin. The project turned out very well so it resulted in a larger research project which I was offered to continue working on. I declined, since I now knew that I really wanted to go for science, but instead within astronomy, since I already fell in love with it 2 years earlier. It just took me some time to accept it and give up my original dream to study medicine. A few weeks later I started the physics program at Stockholm university and I felt directly that my choice was right. However life wanted something differently so I had to interrupt my studies after one month for family reasons and wait another year to start things over again. So that year, I worked as a kindergarten teacher instead. I started my studies again one year later and got my Masters degree in astronomy 2007 at Stockholm university.

I was very active in both the social and political student association life during my studies. My larger responsibilities were to be working as the vice president for the social student association for physics students and to be president of the

political student association for the natural sciences faculty. As their president, I was in charge of managing people within the organisation and its sub-organisations plus being the main driver of many projects or causes to maintain or improve the quality of student life and education for around 10,000 undergraduate and graduate students. I was in addition working extra as a teaching assistant for an introductory course in Astronomy. During my studies, I took part in one graduate and two master science schools in Finland, Denmark and France, within the topics of astrobiology and particle physics. I also got a scholarship to take part in a workshop, about ALMA, in Denmark. During this workshop I met graduate students from Ewine van Dishoeck's research group, which made me curious about doing a PhD with her as a supervisor. Just a few months later, still early in my diploma thesis work, a PhD position opened up in her group and I applied and got offered the position. Suddenly I was faced with the choice to leave my country for 4 years. It was not an easy decision since I had not really seriously thought about leaving my country or even my home city, but I took it, which I am very grateful for today.

I started my PhD in the spring of 2007 with Ewine van Dishoeck as my supervisor. Besides Leiden, during the next few years, I worked and lived about 5 months at Caltech in Pasadena (U.S.A.) and 8 months at the Max Planck Institute for Extraterrestrial Physics in Garching (Germany). A big dream came true when I went for a work visit to NASA Goddard Space Flight Center, Washington (U.S.A.). I have given talks at NASA GSFC (U.S.A.), ESTEC (Netherlands), at Universidad Nacional de Colombia, Bogotá (Colombia) and at a conference in Glasgow (Scottland). I have presented posters at conferences in Vienna (Austria), Paris (France), Pasadena (U.S.A.), Toledo (Spain) and Gothenburg (Sweden), I attended two graduate science schools, one in Rome (Italy) and one in Tällberg (Sweden). I have always loved to teach, so I was very happy to be a teaching assistant for three different courses; *The interstellar medium*, the bachelor thesis course in astronomy and *Detection of light*. As a fun side step to my work I was part of an art installation here in Leiden, relating childrens' thoughts about space travel to the scientists' views. During my stay in Garching I also helped out to arrange an exhibition in astronomy at the Deutsches museum in Munich.

My goal during these years has more and more developed into working towards a position where I can combine all my interests in science, management and lobbying politics both within academia and in the space industry. I therefore decided to apply for a position as a contractor at SRON with the consultancy firm Science and Technology as my employer, which offers me many opportunities in the directions I want to develop. I started this job in August, 2012, and I am so far very pleased with my new work and really looking forward to all the new challenges it offers me.

Acknowledgements

So before I start I want to warn you that this will be an unusually long acknowledgement section because I am such a lucky person that I have so many wonderful colleagues, friends and family around me that I don't want to miss out to show them all my gratefulness. So bear with me or just read sections where you are mentioned.

First of all I am very grateful that I got the opportunity to start my PhD at Leiden Observatory. With such a high concentration of very skillfull and enthusiastic scientists it is easy to gain a lot of knowledge and experience. That said, still the science would never move forward without the help of the very efficient and always friendly supporting staff. *Jeanne, Kirsten, Anita, Liesbeth, Jacqueline* and *Evelijn*, thank you for always making me feel so welcomed with my questions and for so fast solving whatever problems I had. The computer guys, as I am used to refer to you. I don't know how many times I mailed or dropped by you in utter despair that something did not work as I wanted. I must say I am very impressed with how fast you are on fixing things. *Tycho* you vanished after a few years but I always enjoyed our chats after the computer problem was solved. *Aart* I will for sure miss to hear about your latest vacation in Sweden and *David* you are just such a sweet and kind person.

During the time of my PhD I had the opportunity to work at three different places: Caltech in Pasadena, MPE in Munich and NASA Goddard in Washington. My main reason to go to Caltech was to collaborate with Geoffrey Blake's group. *Geoff*, I am very grateful for your wise advices and for welcoming me to your group and *Klaus and Colette* for all your work, help and support. Klaus, one hour learning idl next to you was worth more than one month learning it by myself! Especially thanks to the friends outside of work that I got there. *Jessica, Nouhad, Guido, Fabio, Celia, Michele, Terry, Lauren* and *Sawyer*. Our weekends and evenings in California made it an unforgettable time in my life. At MPE I met a lot of very helpful and friendly people and I want to thank you all for making my stay there so pleasant. Especially I am grateful to *Joanna, Greg* and *Simon* that helped me out so much with completing my projects and giving me so much help and advices. Greg you once told me that, I have to believe in myself before any other person can believe in me. Realising that was one of the most important turning points in

my whole PhD. *Jennifer, Camilla, Michele, Francesco, Agata* and *Katie*, you made the coffee breaks and lunches to the best moments of my work days. My final longer work stay was to visit Michael Mumma's group at NASA Goddard, to especially collaborate with Avi Mandell. I am very thankful to you *Mike* for letting me join your group for three weeks and especially Avi for arranging it. *Avi*, collaborating with you during these years has been a pure joy and very inspirational. And *Eva* our Swedish lunches and coffee breaks in the sun were always so much fun. My last chapter in this thesis was mainly done together with Fred Lahuis. *Fred* it was a pleasure working with you and once more thank you so much for doing the last work on our article. *Gerrit*, thank you for many fruitful discussions. I wish you all the best for your future.

To my colleagues at the Sterrewacht. First of all thank you all in the *astrochem group*! We had a lot of fun at the conferences together and our lunches were always a nice break during the day. There are too many people in this group here to mention you all and I am worried I will forget one if I start to write you all down so instead I just say thank you all! Besides the astrochem group I want to especially say that I am very grateful to *Bruno, Willem, Nikta, Olmo, Silvia, Jarle, Bernhard, Franco, Christian, Eduardo, Olivera, Niruj, Nadine, Steven, Irene, Mattia, Berenice, Matteo, Nicola, Thibaut, Liesbeth, Francisco, Jes, Suzanne, Olja, Brent, Sandrine, Ernst, Jean Baptiste, Jordy, Sergio, Karoliina, Joseph* and *Dominic* for so many nice talks in the corridors, lunches, breaks and borrels. You made the observatory such a warm and friendly place to work at.

Then I have my office mates during these years. I must say I have been super lucky because you all always helped me a lot professionally but also by making me smile the moments I needed it the most. My first year I shared an office with *Edo*. We went from office mates to dear friends and I still miss you here in Leiden. *Lars*, even though you are Danish... you are ok... So thank you for that! ;) *Xiaohu*, you are such a nice and caring person, I wish you all the best for your thesis and future. *Jaya*, it was a short time, but when we talked it was intense and could have continued for hours if we would not have had so much work to do. *Dave*, you were just so much fun and always knew how to cheer me up with some comforting words when I needed to hear it. And *Remco*, we had almost 5 years together in that office. And I must say that the office was never the same after you left it. You have such a good heart and I value the friendship we developed highly. And thanks of course for translating my Dutch summary!

I also developed some other closer friendships during my years at the observatory that mainly took place outside of the office. *Olivier*, merci from all of my heart to you for both helping me with my work but mainly for being such a wonderful friend. *Kalle*, you were not just next to my office during 5 years you were also next to me. Always giving me a big hug when I needed it. Always making me laugh or helping me out. You leaving Leiden created a void, not just at work, but also in my life. That you will stand next to me again, when I become a Dr., feels like such a perfect way for me to complete my PhD. *Karin*, many people know what an extraordinary scientist you are but what most people might not know is what

an extraordinary friend you are. I am so proud of you and so utterly grateful for all your support and your caring friendship during all these years. No words would be enough to describe it. So just thank you from all my heart. *Rafael*, you have helped me through many stages of my thesis, both with the practical things, but also by showing that you always believed in me. I am very grateful for this and for the close friendship we developed. *Carina*, you have been like my second half during these last 2.5 years. We have gone through so much together and this thesis would for sure not have been finished without you!!! You have to stay here in Leiden, because a life here without you, would not be a life I would like to live.

To the ones that first inspired me to become an astronomer... *Gösta*, you were my teacher during an introductory evening course in astronomy. Your enthusiasm about your topic and ability to share it was the thing that made me leave my plans to be a medical doctor to instead become doctor in astronomy. Thank you for giving me the initial spark to go for it! *Fredrik*, you were my diploma thesis supervisor in Stockholm. You were the one making me believe that I had the abilities to reach whatever goal I was aiming at. I am very sad that you are no longer with us. I so wish I could have personally given you this thesis, that you already from the beginning said, you knew would be a great one. To the ones in my new work life... *Ralph, Richard, Evert, Toncho* and *Marc*, thank you for being so patient and supporting me so much so I could take the time to finish my PhD, even if it sometimes interfered with my work with you. You really helped me to reach the finish line.

My life in Leiden outside of the office also gave me many wonderful friends... *Eva*, that you are a true part of this thesis in the form of making my cover felt very important to me since you have been a part of my life here in the Leiden almost from the first day I came here. Thank you first all for the amazing cover and to help me make such a cool layout for my thesis!!! But most importantly thank you for being a friend that is always there for me. I am so grateful that I met you. *Iberia*, you are not here anymore but you were for almost 5 years. You leaving the Netherlands was the hardest separation I had to go through from any of my friends leaving Leiden. I miss you still everyday. Thank you for just being you!!! *Erwin*, I thank many people for their contributions to this thesis but without you this thesis would never have been finished. You picked me up when I needed to be picked up, you were my wall when I needed something to lean at and most importantly you always took the time to talk to me when I needed it the most. I feel very happy to have you in my life. *Maiki, Nic, Bas, Carmen, Marlies* and *Angelica*, you are like my little family here in the Leiden. Our weekly activities together is one of the main reasons for me to stay here in Leiden and has made these last two years here to be my most happy ones. Krams! *Dominique*, nobody is as good as you to make me totally forget about my work!!! That really helped me survive my last year of my PhD. *Eric and Anna*, thank you for always caring for me and all the fun we have together. *David Dankers*, thank you for always making see things from a new side. To all my *friends at Salsiando*, you are so great! Our salsa evenings together always bring me so much positive energy!!! To the rest

of my dear friends in Leiden that I have had so many parties, coffees, dinners, wonderful days and evenings with. *Jimi, David Raban, Inge, Ivo, Tonie, Younes, Sicco, Lara, Thomas Vorisek, Andrea, Justin, Julia, Arjan, Renato, Julio, Rodrigo, Lin, Monica, Andres, Pilar, Paul, Hugo, Max, Jorge, Anna Grasskamp, Dalia, Floris* and many more. Thank you for all the joy and happiness you have given me during all these years.

And my travels in my job created many opportunities to develop friendships that stayed also after the trip had finished. *Ray, Felicitas, Ben de Vries, Daniel Camilo, Christoph* and *Marco*, you all contributed to many fun and nice memories and still I hope some more will come. *Alexandre*, you were my biggest support during my middle phase crisis, what all PhD students know to be the toughest stage of your PhD. You made me not quit my PhD which I am very thankful for today. I still value our friendship highly even if we can't meet as often anymore.

And of course my life in Sweden holds many people close to my heart... *Thomas* we finished our astronomy studies, left our country and started our PhDs together here in the NL. If it was not for you, I would probably never have had the courage to move here. Thank you for being such an inspirational person. *Lina*, you are my most frequent visitor from Sweden. You are one of the best people to make me laugh about my worries and forget all about them. Thank you for always bringing sunshine into my life. *Sara*, I still remember when we started our studies together and how we both were dreaming about one day becoming doctors and now we both are. You are one of the first ones I go to for both private and professional advices. Few people are as open-minded as you and I so admire you for the person you are. Thank you *Yufang* and *Zenzan* for being the sisters I never had. You are the BEST ones of reminding me that there is another life outside of studies and work. I am so grateful to know that whatever happens in life I know you will always be there for me. To my other friends in Sweden, *Ricky, Anna Trobäck, Eva Wirström, Ida, Oskar, Henrika, Tompa, Mattias, Linda, Danne, Catherine* and *Kristoffer*. I am so happy that you are all still in my life even though I have been away for almost 6 years now.

To my family... *Mina kusiner, morbröder, farbröder med familjer och mormor*. Även om jag bor långt borta nuförtiden så tänker jag ofta på er och önskar att jag kunde vara närmare er. Ert stöd och omtanke betyder oerhört mycket för mig. To my dear brother *Jimmy*. You are the reason I can be so far away from home without feeling too bad about choosing to live at this long distance from our parents since I know you are next to them when I can't be there. You are one of the best brothers a sister can have. *Farmor och farfar*, ni är mina förebilder för hur jag vill leva mitt liv. Få är så bra som ni på att njuta av ögonblicket och av allt livet har att erbjuda. Jag kommer alltid vara så tacksam att ni gav mig den förmågan. *Mamma och pappa*, ni är och har alltid varit ett ständigt stöd för mig. Jag har ofta valt att gå den mer ovanliga och ibland mer bökiga vägen i mitt liv, men ni är de som gav mig styrkan och tron på mig själv att våga ta den. Inga ord kan beskriva den oerhörda tacksamhet som jag känner till er.